

THE ROLE OF OSTEOCLASTS IN CANCER-ASSOCIATED BONE PAIN

Patrícia Silva Santos Ribeiro

Dissertation to obtain the Degree of Master of Science in Bioengineering at Faculdade de Engenharia da Universidade do Porto and Instituto de Ciências Biomédicas Abel Salazar

Supervisor: Estrela do Céu Neto

Co-supervisor: Meriem Lamghari

October, 2019

The role of osteoclasts in cancer-associated bone pain

Patrícia Silva Santos Ribeiro

Dissertation to obtain the Degree of Master of Science in Bioengineering
(specialization in Molecular Biotechnology) at Faculdade de Engenharia da
Universidade do Porto and Instituto de Ciências Biomédicas Abel Salazar

October, 2019

The work described in this dissertation was conducted at:

i3S/INEB – Instituto de Investigação e Inovação em Saúde/Instituto de Engenharia Biomédica



The work presented in this dissertation was financed by:

FEDER - Fundo Europeu de Desenvolvimento Regional funds through the COMPETE 2020 - Operational Program for Competitiveness and Internationalization (POCI), Portugal 2020, and by Portuguese funds through FCT/MCTES in the framework of the project SproutOC "POCI-01-0145-FEDER-030158, PTDC/MED-PAT/30158/2017". This work had also the support of the i3S Scientific Platforms BioSciences Screening and Bioimaging, members of the PPBI (PPBI-POCI-01-0145-FEDER-022122).



“Education is a progressive discovery
of our own ignorance.”

- Will Durant

AGRADECIMENTOS

Primeiramente, gostaria de agradecer à Estrela por todo o apoio e orientação. Obrigada pela disponibilidade em esclarecer todas as minhas dúvidas, bem como pelos sábios conselhos que asseguraram a chegada a um bom porto desta viagem de exploração que é a tese de mestrado. Naturalmente, nada disso seria possível sem a Dr. Meriem Lamghari, que me aceitou no seu grupo e me concedeu a oportunidade de fazer parte deste projeto. Como sensatas vozes antes de mim já proclamaram, mais importante do que o projeto, é a equipa por trás do mesmo. Muito obrigada a todos os membros da NESK team (Luís, Francisco, Daniela, Juliana, Carolina, Marina, Jannika, Beatriz e Carlos) por me terem acolhido tão bem e por estarem sempre prontos a ajudar uma alma em apuros. Aproveito também para deixar a minha palavra de apreço aos grupos coocupantes dos laboratórios 113S3 e 214S2, por contribuírem para o salutar ambiente de trabalho e, acima de tudo, por toda a muito boa (e menos salutar) comida. Gostaria também de fazer um especial agradecimento a todos os técnicos, em particular à Dalila Pedro, que diligentemente solucionou todos os problemas que eu lhe apresentava.

A vida dentro do laboratório e dentro deste instituto não seria a mesma sem a companhia dos meus companheiros de mestrado e da vida, biotecos de profissão e de coração (Anabela, Helena, Bó, Raio, Andreia, André, Kelly, Cortinhas, Sara, Rafa, Duarte, Francisca, Joana). Obrigada pelos abraços de compreensão nos momentos de desespero. Biotec continua a não vacilar, pode haver pânico, mas memes não irão faltar.

Porque tem de haver vida fora do i3S, para que continue a haver vida no mesmo, este trabalho não existiria sem o apoio de todos os outros amigos que me acompanharam neste percurso. Um especial obrigado às Mitocôndrias e respetivos complexos, por todos os jantares, acompanhados pelas melhores histórias e melhores frases fora de contexto. Obrigada também à toda a comunidade da “CONVERSA”, essa grande entidade eterna e sempre em crescimento (Paulo, Maggie, Leo, Cris, Marina, Carol, Alex, Ju, Marianas, Bruno, Rita, Tomás, Nuno). A vida seria certamente menos divertida sem a vossa aleatoriedade e sem a adrenalina de abrir este *chat* perto de pessoas normais. Um muito obrigada a todo o pessoal de M&B, em particular, os RS, o melhor ano que se podia pedir. Uma especial palavra de apreço à grande Ma(d)rinhas, que tem sempre as melhores conselhos, para a música e para a vida.

Quase a terminar, aproveito para agradecer àqueles que estão comigo desde um longínquo começo: Ana, Cátia, Fábio, João, Paula, Chico, Pedro, Ste, Rafaela. Vocês são definitivamente a família que eu escolhi e iremos aturar-nos até à terceira idade. Eliana, citando essa grande banda de um só êxito: estarei sempre lá para ti, porque estiveste sempre lá para mim. És a melhor melhor amiga e serei eternamente grata pelo alinhamento planetário que alinhou as nossas existências e personalidades. Por fim, um enorme obrigada à minha família, em particular à minha mãe. Não seria nada sem vocês, sem o vosso amor e apoio incondicional. Por muitos anos que viva, nunca irei retribuir tudo o que já fizeram por mim.

ABSTRACT

Breast cancer (BrCa) rises as second on the top of most deadly cancer in women worldwide. Around 75% of patients develop bone metastases and most of them experience a condition designated as cancer associated bone pain (CABP), a major life quality impairing factor. Current treatments are ineffective for half of the patients, not controlling the pain or causing side effects. The maintenance of chronic pain throughout cancer progression has been associated with the ectopic sprouting of sensory nerve fibers in the bone. The suppression of CABP after administration of specific osteoclasts (OCs) inhibitors, together with the neurotrophic potential associated with OCs secretome in physiological conditions, corroborated by the recent finding of OC-induced sensory innervation in an osteoarthritis (OA) model point to an important role for OCs in the pathophysiology of CABP. The lack of knowledge about the molecular mechanisms underlying CABP has been indicated as the main reason behind the absence of an efficient therapy. As such, the main aim of this project was understanding the crosstalk between OCs and nerve cells in the context of bone cancer pain.

The first part of this work comprised the evaluation of morphology, cell number and activity of murine OCs under tumorigenic effect, achieved by the stimulation with the conditioned media (CM) of a bone tropic BrCa cell line (4T1.2). This characterization was performed for OCs seeded on common tissue culture polystyrene (TCPS)-well plates and on bone slices, a mineralized substrate resembling the actual bone niche. Tartrate-resistant acid phosphatase (TRAP) and filamentous actin (F-actin) staining confirmed the presence of fully mature, large, multinucleated, TRAP⁺ OCs, displaying characteristic actin structures, upon stimulation with 4T1.2 CM. Notwithstanding, only the exogenous supplementation with macrophage colony-stimulating factor (M-CSF) and receptor activator of nuclear factor (NF)- κ B ligand (RANKL) enabled the utter preservation of morphology and cell number. Furthermore, cytokine supplementation was also required for maintaining OC activity, a conclusion confirmed by the quantification of TRAP activity and the percentage of eroded surface. Furthermore, exposure to 50% 4T1.2 CM resulted in resorption events with an augmented depth and volume. Additionally, the 4T1.2 cell line was characterized, revealing residual RANKL expression at the mRNA level and the absence of the correspondent protein in the CM. Combining these findings, one can hypothesize that cancer cells interact indirectly with OCs, most likely through the induced production of cytokines by osteoblasts (OBs) and/or stromal cells.

In the second part of the work, the axon terminals of murine dorsal root ganglia were stimulated with OCs and 4T1.2 CM, followed by the quantification of axonal elongation using a semi-automated software. The results revealed that BrCa cells and OCs secretome promote axonal extension at the same level as the positive stimulation with nerve growth factor (NGF). Moreover, exposure to BrCa cells' stimuli did not increase the neurotrophic potential of the secretome of OCs in comparison with the physiological status. Lastly, reverse transcription quantitative real time polymerase chain reaction (RT-qPCR) revealed that OCs expressed Netrin 1 in low levels.

All in all, the results obtained allowed a better understanding of the interaction between BrCa cells, OCs and nerve cells in the context of bone metastases. Further exploring the ability of OCs to promote axonal extension could unveil a promising therapeutic target for CABP.

INDEX

AGRADECIMENTOS.....	i
ABSTRACT.....	iii
LIST OF ABBREVIATIONS.....	vii
LIST OF FIGURES.....	ix
LIST OF TABLES.....	x
LIST OF EQUATIONS.....	x
Chapter I: INTRODUCTION.....	1
1. Skeleton: functions, structure and composition.....	3
2. Bone cells.....	5
3. Bone innervation.....	9
4. Bone metastasis.....	11
5. CABP.....	13
5.1 Nociceptive component of CABP.....	14
5.2 Neuropathic component of CABP.....	16
6. Bone pain treatments.....	21
6.1 Disease modifying agents.....	21
6.2 Analgesics.....	22
6.3 Anti-NGF treatments.....	22
Chapter II: MOTIVATION & OBJECTIVES.....	25
Motivation.....	27
Objectives.....	28
Chapter III: MATERIALS & METHODS.....	29
Interaction between BrCa cells and OCs: impact on morphology and activity.....	31
1. Cell culture.....	31
1.1 Bone tropic BrCa cell line.....	31
1.2 Murine OCs.....	32
2. OC characterization.....	35
2.1 Cell morphology.....	35
2.2 Cell activity.....	36
Evaluation of neurotrophic potential of BrCa and OCs CM.....	39
1. Preparation of microfluidic devices.....	39
1.1 Microfluidics fabrication.....	39
1.2 Coverslip preparation.....	41
1.3 Microfluidics assembling.....	41

2. Embryonic DRG culture.....	41
2.1 Isolation and seeding	41
2.2 Treatment with 4T1.2 and OCs CM	41
3. Quantification of axonal growth	43
3.1 β III tubulin immunostaining	43
3.2 Imaging and quantification with AxoFluidic software.....	43
Gene and protein expression analysis	44
1. RNA extraction and quantification	44
2. Evaluation of RNA integrity	45
3. cDNA synthesis	45
4. RT-qPCR	45
5. Quantification of RANKL in 4T1.2 secretome by ELISA	46
Statistical analysis	47
Chapter IV: RESULTS & DISCUSSION	49
Interaction between BrCa cells and OCs: impact on morphology and activity.....	52
Evaluation of neurotrophic potential of BrCa and OCs CM	70
Chapter V: CONCLUDING REMARKS & FUTURE WORK.....	81
References.....	86
APPENDIX	95

LIST OF ABBREVIATIONS

Abbreviation	Explanation
%ES	Percentage of total eroded surface
%trench surface/ES	Percentage of eroded surface represented by trenches
α – MEM	Alpha-Minimum essential medium
3D	Three-dimensional
Akt	Protein kinase B
AM	Acetoxymethyl
ANOVA	Analysis of variance
ASIC3	Acid-sensing ion channel 3
ASICs	Acid-sensing ion channels
B-27	B-27 Serum-Free Supplement
BDNF	Brain-derived neurotrophic factor
BMFs	Bone Modifying Factors
BPs	Bisphosphonates
BSA	Bovine serum albumin
BSGFs	Bone-Stored Growth Factors
CABP	Cancer associated bone pain
CaMKII	Ca ²⁺ /calmodulin-dependent protein kinase II
CAR	CXCL12-abundant reticular cell
caSR	Calcium-sensing receptor
CFU-GM	Granulocyte, Monocyte - Colony Formation Unit
CFU-S	Spleen Colony Formation Unit
CGRP	Calcitonin gene related peptide
CIC-7	2Cl ⁻ /H ⁺ -exchanger CIC-7
CM	Conditioned media
CNS	Central nervous system
CREB	cAMP responsive element-binding protein
C _T	Cycle threshold
CTR	Calcitonin receptor
DAPI	4',6'-diamino-2-fenil-indol
DCC	Deleted in colorectal cancer
DRG	Dorsal root ganglia
DTCs	Disseminated tumor cells
ECM	Extracellular matrix
EDTA	Ethylenediaminetetraacetic acid
ELISA	Enzyme-linked immunosorbent assay
EMT	Epithelial-mesenchymal transition
EP	Prostaglandin E receptor
Erk	Extracellular-signal-regulated kinase
ESMO	European Society for Medical Oncology
ET	Endothelins
ET _A R	Endothelin receptor type A
F-actin	Filamentous actin
FACIT	Fibril-Associated Collagens with Interrupted triple helices
FAK	Focal adhesion kinase
FBS	Fetal bovine serum
FDA	Food and Drug Administration
FDU	Fluoro-2'- deoxyuridine
GAPDH	Glyceraldehyde 3-phosphate dehydrogenase
GFP	Green fluorescent protein
HBSS	Hank's balanced salt solution
HSCs	Hematopoietic stem cells
IGF	Insulin-like growth factor
IL-6	Interleukin-6
IL-11	Interleukin-11
M-CSF	Macrophage colony-stimulating factor
MCT1	Monocarboxylate transport 1

MCT4	Monocarboxylate transport 4
MMP-9	Matrix-metalloprotein-9
MSCs	Mesenchymal stem cells
NcP	Nociceptive pain
NF-200	Neurofilament 200
NGF	Nerve growth factor
NpP	Neuropathic pain
NSAIDs	Non-steroidal anti-inflammatory drugs
NT-3	Neurotrophin-3
NT-4	Neurotrophin-4
OA	Osteoarthritis
OB(s)	Osteoblast(s)
OC(s)	Osteoclast(s)
OPG	Osteoprotegerin
P2X3R	Purinergic P2X3 receptor
PBS	Phosphate buffered saline
PDL	Poly-D-lysine
PDMS	Poly(dimethylsiloxane)
PFA	Paraformaldehyde
PGE2	Prostaglandin E2
PNS	Peripheral nervous system
P/S	Penicillin/streptomycin
PTH-rP	Parathyroid hormone-related protein
RANK	Receptor activator of nuclear factor (NF)-kB
RANKL	Receptor activator of nuclear factor (NF)-kB ligand
RGCs	Retinal ganglion cells
RGD	Arginine-Glycine-Aspartic Acid (aminoacidic sequence)
rpm	Rotations per minute
RT	Room temperature
RT-qPCR	Reverse transcription quantitative real time polymerase chain reaction
SIBLING	Small integrin-binding ligand, N-glycosylated
SP	Substance P
SREs	Skeletal-related events
TCPS	Tissue culture polystyrene
TGF- β	Transforming growth-factor- β
TRAP	Tartrate-resistant acid phosphatase
Trk	Tyrosine kinase
UV	Ultraviolet
V-H ⁺ -ATPase	Plasma membrane (α 3 isoform) vacuolar H ⁺ -ATPase proton pump

LIST OF FIGURES

Figure I. 1 - Cortical bone structure and components	3
Figure I. 2 - Periosteum and endosteum: spatial location in bone tissue.....	4
Figure I. 3 - Trabecular bone: morphology and structure	4
Figure I. 4 - Bone compartments in human femur.....	5
Figure I. 5 - Types of bone cells and relative location in bone tissue.....	6
Figure I. 6 - Stages of osteoclastogenesis: from bone marrow precursors to activated OCs (adapted).....	7
Figure I. 7 - Mechanisms used by OCs to degrade the mineral and the organic components of the matrix (adapted)	8
Figure I. 8 - Sensory innervation in the bone.....	10
Figure I. 9 - Vicious cycle established between OCs and cancer cells in bone metastases (adapted).....	13
Figure I. 10 - Receptors expressed by bone-innervating nociceptors.....	14
Figure I. 11 - Acidic bone environment and CABP (adapted).....	15
Figure I. 12 - Ectopic nerve sprouting and neuroma formation in murine model of prostate induced-bone cancer.....	17
Figure I. 13 - Microfluidic platforms used for the evaluation of axonal outgrowth in mouse embryonic DRG upon stimulation with mature OCs secretome.....	19
Figure I. 14 - Possible mechanism for the OC-induced sensory nerve sprouting in bone tissue in the context of OA	20
Figure III. 1 - Representative image of the 4T1.2 cell line morphology.	32
Figure III. 2 - Protocol for isolation and differentiation of murine OCs.	33
Figure III. 3 - Representative image of mature murine OCs (day 4 of cell culture).....	34
Figure III. 4 - Workflow for OC treatments.....	35
Figure III. 5 - Quantification of bone resorption.	37
Figure III. 6 - Steps for 3D reconstruction of resorption events using BonePit.....	39
Figure III. 7 - Steps for microfluidic fabrication.....	40
Figure III. 8 - Experimental setup for axonal simulation with CM.....	42
Figure III. 9 - Steps for axonal outgrowth quantification with AxoFluidic	44
Figure IV. 1 - Representative images of OC morphology in each condition after TRAP staining (Day 4).....	53
Figure IV. 2 - Representative images of characteristic actin structures found in OCs.	53
Figure IV. 3 - Representative images of OC morphology in each condition after F-actin immunostaining (Day 4).....	54
Figure IV. 4 - Evaluation of cell number after treatment with 4T1.2 CM.	55
Figure IV. 5 - Representative images of toluidine blue stained bone slices for each condition (Day 4, 6 h of stimulus).....	56
Figure IV. 6 - Effect of 4T1.2 CM on OC activity (Day 4, 6 h of stimulus).	57
Figure IV. 7 - Impact of longer stimulus in the depth of impressions left by OCs.....	58
Figure IV. 8 - Representative images of toluidine blue stained bone slices for each condition (Day 5, 24 h of stimulus).....	59
Figure IV. 9 - Effect of 4T1.2 CM on OC activity (Day 5, 24 h of stimulus).	59

Figure IV. 10 - Impact of longer stimulus in %ES.....	60
Figure IV. 11 - Representative 3D reconstructions of resorption events obtained using BonePit.	62
Figure IV. 12 - Quantification of morphologic parameters in 3D reconstructions of resorption events using BonePit.....	63
Figure IV. 13 - Quantification of TRAP activity in OCs CM.....	64
Figure IV. 14 - RANKL expression levels in the 4T1.2 cell line.	66
Figure IV. 15 - Assessment of the neurotrophic potential of 4T1.2 cell line and OCs CM.	71
Figure IV. 16 - Assessing how 4T1.2 secretome impacts OCs neurotrophic potential.....	73
Figure IV. 17 - Impact of bone matrix degradation products in the neurotrophic potential.	74
Figure IV. 18 - Evaluation of the tumorigenic effect in the axonal outgrowth for OCs seeded on a mineralized substrate.....	76
Figure IV. 19 - Comparison between Netrin 1 expression and the neurotrophic potential.	78

Figures I.1, 5, 6, 7, 9 and 11, as well as Figures III. 2, 4 and 8 were created with images from Servier Medical Art by Les Laboratoires Servier. Original images are licensed under a Creative Commons Attribution 3.0 Unported License. Figures IV.16 and 18 also made use of this image database.

LIST OF TABLES

Table III. 1 - Summary of experimental conditions used for the evaluation of the paracrine effect of 4T1.2 cells on OCs.	34
Table III. 2 - Experimental conditions used for the evaluation of neurotrophic potential.	42
Table III. 3 - Pairs of primers used in RT-qPCR analysis.....	46
Table III. 4 - List of reagents used for the experimental work	48

LIST OF EQUATIONS

Equation 1:	37
Equation 2:	37
Equation 3:	46

Chapter I:

INTRODUCTION

1. Skeleton: functions, structure and composition

The human skeleton comprises individual or fused bones that interact with cartilage, ligaments, tendons and muscles. The skeleton is necessary for vital functions that can be divided into three categories: mechanical, metabolic and cellular proliferation. Mechanical functions involve giving structural support for the body, protecting the internal organs and allowing locomotion. Maintenance of mineral (calcium and phosphate) and acid-base homeostasis, along with storage and release of both growth factors and cytokines represent the main metabolic functions. Concerning cell proliferation, hematopoiesis (blood cell production and maturation) and the differentiation of bone cells happen in the bone marrow.¹⁻⁴

Bone is a rigid organ composed by an elastic and flexible organic matrix (represents 20-40% of bone tissue), combined with a mineral part (50-70% of bone tissue), which provides rigidity and load-bearing strength.¹ The mineral (or inorganic) phase consists of hydroxyapatite [$\text{Ca}_{10}(\text{PO}_4)_6(\text{OH})_2$] crystals with minor quantities of carbonate, magnesium and acid phosphate. Regarding the organic matrix, collagen type I is the most abundant protein, whereas collagen types III, V and fibril-associated collagens with interrupted triple helices (FACIT) are found in traceable quantities.¹ Despite their reduced content, FACIT collagens play a vital role in the stability and organization of the extracellular matrix (ECM), because they link collagen fibers with each other and with other ECM non-collagenous components.⁵ Overall, collagenous proteins account for 85-90%, with non-collagenous proteins making up the remaining 10-15%. Non-collagenous components comprise serum proteins (such as albumin), glycosaminoglycan-containing proteins and leucine-rich repeat proteins (e.g. aggrecan, versican, biglycan, hyaluronan), glycoproteins (alkaline phosphatase and osteonectin), small integrin-binding ligand, N-glycosylated (SIBLING) proteins (osteopontin and bone sialoprotein), RGD-containing glycoproteins (such as fibronectin and vitronectin) and γ -Carboxy glutamic acid-containing proteins (including matrix Gla-protein, osteocalcin and protein S). The specific functions of each component are not yet completely defined. OBs and osteocytes, bone cells which will be further explored later on, are responsible for secreting matrix components that can be organized into two different patterns – cortical (or compact) bone or cancellous (trabecular or spongy) bone.^{1,6}

The solid and smooth appearance associated with bone is given by the dense cortical bone, which constitutes their outer layer and accounts for 80% of the adult human skeleton.¹ Cortical bone consists of multiple columns called osteons (**Figure I. 1**); each osteon is composed of concentric layers of mineralized matrix (lamellae) intertwined by osteocytes and OBs around a central canal designated as Haversian canal⁷ (as a consequence, the cortical osteon might also be called Haversian system). Haversian canals contain blood and lymphatic vessels, as well as nerves. Different osteons can communicate because they are

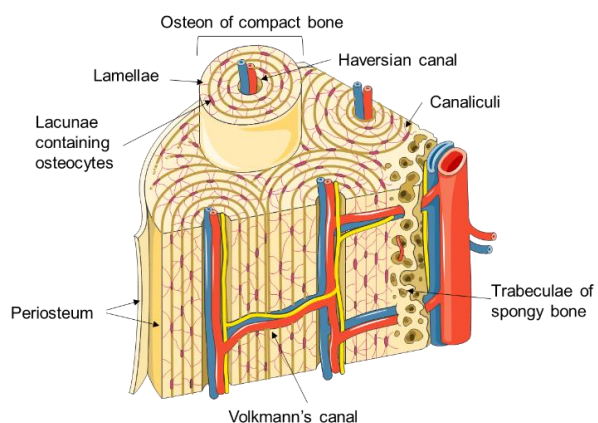


Figure I. 1 - Cortical bone structure and components (adapted).⁶ The lamellae forming the cortical bone create a typical architecture perceived both from a longitudinal and a cross-sectional point of view.

connected by Volkmann's canals (also referred as perforating canals).⁶ Cortical bone's outer surface is covered by the periosteum (with exception of joints, where bone is coated with articular cartilage), whereas its inner surface is covered by endosteum (**Figure I. 2**). Periosteum is a membrane of fibrous connective tissue divided into the fibrous layer (more external, rich in fibroblasts) and the cambium or cellular layer (inner layer, contains progenitor cells that develop into OBs).^{1,6} Periosteum is characterized by a dense vascular and nervous network.⁸ Endosteum corresponds to a single layer of bone-lining cells supported by a thin sheet of reticular connective tissue, together composing a membrane that lines the medullary cavity.^{1,8,9}

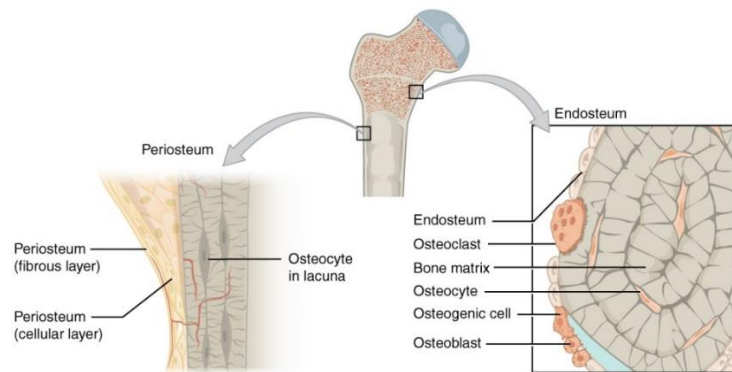


Figure I. 2 - Periosteum and endosteum: spatial location in bone tissue.⁶ Periosteum and endosteum correspond to the outer and inner bone lining membranes, respectively. Both contain cells embedded on connective tissue, but periosteum is a bilayer, whereas endosteum is a monolayer. While periosteum is absent at the joints, endosteum occurs in all bones.

On the other hand, trabecular bone (**Figure I. 3**), which comprises the remaining 20% of the adult human skeleton, is less dense than cortical bone due to its porous morphology (higher surface area to volume ratio). Osteon remains the structural unit; nevertheless, in the cancellous bone, the mineralized matrix shapes into plates and rods, defining a network called trabeculae (singular = trabecula). Each trabecula forms in the direction of applied tension in order to assure bone's ability to bear mechanical stress. Pores defined by the trabeculae often contain red marrow where hematopoiesis occurs^{1,6}.

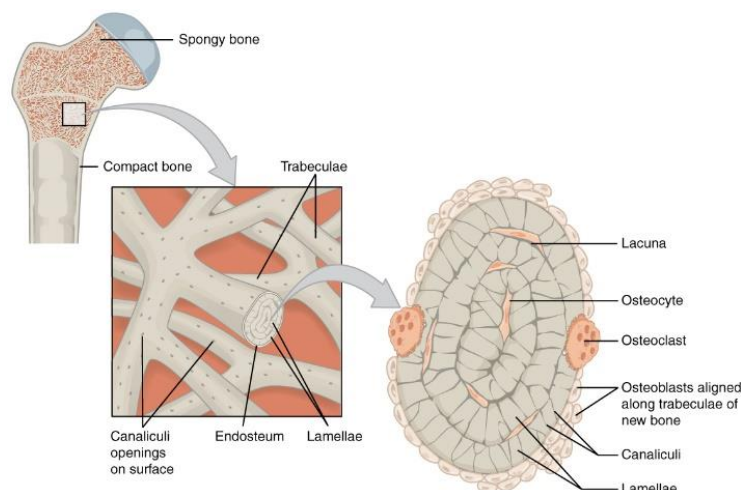


Figure I. 3 - Trabecular bone: morphology and structure.⁶ While the typical architecture of the cortical bone is characterized by the tubular and well-defined nature of osteons, trabecular bone is designed as an intricate network.

Bones can be classified into 5 types considering their size and shape – long, short, flat, sesamoid and irregular. Long bones (e.g. clavicles, femurs, tibiae) are the ones with the most standardized structure (**Figure I. 4**). A long bone is divided into 2 main parts: the proximal and distal ends are called epiphyses (singular = epiphysis) and the tubular shaft between them diaphysis. Diaphysis' walls are composed of compact bone, while its core is filled with bone marrow (medullary cavity). Trabecular bone can be found at the epiphyses (it is also present near joints in the interior of vertebrae).¹

Bone marrow is a spongy tissue that can be found in the center of long bones or in cancellous bone portions. It represents the primary site for hematopoiesis, enclosing not only hematopoietic cells, but also adipocytes and supportive stromal cells. Two main types of bone marrow are differentiated considering fat content and vascularization: red and yellow bone marrow, with the first being converted to the second throughout lifetime. Yellow bone marrow is poorly vascularized and predominantly constituted by adipocytes (80% fat, 15% water and 5% protein). On the other hand, red bone marrow is highly vascularized, thus enriched in hemoglobin and erythrocytes (responsible for its red color), and has a lower fat content (only 40-60% of lipid content).¹⁰

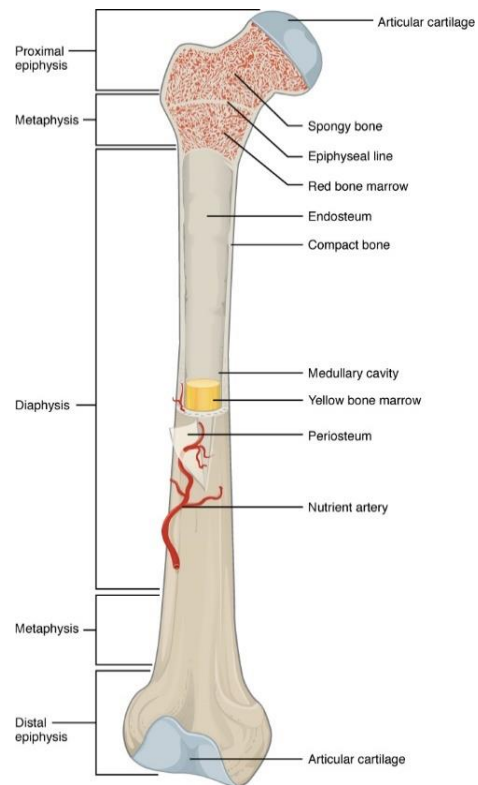


Figure I. 4 - Bone compartments in human femur.⁶ Trabecular bone is mainly observed in epiphyses, while cortical bone covers bone marrow in the diaphysis. Metaphysis is the short portion that corresponds to the transition between the epiphysis and the diaphysis.

In order to provide an appropriate support at mechanical, metabolic and cellular levels, the skeleton must change throughout life to adapt to the body's changes and growth. Bone must follow these changes.⁴ Therefore, it is a dynamic tissue, undergoing constant modelling and remodeling during life (turnover rate of the whole skeleton is around 10% per year).¹¹ Bone modelling, the prevailing process during childhood, corresponds to the modification of bone's shape or size in response to physiological and mechanical conditions to which the skeleton is submitted. Bone remodeling comprises the elimination of old bone and its substitution by new and healthier bone, avoiding the cumulation of microdamage in the skeleton. This process starts before birth and lasts until death, assuming a predominant role during adulthood.¹² Remodeling implies a controlled equilibrium between bone formation and resorption, carried out by OBs and OCs, respectively.¹³

2. Bone cells

Cells represent a small percentage of the bone (around 10%). Nevertheless, they are of paramount importance for bone formation, maintenance and function. OBs, bone lining cells, osteocytes and OCs correspond to the main cell categories.¹⁴ Each cell category has different functions and a specific spatial location in accordance with said functions (**Figure I. 5**).

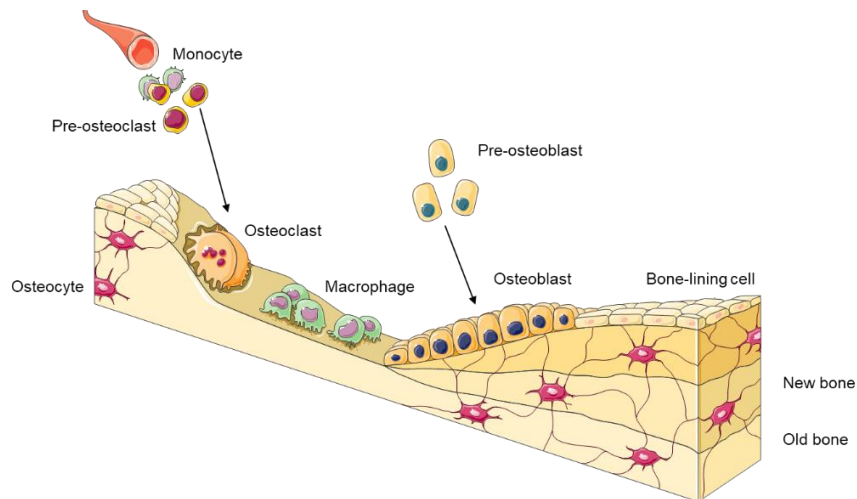


Figure 1.5 - Types of bone cells and relative location in bone tissue (adapted).⁶ Osteocytes are entrapped within the bone matrix and are responsible for maintaining the bone tissue itself. OBs are the bone forming cells, whilst OCs play the opposite role, as they are the only bone resorbing cells. Bone-lining cells cover the bone surface and are located on top of a thin layer of non-mineralized collagen matrix.

OBs result from the differentiation of a small bone marrow-resident population of pluripotent mesenchymal stem cells (MSCs), committed to the OB lineage due to signaling involving the canonical Wnt/ β -catenin pathway and associated proteins.^{1,13} These cells can be found on bone surface (both trabecular and cortical bone), inclusively in the periosteum and endosteum. OBs are responsible for bone deposition, synthesizing and secreting collagenous proteins (particularly collagen type I, as it corresponds to the most abundant component). In addition, mineralization occurs by the release of OB-derived vesicles with high concentration of calcium and phosphate, along with mineralization inhibitors (e.g. pyrophosphate or proteoglycans) to regulate the mineralization rate.^{1,12} As the vesicles content is released, the matrix is gradually mineralized, forming new bone and entrapping OBs within it. Subsequently, their organelles and cytoplasm are reduced up to 70%. Additionally, they assume a star-shaped appearance as long dendritic-like processes appear, becoming osteocytes. Osteocytes, which represent 95% of all bone cells, are located in spaces called lacunae (singular = lacuna).¹² Despite being surrounded by bone tissue, osteocytes receive nutrients and eliminate metabolic waste using cytoplasmic processes that extend from the cells through the canaliculi found in bone matrix. These canaliculi allow the communication with other osteocytes in the bone tissue, or with OBs and bone-lining cells on the bone surface, forming the lacunar-canalicular network.^{1,6,12} Osteocytes detect mechanical and metabolic signals, upregulating or downregulating OBs activity in accordance.^{12,13} OBs and osteocytes do not divide because they lost their mitotic activity.¹⁴

Bone-lining cells are post-mitotic flat-shaped OB-derived cells found in the endosteum, covering the bone where neither bone resorption nor bone formation occurs. Their functions are not yet fully understood.^{1,14} However, it was proposed that they control the inflow and outflow of mineral ions from the bone extracellular fluid, acting as a selective barrier. These cells can dedifferentiate into OBs in the presence of parathyroid hormone (PTH) or under the effect of mechanical forces.¹

OCs derive from bone marrow hematopoietic stem cells (HSCs)⁴ through precursors from the monocyte-macrophage lineage, which upon stimulation with M-CSF upregulate the expression of essential OC genes, committing to the osteoclastic lineage and differentiating into preosteoclasts¹⁵ (**Figure I. 6**). M-CSF, which is mainly secreted by bone marrow stromal cells and OBs, is responsible for increasing the expression of the receptor activator of nuclear factor (NF)- κ B (RANK), the osteoclastic receptor for RANKL, the other key cytokine involved in osteoclastogenesis (i.e. OC formation). RANKL is secreted by OBs, osteocytes, bone-lining cells and stromal cells.¹⁴ RANKL cytokine is produced both in membrane-bound and soluble forms that interact with membrane-bound RANK receptor in nearby preosteoclasts.¹³ The combined action of M-CSF and RANKL stimulates the fusion of said preosteoclasts, resulting in mature, multinucleated OCs.^{12,15,16} The extent of mature OCs' activation and function is regulated by the ratio between RANKL and osteoprotegerin (OPG), a soluble decoy receptor that binds to RANKL with high affinity, preventing it from reaching RANK receptors.^{12,15}

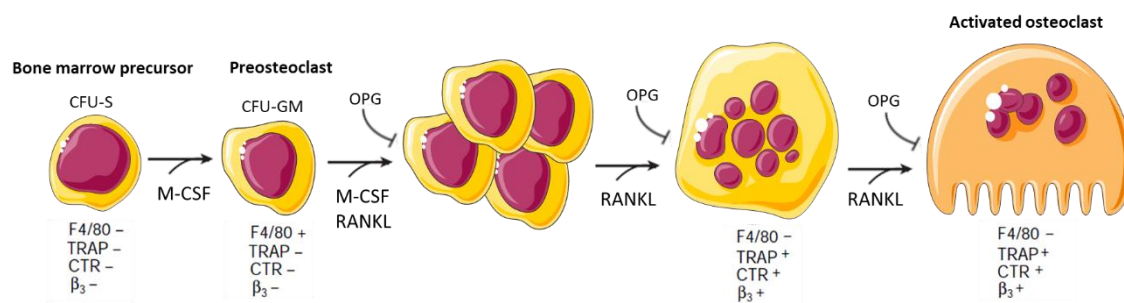


Figure I. 6 - Stages of osteoclastogenesis: from bone marrow precursors to activated OCs (adapted).¹⁵ Mature activated OCs are characterized by their large diameter (50-100 μ m), the presence of several nuclei and the abundance of mitochondria, lysosomes and free ribosomes in the cytoplasm. At the interface between the OC and the bone matrix, the membrane assumes the shape of finger-like projections, creating a ruffled border, another main distinctive feature of this cell type.¹¹ F4/80 is a major murine macrophage marker; TRAP, β_3 integrin (β_3) and calcitonin receptor (CTR) are genes that define the OC lineage. CFU-S: Spleen Colony Formation Unit; CFU-GM: Granulocyte, Monocyte - Colony Formation Unit

Mature OCs activation is only completed when they bind to the bone matrix via integrin receptors; in particular, $\alpha_v\beta_3$ integrin interacts with osteopontin and bone sialoprotein, while the β_1 family of integrin receptors link OCs to collagen, fibronectin and laminin. Binding to the matrix triggers OCs polarization and allows bone resorption to start. The interaction involving $\alpha_v\beta_3$ integrin is of pivotal importance for bone resorption stimulation.¹ In contrast with most cells, polarized OCs bind to ECM not by focal adhesions, but through podosomes, adhesive structures formed by a ring of integrins and cytoskeletal proteins around an actin core; podosomes appear as dot-like rings along cell borders.^{1,12,15} Resorption implies an extreme microenvironment conceived for bone destruction, therefore the process must occur in a restricted area to avoid excessive damage to bone tissue. As such, polarization involves the rearrangement of cytoskeletal F-actin to circumscribe the bone-resorbing compartment (also designated as resorption lacuna), isolating it from the surrounding bone tissue – formation of the sealing zone.^{1,12} In addition to podosomes, actin rings are also typically observed around cell nuclei, both contributing for the establishment of the sealing zone. Filopodia correspond to another important structure that appears as a consequence of the cytoskeleton rearrangement that marks the transition from non-resorbing to resorbing OCs. Filopodia are cellular projections comprised by actin clusters and are used for cell migration. Filopodia, podosomes and actin rings

are very useful structures to identify fully polarized OCs¹⁷ and are detectable in TCPS seeded OCs.^{18,19}

Resorbing OCs must degrade both the mineral and the organic parts of the matrix (**Figure I. 7**). Minerals are dissolved due to the release of protons (H^+) and chloride ions (Cl^-) via the plasma membrane (α_3 isoform) vacuolar H^+ -ATPase proton pump (V- H^+ -ATPase) and the $2Cl^-/H^+$ -exchanger CIC-7 (CIC-7), respectively. Consequently, an acidic environment is created, and pH can drop until 4,5. On the other hand, TRAP, cathepsin K, matrix metalloproteinase 9 (MMP-9) and gelatinase are secreted in vesicles to digest the organic components.^{16,20,21} The vesicles have to fuse with the OCs membrane to release its content into the bone-resorbing compartment, creating the characteristic ruffled border of polarized OCs.¹² Acid phosphatases correspond to a family of ubiquitous lysosomal enzymes, which have optimal activity in an acidic environment. TRAP, a member of this family of enzymes, is found not only in bone, but also in spleen and lungs.²² However, the isoenzyme 5b is bone specific; for that reason, it has been extensively used as a biochemical marker of bone turnover and as an osteoclastic specific marker.²²⁻²⁵ Indeed, it is well acknowledged that increased OC activity implies an increased synthesis and secretion of TRAP5b. Accordingly, the rate of TRAP synthesis and its accretion in body fluids correlates with the rate of bone resorption.²⁵ The quantification of TRAP activity is particularly relevant in the scenario of disease, since its serum levels appear to be a good marker to diagnose and quantitatively monitor metabolic bone disorders involving increased resorption (such as bone metastasis or osteoporosis, for instance).^{23,25} Its substrate is not completely clear, because TRAP is a non-specific phosphoprotein phosphatase. Nonetheless, considering it acts by catalyzing the release of phosphate groups from proteins, osteopontin, bone sialoprotein and osteonectin are all possible substrates present in the bone matrix. Thus, TRAP plays a major role during the degradation of the organic components.²⁵

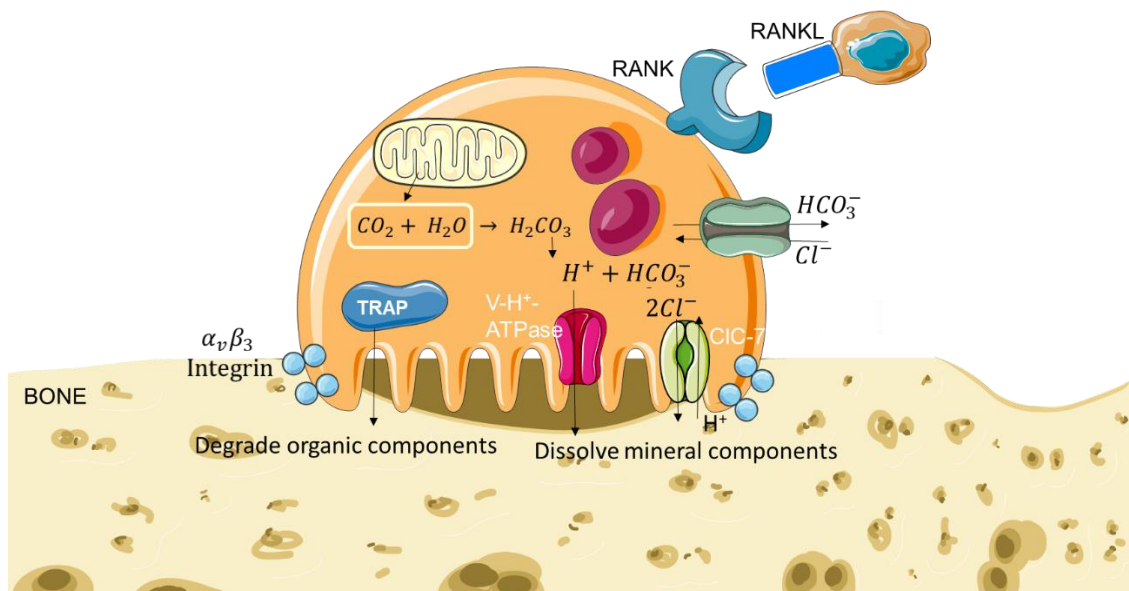


Figure I. 7 - Mechanisms used by OCs to degrade the mineral and the organic components of the matrix (adapted).²⁰ The carbon dioxide (CO_2) produced during aerobic respiration in the mitochondria is converted to carbonic acid (H_2CO_3) by the enzyme carbonic anhydrase II and, subsequently, results in protons and bicarbonate ions (HCO_3^-). The resulting protons are released into the bone matrix through the V- H^+ -ATPase, to degrade the mineral components. On the other hand, to avoid cytoplasm's excessive alkalization, the bicarbonate ions are removed through a basolateral HCO_3^-/Cl^- anion exchanger. Chloride ions are released to the extracellular matrix through the CIC-7 present in the basal membrane.

3. Bone innervation

In physiological conditions, the nervous system receives signals from different parts of the body and sends back signals in response to the detected environmental changes, assuring homeostasis. In vertebrates, the nervous system branches into two components: the central nervous system (CNS) and the peripheral nervous system (PNS). CNS comprehends the brain, the brainstem, the cerebellum and the spinal cord. On the other hand, PNS is composed by nerves and ganglia (singular = ganglion) that innervate organs and limbs, establishing the communication between CNS and the rest of the body.²⁶ The fundamental unity of the nervous system is the neuron (or nerve cell), a specialized cell that receives and transmits information through electrical signals called nerve impulses or action potentials. Neurons have a typical structure that can be divided into the following segments: the cell body or soma (containing the nucleus and other organelles), the dendrites (short cytoplasmic extensions that branch out from the cell body) and the axon (long cytoplasmic extension that leads the nerve impulse from the cell body).²⁶ Nerves are essentially bundles containing axons from neurons whose cell bodies usually lie on the CNS. Ganglia are nodules (clusters) of neuron cell bodies located outside the brain and spinal cord.²⁷ PNS is itself divided into two components – somatic (includes sensory and motor nerves) and autonomic (comprising sympathetic, parasympathetic and enteric systems).²⁶

As most living tissues, bone is innervated by peripheral nerves. Both sensory and sympathetic innervation have been detected within the tissue, but afferent sensory nerve fibers, which are involved in nociceptive signaling (i.e. recognition of noxious mechanical, chemical or thermal stimuli that are transmitted to the CNS, creating the sensation of pain) are more relevant within the present framework. Sensory neurons associated to sensory nerve fibers are designated as nociceptors. The sensory fibers that innervate the bone tissue (**Figure I. 8**) correspond to bundles of axons whose cell bodies are located on the dorsal root (or spinal) ganglia (DRG) that occupy the dorsal roots along the vertebral column.^{26,28} Each sensory neuron of the DRG will ultimately conduct the somatosensory information detected by the peripheral nerves to the brain, where it is processed and analyzed, creating the perception of pain.^{2,27} Bone tissue is predominantly innervated by thinly myelinated A-delta ($A\delta$) fibers (type III afferent fibers) and peptide-rich unmyelinated C-fibers (type IV afferent fibers).^{2,20,29,30} This classification is based on the diameter, myelination status and velocity of conduction of each fiber type. $A\delta$ fibers are thicker (6-8 μm versus < 1 μm , rat) and faster conducting (10-15 m/s versus 1-2 m/s, rat) than C-fibers (the lower the degree of myelination, the lower the conduction velocity). These properties condition fibers' functions – noxious stimuli detected by $A\delta$ fibers originate a sharp and fast pain sensation, while those detected by C-fibers are associated with a dull, aching, slow burning pain.³⁰ Both $A\delta$ and C fibers were identified in the periosteum, bone marrow and cortical bone, but the innervation density varies with the compartment.⁸ The ratio of relative density in periosteum, bone marrow and cortical bone is approximately 100:2:0.1, respectively.^{2,31-33}

While size, myelination status and velocity of conduction are relevant properties to define the functional category of nerve fibers, the use of molecular markers is of uttermost importance to properly identify the subpopulations of sensory neurons that innervate bone, since the nociceptors correspond to a very heterogeneous cell population. These markers can

be either expressed on neurons' cell bodies (in the DRG) or on the nerve terminals in bone tissue.³⁰ Neurofilament 200 (NF-200), substance P (SP), calcitonin gene related peptide (CGRP) and tyrosine receptor kinase A (TrkA) represent the most relevant and commonly used molecular markers for the characterization of sensory nerve fibers. NF-200 is specific for neurofilaments with high molecular weight (200 kDa), a class of intermediate filaments particularly profuse in the axons of DRG neurons. Hence, despite being often described as a general neuronal marker, NF-200 assumes particular interest in the study of sensory innervation.^{34,35} Nociceptors are excitatory neurons, therefore their signaling process involves the release of glutamate (the most abundant excitatory neurotransmitter), but also peptides, such as SP, CGRP and somatostatin.^{4,36}

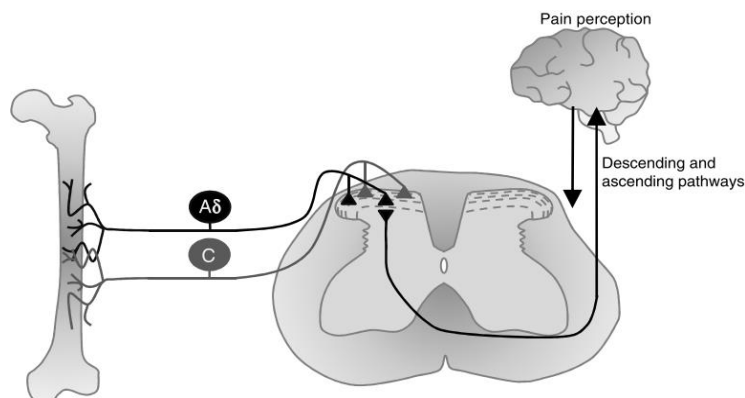


Figure 1. 8 - Sensory innervation in the bone.²⁹ Each sensory neuron of the DRG conducts the somatosensory information detected by the peripheral nerves to the brain (ascending pathway), where it is processed and analyzed, creating the perception of pain (descending pathway).

In addition to neurotransmitters and peptides, other molecules involved in cell communication in the nervous system can be used to categorize neurons. Neurotrophins, a family of small proteins critical during the development of the vertebrate nervous system, are possible candidates. They promote neuronal outgrowth and survival, influencing plastic and pathological processes. Neurotrophins are of key importance for the maintenance of nerve cells and have been appointed as mediators of neurotransmitter release.³⁷ NGF, brain-derived neurotrophic factor (BDNF), neurotrophin-3 (NT-3) and 4 (NT-4) are examples of neurotrophins. Their action is mediated through two different types of cell surface receptors - tyrosine kinase (Trk) or p75 receptors.^{38,39} Tyrosine receptors are particularly interesting, since they can be used to segment sensory neurons into three functionally distinct populations: TrkA is expressed in neurons detecting heat or noxious mechanical forces (which usually result in the sensation of pain), TrkB⁺ neurons perceive innocuous mechanical forces and TrkC⁺ neurons sense changes in muscles length. In particular, TrkA has a high affinity for NGF, hence it is recognized as its cognate receptor.^{40,41} NGF tropic signaling is vital for neuron survival, as well as for their ability to extend axons, both *in vivo* and *in vitro*.⁴² In fact, NGF knockout mice experienced the loss of unmyelinated and thinly-myelinated TrkA⁺ nociceptors.⁴³ Myelinated Aδ fibers represent the most abundant category of sensory nerve fibers in the bone- 75% *versus* 25% of peptide rich C-fibers. Within each of these categories, different populations have been identified according to the molecular markers expressed, so the overall distribution of sensory nerve fibers in bone tissue is the following: 60% of NF-200⁺, TrkA⁺, CGRP⁺ (Aδ fibers), 15% NF-200⁺, TrkA⁻ (Aδ fibers), 20% CGRP⁺, TrkA⁺ (peptide rich C-fibers) and <5% CGRP⁺, TrkA⁻ (peptide rich C-fibers).^{29,44}

4. Bone metastasis

A neoplasm (commonly designated as tumor) is an abnormal cell mass that results either from the excessive proliferation or insufficient death of anomalous cells. If the cell mass is able to invade and/or destroy the surrounding tissue, it is classified as malignant tumor or cancer.⁴⁵ The most straightforward classification system for cancer is based on the tissue/organ where the primary tumor is formed (e.g. if it appeared in the breast tissue, the malignant tumor will be designated as BrCa). If tumor cells successfully escape the primary tumor and establish neoplasms in other organs (secondary tumors), those tumors are designated as metastases. The metastatic spread of tumors is a 4-step process: (1) local ECM suffers alterations that allow the dissemination of tumor cells in the periphery of the neoplasm (invasion); (2) disseminated tumor cells (DTCs) enter circulation (intravasation); (3) DTCs leave circulation (extravasation); (4) DTCs occupy a new organ and form a new cell mass (metastasis). Each type of tumor has a different pattern of dissemination. Bone is a preferential metastatic site for solid tumors, in particular for breast and prostate cancer.⁴⁶⁻⁴⁸ Lung cancer often metastasizes to the bone as well. Bone metastases significantly worsen prognosis, leading to higher mortality⁴⁹ and decreasing patients' life quality, as they result in skeletal-related events (SREs) (fractures, spinal cord/intervertebral nerve compression, hypercalcemia) and cause pain.⁵⁰ The axial skeleton, comprising spine, ribs and pelvic bones, is the most frequently metastasized bone area (correlates with the localization of red bone marrow in adult skeleton).^{13,46}

The unique bone microenvironment is highly attractive for tumor cells, which hijack several bone marrow functions, thus creating the most suitable "soil" for their homing, seeding and proliferation.^{46,47,51} The wide set of functions served by the skeleton (e.g. hematopoiesis, osteogenesis, regulation of metabolic and mineral homeostasis) asks for a heterogeneous cell population, particularly in the bone marrow, where hematopoiesis occurs. In fact, the bone marrow contains HSCs, OCs, macrophages, lymphocytes (hematopoietic origin); MSCs, OBs, adipocytes (mesenchymal origin); endothelial cells, nerve cells, CXCL12-abundant reticular (CAR) cells, among others.^{46,51} In order to maintain an appropriate organization to support cell function for all the aforementioned cell types, an intricate ensemble of growth factors, cytokines and chemokines creates a unique microenvironment (bone niche) that regulates the dynamic balance between all bone components. Predictably, given the profusion of cell communication mediators (growth factors, cytokines, chemokines) involved in the modulation of bone niche, cancer cells are drawn to this microenvironment.⁵² Following bone niche invasion, cancer cells end up interfering with bone niche modulation, ultimately disturbing the physiological bone homeostasis, in particular, the equilibrium between bone deposition and resorption.⁵³ Bone metastases can have an osteolytic (simultaneously stimulate bone-resorption and/or block bone formation) or osteoblastic (stimulate bone-formation and/or impair bone resorption) profile, resulting in weakened or excessively built-up bone, respectively. A mixed profile (osteolytic/osteoblastic) is also a possibility for some cancers.⁴⁷

Cancer cells are primed to occupy and metastasize the bone (homing) by chemotaxis involving a gradient of chemokines. CXCL12 (produced by MSCs, endothelial cells, CAR cells, OBs and other bone marrow stromal cells) is involved in the major signaling pathway. It binds to the CXCL12 receptors CXCR4 and CXCR7 expressed by cancer cells. Additionally, CCL-2 and CCL-22 also seem to play a part in the process of bone homing.⁴⁶ Once in the bone, cancer cells assure

definite residence in the tissue (seeding) by promoting a firm adhesion to the bone stroma and bone matrix mediated by integrins.⁴⁶ When adhesion is established, metastatic cancer cells interfere with bone homeostasis, favoring bone lysis or growth to enable metastatic outgrowth in the bone.

Bone metastases are present in around 70-100% of patients with prostate cancer.⁴⁷ Pelvic and long bones, vertebral column, and ribs are preferentially occupied. Prostate cancer derived bone metastases have a differentiating feature, as they typically have an osteoblastic profile.^{32,47} Regarding lung cancer, although not the most common site of metastasis, bone is affected in 40% of the cases.⁴⁹ Most importantly, bone metastases are associated with shorter survival in comparison with metastases in the nervous system (the preferential metastatic site, affected in 47% of the patients). Osteolytic or mixed (osteolytic/osteoblastic) lesions are the common result of lung cancer metastases.^{47,49} BrCa is particularly worrisome for several reasons. Firstly, it is the second most deadly cancer in women, with 626 679 deaths registered worldwide until September of 2018.⁵⁴ Secondly, 75% of advanced BrCa cases develop metastases in the skeleton and 80% of BrCa patients who die have bone metastases. Adding to this, BrCa incidence is increasing hand-in-hand with survival times. Lastly, a significant part of BrCa patients are young women (20-44 years old) in their working age and/or raising a family. BrCa-derived metastases are usually osteolytic, significantly contributing to increase morbidity and mortality.⁴⁷ They stand out as a paradigmatic example of “seed and soil” interactions between tumor and stroma cells.

Cancer cells release bone modifying factors (BMFs), such as parathyroid hormone-related protein (PTH-rP), prostaglandin E₂ (PGE₂), interleukin-6 (IL-6) and interleukin-11 (IL-11). BMFs increase OCs' differentiation, proliferation and activation both directly and indirectly, with the latter form of interplay assuming greater relevance.¹¹ In fact, PTH-rP released by cancer cells binds to its receptor, which is expressed by OBs, consequently increasing their production of RANKL and diminishing the release of OPG.^{53,55} Osteocytes are also altered by the tumor products, increasing the synthesis of RANKL, further contributing to foster osteoclastogenesis.⁵³ The increase in OCs proliferation translates into enhanced bone resorption, during which bone-stored growth factors (BSGFs), such as insulin-like growth factor (IGF) and transforming growth-factor- β (TGF- β), are released from the ECM. BSGFs promote epithelial-mesenchymal transition (EMT), creating cancer cells with a mesenchymal-like profile and, consequently, more capable of invasion. Simultaneously, BSGFs inhibit apoptosis, stimulating bone colonizing cancer cells to proliferate and release BMFs^{20,32,56}. Thus, a vicious cycle is established (**Figure I. 9**). Bone destruction results in weakened bone; hence, skeletal fractures, spinal instability, decreased mobility and significant skeletal pain are often experienced.⁴⁴

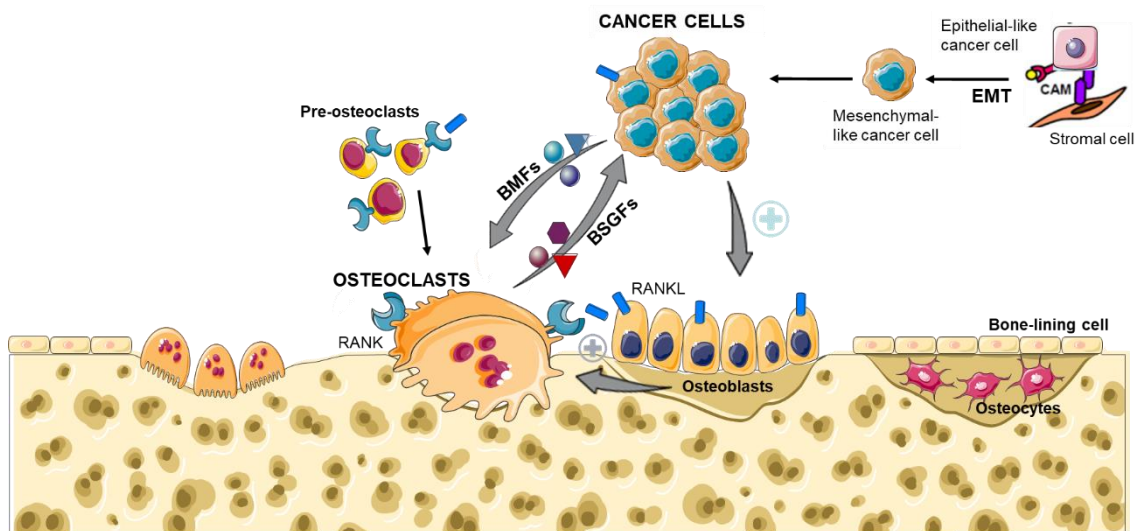


Figure 1. 9 - Vicious cycle established between OCs and cancer cells in bone metastases (adapted).²⁰ Cancer cells promote bone destruction by releasing BMFs (PTH-rP, IL-6 or IL-11), which enhance the production of RANKL in OBs, bone lining cells, osteocytes and stromal cells.^{20,32,56} RANKL interacts with the RANK receptor expressed by OCs, resulting in the increased osteoclastic activity observed in bone metastases.

5. CABP

There is a long list of conditions that cause skeletal pain, namely, osteoporosis, OA, trauma-induced fracture, spinal cord injuries or metastatic cancers.² CABP aggravates morbidity and mortality, reducing patients' quality of life.²⁰ Bone pain is commonly originated by metastatic cancer: between 75 and 90% of patients with metastatic-stage cancer will suffer from CABP.^{32,57} Most importantly, 50% of cases are not solved by current treatments.^{30,31}

Two main types of CAPB have been described: ongoing and breakthrough. It is not yet clarified if the two types of pain result from the exact same mechanism. Ongoing pain can be the first sign of cancer, it is the most frequent and it is described as dull and gradually increasing in intensity with time. As cancer evolves, intermittent episodes of pain can occur without any obvious precipitating event (spontaneous breakthrough pain) or be provoked by the movement of the tumor-bearing organ (movement-evoked breakthrough pain). Classification as breakthrough refers to the ability of disrupting the analgesic regimen applied to the patient to control the ongoing pain. Breakthrough pain can occur several times per day, lasts from seconds to minutes, it is usually more severe and it is most difficult to control, involving the administration of higher doses of opioids, often followed by adverse effects (depression, cognitive impairment, somnolence).^{31,58} Available bone pain treatments and associated side effects will be further explored in a latter section.

Another relevant pain classification distinguishes between nociceptive and neuropathic pain, using as classification criterion the pain's origin. Nociceptive pain (NcP) is caused by tissue damage or potentially noxious stimuli, detected by peripheral neural pathways. Stimulation of nociceptors triggered by augmented levels of proinflammatory cytokines (chemical noxious stimuli) corresponds to one of the mechanisms behind NcP.⁵⁹ On the other hand, neuropathic pain (NpP) is a chronic condition provoked by lesions or dysfunctions in the nervous system, which result either in excessive stimulation or damaged inhibitory pathways. Activation of neuromas, sprouting of primary afferent axon terminals or the interaction between sympathetic

and somatosensory afferents are possible mechanisms behind NpP.⁶⁰ In a simplistic view, nociceptive pain is predominantly caused by chemical mediators, while neuropathic pain is triggered by distorted electrical events.⁵⁷ Nociceptive, as well as neuropathic (both acute and chronic) pain have been described in cancer patients.^{29,44,60,61} Comprehensive studies for the analysis of cancer pain revealed that NcP is the predominant type, as it is presented by 65-75% of the patients.^{62,63} Nociceptive bone pain is triggered by the algogenic mediators secreted by tumor and associated stromal cells, acidosis and abnormal mechanical pressure that leads to distended sensory nerve fibers.^{29,44} Regarding the neuropathic component of bone cancer pain, two major mechanisms have been proposed: injury and destruction of nerve fibers promoted by tumor growth; extensive pathological sprouting and neurochemical reorganization of sensory and sympathetic fibers innervating tumor-bearing bone.^{44,60,61} The etiology of bone cancer pain is still not completely understood, given its complex profile that involves two different components - nociceptive and neuropathic – which can even coexist. CABP's complexity is further aggravated by the different mechanisms behind each pain component, as well as for the pain's changing nature and frequency throughout the disease.

5.1 Nociceptive component of CABP

The nociceptive component of CABP is particularly relevant during the initial stage of the disease. The tumor niche's cell composition is complex and diverse, comprising not only cancer cells, but also OCs, cancer-associated stromal cells and inflammatory immune cells. Once the metastasis is established, all these cell types release algogenic mediators responsible for excitation and sensitization of peripheral nociceptive sensory neurons, thus evoking pain. Protons, bradykinin, endothelins (ET), prostaglandins, proteases, and Trk activators are some of the common algogenic substances released.^{20,32} Nociceptive sensory neurons express different types of receptors to detect different types of noxious stimuli threatening bone homeostasis (Figure I. 10).

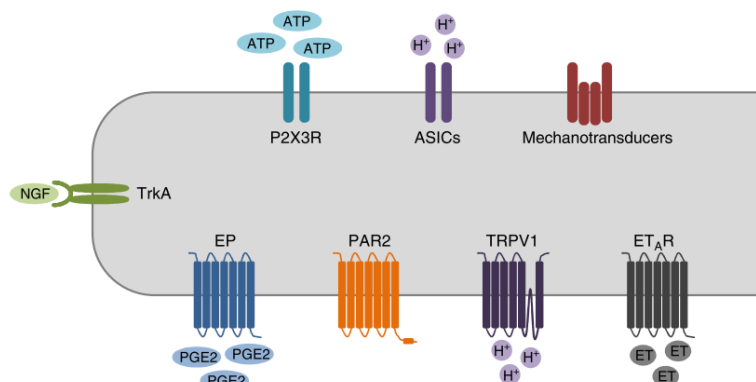


Figure I. 10 - Receptors expressed by bone-innervating nociceptors.²⁹ Nociceptors are responsible for recognizing noxious stimuli of different origin. Several receptors are aimed at detecting chemical algogenic substances. In addition, mechanosensitive ion channels can sense unusual pressure or distortion in the bone. Moreover, nociceptors sensitivity and expression can be boosted by the binding of NGF to its receptor (TrkA). P2X3R = purinergic receptor P2X3; TRPV1 = transient receptor potential channel-vanilloid subfamily member 1; EP = prostaglandin E receptor; ET_AR = endothelin receptor type A.

Acidosis stands out as a major player in CABP, because the tumor niche is characterized by an acidic microenvironment. In one hand, during the process of bone resorption, OCs secrete protons via V-H⁺-ATPase to dissolve the mineral components of the bone. On the other hand, cancer cells release protons and lactate via plasma membrane pH regulators, further aggravating

the acidic extracellular environment created by OCs. Adding to this, the insufficient oxygen delivery to the tumor area creates a hypoxic environment. Cancer cells have a high proliferation rate, which requires an increased ATP consumption. In order to maintain their aggressive profile, the energy metabolism shifts from aerobic respiration to glycolysis (independent of oxygen), which leads to the production of a considerable amount of lactate. Lactate lowers intracellular pH, so to avoid excessive intracellular acidification, cancer cells intensify the release of lactate and protons through plasma membrane pH regulators such as monocarboxylate transport 1 (MCT1) and 4 (MCT4), a phenomenon designated as Warburg effect (**Figure I. 11**).^{20,52,53,64,65}

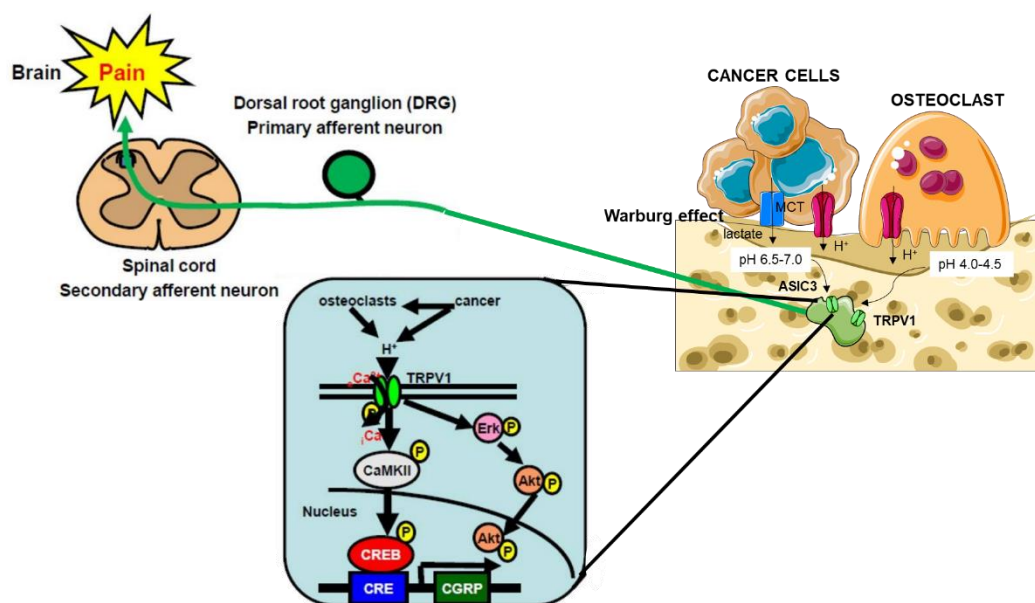


Figure I. 11 - Acidic bone environment and CABP (adapted).²⁰ Both cancer cells and OCs contribute to the creation of an acidic extracellular environment, although OCs have the ability to drop pH even further than the cancer cells (4.0-4.5 versus 6.5-7.0, respectively). The acidic environment activates acid-sensing receptors expressed by the DRG at the end of their axons, ultimately evoking pain in the brain.

The TRPV1 and the acid-sensing ion channel 3 (ASIC3) are two specific and representative pH-sensitive acid-sensing receptors whose expression is increased in DRG in the presence of bone cancer (**Figure I. 11**).^{52,66} TRPV1 expression is nearly all concentrated in the small unmyelinated c-fibers.⁵³ The role of TRPV1 in acid-evoked CABP is supported by the suppression of CABP in preclinical studies where TRPV1 gene was disrupted or TRPV1 antagonists were administered.^{20,59,67,68} TRPV1 is activated when pH is lower than 6.0; when activated, it promotes the influx of calcium ions into cytoplasm, triggering an intracellular signaling cascade which involves Ca²⁺/calmodulin-dependent protein kinase II (CaMKII) and the transcription factor cAMP responsive element-binding protein (CREB). As a result, the transcription of target molecules, such as CGRP, is increased. Additionally, TRPV1 activation also stimulates extracellular-signal-regulated kinase (Erk) and protein kinase B (Akt) pathways to avoid neuron cells' death.²⁰ The role of ASIC3 is not as clear, but its mRNA expression was upregulated in DRG in two models of rat mammary tumor with CABP.^{20,69} Moreover, a single injection of APETx2 (selective ASIC3 antagonist) in a multiple myeloma bone pain mouse model dramatically reduced CABP.⁶⁵ ASIC3 detects moderate extracellular acidification (pH 6.8-7.0).^{20,66}

Given the demonstrated efficacy of TRPV1 antagonists to reduce pain in cancer rodent models, it would be reasonable to propose them as a promising target for pharmacological

intervention in human patients. In fact, this class of molecules was also validated as a promising pain target in rodent models of inflammation or OA, in addition to CABP.⁵⁹ Following such discoveries, several pharmaceutical companies initiated clinical trials with a number of TRPV1 receptor antagonists.⁷⁰ Nevertheless, none has gone past phase II, either on the account of adverse secondary effects, or due to interpatient variability in the response to the drug candidates.^{59,70-72} Hyperthermia was the most prominent side effect and led to the discontinuation of numerous clinical trials with different drugs (AMG517, AZD1386, ABT-102, MK-2295)^{59,70,71}; patients' inability to sense noxious heat stimuli was also reported (ABT-102, MK-2295).⁵⁹ Moreover, a double-blind, randomized clinical trial with fifteen healthy human subjects revealed the inability of BCTC, a TRPV1 antagonist, to inhibit human acidosis-induced pain.⁷² The wide distribution of TRPV1 receptor in the CNS and in non-neuronal cells (epidermal keratinocytes, hepatocytes, granulocytes, pancreatic β -cells, endothelial cells, arteriolar smooth muscle cells, adipocytes), together with the multifaceted dimension of TRPV1 functions (the receptor has the ability to detect several types of stimuli, for example, pH, peptide toxins, lipoxygenase products or heat) might explain the reported side effects and leave open the possibility for other adverse reactions.^{59,70} Regarding the potential of ASIC3 as a target for pain treatment, modulators of ASICs activity have been developed. Nonetheless, pharmacological studies involving these molecules are still at an early stage, therefore data regarding safety and efficacy are insufficient for final conclusions. Additionally, the majority of the modulators developed so far is not specific for ASIC3, targeting other ion channels from the ASICs family.^{66,73} It should be noted that ASIC3 is not exclusively expressed by sensory neurons; it is also present in other tissues, namely, brain, spinal cord, lymph nodes, kidney, heart or testis.⁷⁴ Hence, the administration of ASIC3 antagonists might also raise side effects. Summing up, although TRPV1 and ASIC3 could appear as obvious and correct pharmaceutical targets for pain treatment in the first place, current knowledge concerning their antagonists suggests otherwise.

Acidosis is not the only phenomenon caused by the increased OC-mediated bone resorption triggered by tumor cells. In fact, the shift to an osteolytic profile implies bone destruction, thus mechanical strength and stability are diminished and bone fracture is a possibility. In addition, cancer cells divide, and the tumor mass grows, occupying the space created by bone resorption and further destabilizing bone tissue. Overall, there is a mechanical distortion of the bone tissue that can be detected by the mechanotransducers expressed by the bone innervating sensory nerve fibers, therefore causing pain.^{32,53}

5.2 Neuropathic component of CABP

As tumor cells invade the normal tissue, they initiate nerve injury by destroying the distal processes of sensory fibers, which become fragmented and disjointed. Ongoing and movement-evoked pain are increased after the described nerve injury.³² Following nerve destruction, the opposite process occurs: inappropriate sprouting of bone-innervating sensory and sympathetic fibers and/or neuroma formation is promoted (**Figure I. 12**). The abnormal innervation associated with CABP changes not only the density, but also the morphology and organization of nerve fibers, which assume a more chaotic pattern than in physiological conditions.^{2,32,41,61,75} The increased nerve fiber density leads to hypersensitivity, hence normally innocuous mechanical stress is perceived as noxious and might cause significant pain.² Changes in the innervation were detected in several bone compartments, namely, bone marrow, mineralized bone and periosteum.⁷⁶ Both spontaneous and movement-evoked breakthrough pain have been

associated with electrical impulse conducted by sensory nerve fibers originated by ectopic sprouting.⁷⁷⁻⁷⁹ Considering the two types of observed CABP, breakthrough pain is the most unpredictable and difficult to control. In addition, there is a shift from ongoing to breakthrough pain as the cancer evolves, thus this type of pain is more closely associated with the maintenance of chronic pain.

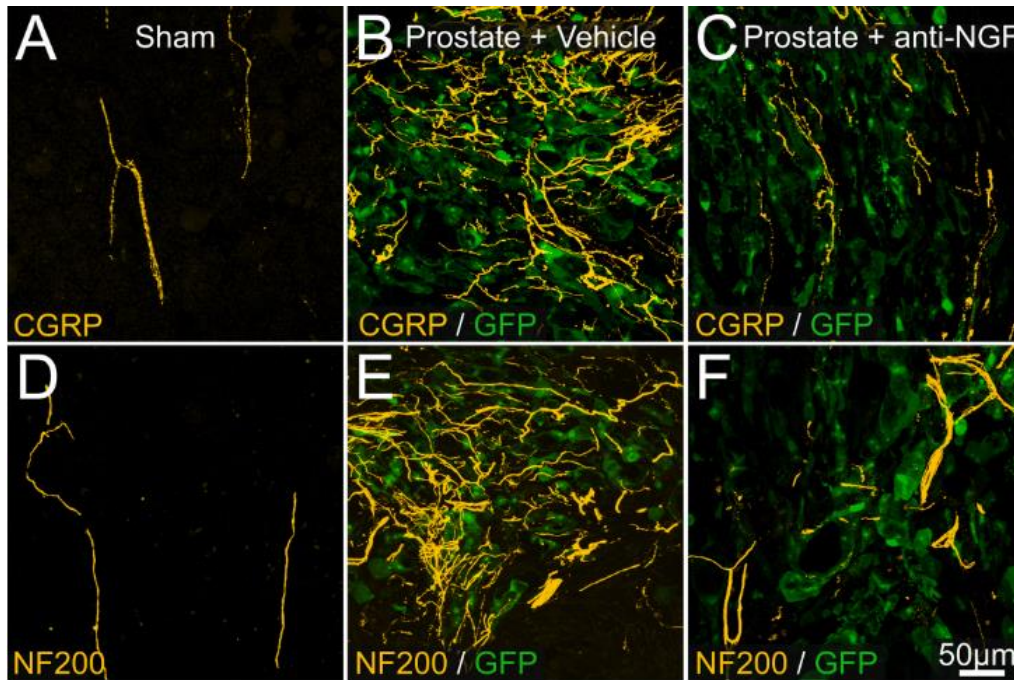


Figure I. 12 - Ectopic nerve sprouting and neuroma formation in a murine model of prostate induced-bone cancer.⁷⁵ The murine model was obtained by injecting canine prostate carcinoma (ACE-1) cells transfected with green fluorescent protein (GFP) into the intramedullary space (B and E). Sham-operated mice were injected with culture medium instead (A and D). Anti-NGF treatment was performed by administering a 10 mg/kg dose of anti-NGF antibody (mAb 911) 10, 15, 20 and 25 days after injection (C and F). Animals were sacrificed 26 days after injection to perform immunohistochemistry. Images were acquired at the metaphyseal region of the bone marrow with a laser confocal microscope.

The abnormal sprouting has been observed in numerous animal models of both prostate and BrCa-derived bone metastasis. In a prostate cancer-induced model obtained by the injection of canine prostate cancers cells into the mouse femur, the number of CGRP⁺/NF200⁺/TrkA⁺ (*Aδ*) nerve fibers per unit area increased 10-70x in comparison with normal bone marrow (**Figure I. 12**).^{44,75} In a different study, ectopic sprouting of periosteal sensory nerve fibers was observed 28 days after injection on the femoral intramedullary space of female athymic nude mice with human BrCa cells (MDA-MB-231-BO – used as a representative of aggressive solid cancer cells). Immunohistochemical analysis revealed expression of CGRP and TrkA on the sprouted periosteal sensory nerve fibers in the vicinity of remodeled cortical bone.⁸⁰ A similar procedure involving the injection of osteolytic murine sarcoma cells (NCTC2472) in male C3H/HeJ mice led to the sprouting of both sensory (NF200⁺ fibers and CGRP⁺ fibers) and sympathetic fibers 20 days post-injection in periosteum. The great majority of these fibers expressed TrkA. These fibers were intermingled amongst themselves, tumor cells and CD68⁺ tumor-associated macrophages and were arranged according to the highly pathological and disorganized pattern of innervation observed in CABP. In addition to sprouting, the identified fibers also resulted in neuroma-like structures (disorganized mass of axons with tangled morphology).³¹ Treatments with anti-NGF

antibody blocked the sprouting (**Figure I. 12**) and diminished bone pain (confirmed by immunohistochemical and behavioral analysis, respectively) in all the three previously described studies (in the later one, early sustained sequestration of NGF had this effect, but late administration only impacted 50% of the animals).^{31,75,80}

These results suggest that NGF plays a role in the pathological sprouting observed in patients with CABP.²⁰ NGF acts by directly activating TrkA-expressing sensory neurons, leading to their sensitization. In addition, this neurotrophin induces the expression of structural molecules (such as neurofilaments and the sodium channel–anchoring molecule p11), transcription factors, neurotransmitters (SP and CGRP) and receptors or channels (bradykinin R, P2X3, TRPV1, ASIC-3, and sodium channels, such as Nav1.8), all required for the regular function of sensory fiber nerves – detecting and signaling noxious stimuli in the bone.^{33,39,44} The impact on TRPV1 involves TrkA-mediated phosphoinositide phospholipase C activation, which leads to the opening of TRPV1 channels.³⁸ Further to this, the profile of supporting cells (such as non-myelinating Schwann cells and macrophages) in the DRG and peripheral nerves was shown to be modulated by NGF.⁴⁴ Despite looking like a promising target for pharmacological intervention, several side effects and other issues have been associated with anti-NGF treatments (e.g. Food and Drug Administration (FDA) suspended all clinical trials with this class of molecules for years). The pros and cons of this therapy will be further explored in the following section. Regarding the source of NGF, studies with animal models of bone cancer pain (breast, prostate and sarcoma) revealed that cancer cells produced little to none NGF. As such, tumor-associated inflammatory, immune and stromal cells (including mast cells, macrophages, neutrophils, T-lymphocytes, endothelial cells and fibroblasts), with a proven ability to produce and release NGF, have been described as the main source of this growth factor. This conclusion is hardly shocking, having in mind that tumor-associated cells account for 10-60% of the tumor mass.^{31,44}

Suppression (or reduction) of CABP after administration of specific inhibitors of osteoclastic activity, such as bisphosphonates (BPs) or denosumab (their effects will be further explored in the following section) was observed in clinical and preclinical trials. Additionally, preclinical data suggest that both BPs and denosumab have direct and indirect antitumor effects, reducing the risk of bone metastases.^{56,81} These results, along with the aforementioned function of OCs in acid-evoked pain, indicate a core role for these cells in the pathophysiology of CABP. Interactions between OCs, cancer cells and sensory neurons have been partially characterized. Nevertheless, information regarding the possible contribution to the modification in the innervation pattern is lacking. In order to understand the possible effect of OCs on axonal outgrowth, our group performed a study using microfluidic platforms that mimic the bone tissue innervation architecture (**Figure I. 13**), reproducing the spatial separation between soma and axonal structures, together with the possibility of exclusive stimulation of the axonal part. The secretome from OCs precursors and mature OCs was used to stimulate explants of embryonic DRG cultures. Interestingly, OC secretome was able to increase axonal outgrowth. None of the neurotrophins expressed in mammals (NGF, BDNF, NT-3 and NT-4/5) was detected in the secretome, either using enzyme-linked immunosorbent assay (ELISA) or liquid chromatography mass spectrometry (LC-MS) analysis. This is in line with the reduced levels of phosphorylated (activated) TrkA and TrkC receptors observed.³⁸ LC-MS analysis of total OC secretome lead to the identification of three possible molecules that can mediate the

interplay between the sensory neurons and OCs: fibronectin, LPR1 and periostin.⁷⁶ All of them have been linked to axonal outgrowth in previous studies.^{82–85} This study provided pertinent information on the effect of OCs on axonal outgrowth under physiological conditions. Nevertheless, further studies are required to understand if the proposed mechanism can be related to the pathological sprouting associated with bone pain and, more precisely, CABP.

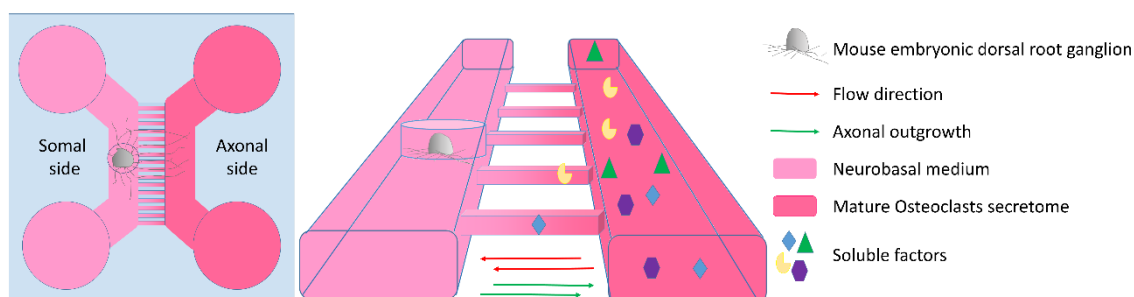


Figure I. 13 - Microfluidic platforms used for the evaluation of axonal outgrowth in mouse embryonic DRG upon stimulation with mature OCs secretome.⁷⁶ Mouse embryonic DRG were seeded on the somal side of the microfluidic platform and cultured in neurobasal medium, while the mature OCs secretome was added to the axonal compartment. Axonal outgrowth was quantified upon 72 h of treatment with the secretome.

OA is another condition that causes skeletal pain and where ectopic sprouting has been observed.^{86–89} In a mechanical model of OA in C57BL/6J (wild type) male mice, obtained by the transection of the anterior cruciate ligaments, a gradually increasing axonal growth and an abnormal distribution of sensory nerve fibers (CGRP⁺, P2X2⁺ and PIEZO2⁺) were detected. These changes were coupled with peripheral neuronal activity in sensory neurons in the DRG. Eight weeks after lesion, the majority of activated neurons was consistent with the size of C and A δ fiber neurons. Furthermore, these changes in innervation correlated with increased osteoclastic activity. The contribution of OCs was confirmed by the inhibition of sensory nerves' growth, DRG neuron hyperexcitability and behavioral measures of pain hypersensitivity in a RANKL knockout mice model. Additionally, the administration of alendronate (a member of BPs class) had similar consequences. OC-induced sensory nerve sprouting appears to be modulated by the secretion of Netrin-1, an axon guidance molecule included in the Netrin family, which acts through the binding to the deleted in colorectal cancer (DCC) receptor expressed by DRG neurons. The activation (by phosphorylation) of focal adhesion kinase (FAK) and phosphoinositide 3-kinase/Akt pathways following the binding to DCC receptor is potentially involved in Netrin-1 action (**Figure I. 14**). This conclusion is supported by different experimental approaches: firstly, Netrin-1 blocking inhibited the axonal growth upon stimulation with OCs CM; secondly, mice models of Netrin-1 and DCC knockouts in TRAP⁺ OCs presented reduced abnormal axonal outgrowth (less density of CGRP⁺ nerve endings), as well as a diminished number of activated DRG neurons and reduced OA pain behavior.⁸⁹

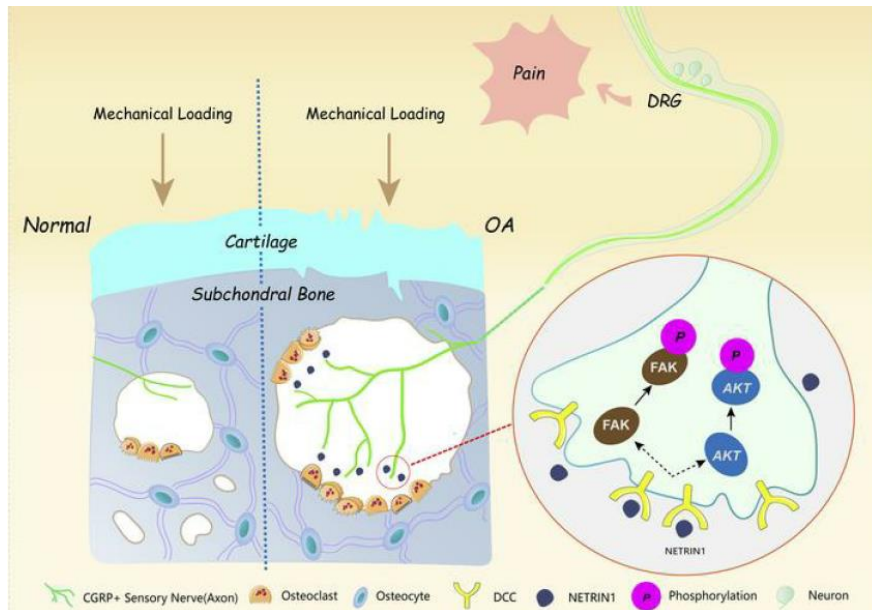


Figure I. 14 - Possible mechanism for the OC-induced sensory nerve sprouting in bone tissue in the context of OA.⁸⁹ OCs secrete Netrin- 1, which binds to the DCC receptor expressed by DRG neurons, activating them and causing pain. Netrin-1 action involves the phosphorylation of FAK and Akt pathways, but a comprehensive understanding of the mechanism is yet to be accomplished.

Taking into account the proposed mechanism in the context of OA, a new category of molecules joins neurotrophins as putative mediators of ectopic sprouting: axon guidance molecules. On the same topic, a study using immunocompromised mice, whose tibial bone marrow cavities were inoculated with osteolytic human prostate (PC-3) or breast (MDA-MB231) cancer cells revealed that the bone/bone marrow stroma transcriptome is modified by cancer cells. Interestingly, molecules of the axon guidance pathway were among the most upregulated pathways in the stroma of osteolytic bone metastasis. Most importantly, comparison with an osteoblastic model (with VCaP cancer cells) suggests the upregulated genes are specific to osteolytic bone marrow/stroma response.⁹⁰ Neurons extend their axons in response to changing environmental cues; the axonal outgrowth involved is controlled and directed by several extracellular receptors and their ligands, a process designated as axon guidance. Semaphorin, ephrin, netrin and slit are the best characterized families of axon guidance molecules.⁹¹ Ephrin ligands (Efn5, Efnb2), ephrin receptors (Epha3, Epha4, Ephb1, Ephb2, Ephb4), ephrin signaling molecules (Ngef, Rsg3), semaphorin ligands (Sema3b, Sema3c, Sema3f, Sema6c, Sema7a), semaphorin receptors (Ntn4, Met, Itgb1, Rnd1) and slit ligands (Slit2, Slit3) were all upregulated in models of osteolytic bone metastasis, but not on the osteoblastic model. Curiously, it has been proposed that semaphorins participate in bone cell communication during bone remodeling. OCs secrete semaphorin 4D (Sema4D) to inhibit bone formation by OBs during bone resorption.^{92–95} On the other hand, mature OCs also express ephrinB2, a membrane-bound molecule from the ephrin family, which binds to OBs and promotes their differentiation.^{14,96} These results suggest the OC-induced ectopic sprouting associated with CABP might be mediated by axon guidance molecules. Therefore, in-depth examination of the mechanisms behind ectopic sprouting should be performed to clarify the pathways underlying this phenomenon.

6. Bone pain treatments

SREs represent a heavy burden in patients with bone metastatic BrCa. Consequently, it does not come as a surprise that several bone targeted therapies have been developed, not only to solve bone pain, but also other common SREs.⁸¹ Focusing on CABP, the available options with established clinical use can be divided into two categories: disease modifying agents and standard analgesics. Anti-NGF treatments are currently being evaluated but are not yet included in medical guidelines for CABP patients.²⁹ As it will become clear, none of them is free of adverse effects, which were reported to be responsible for 10-30% of the cases where cancer patients experience inadequate pain relief.^{52,97}

6.1 Disease modifying agents

BPs and denosumab are classified as antiresorptive agents, because they inhibit the osteoclastic activity (different BPs have distinct modes of action to cause the effect).^{29,81} The chemical structure of BPs, in particular of nitrogen-containing BPs such as zoledronic acid or pamidronate, confers a high affinity to the hydroxyapatite present in the mineralized bone.³ Zoledronic acid, which appears to be a particularly efficient BP and requires a 10-times lower dose than pamidronate,^{81,98} acts by disrupting OCs' cytoskeleton, inducing their apoptosis and resulting in reduced bone resorption.⁸¹ Denosumab is a fully human recombinant monoclonal antibody that targets RANKL, avoiding its interaction with RANK in preosteoclasts (mimicking the action of OPG, the natural decoy of RANKL); as consequence, OCs maturation is avoided and bone resorption reduced.^{50,81,99}

Denosumab and zoledronic acid are approved in Europe for the prevention of SREs in metastatic BrCa, being even included in the European Society for Medical Oncology (ESMO) clinical guidelines for bone health, both at early and advanced cancer stages. Furthermore, zoledronic acid and pamidronate are among the FDA-approved drugs for the treatment of cancer SREs.^{81,100} It is well established through meta-analysis of several clinical trials that BPs and denosumab significantly reduce SREs (e.g. fracture risk, bone loss) and, most importantly, bone pain, increasing the overall quality of life in patients with bone metastases (derived from breast, prostate or lung cancers, as well as multiple myeloma or renal cell carcinoma).^{29,81,99,100} Efficacy studies usually focus on the ability of these compounds to reduce pain; consequently, behavioral tests are the regular procedure and histological analysis is rarely performed. As a result, the impact of BPs and denosumab on ectopic sprouting has not been characterized.¹⁰¹ The administration of alendronate, a member of BPs class, lead to inhibition of sensory nerves growth and DRG hyperexcitability in a OA mouse model.⁸⁹ Therefore, OCs inhibitors might be able to block nerve sprouting. However, further data (preclinical and clinical) must be collected to confirm if this property is shared by other agents. In addition to their bone protective actions, both BPs and denosumab have showed anti-tumor activity in recent preclinical and clinical studies, inhibiting tumor cell proliferation and invasion, thus reducing the risk of bone metastasis and even cancer mortality and recurrence in some cases.^{56,81,100,102,103} Nonetheless, opinions on the ability of BPs and denosumab to have a direct impact on cancer cell proliferation and tumor burden are not consensual, since there are inconsistencies in the studies.

While efficacy in treating CABP is proved, safety is not granted for this class of drugs, because several side effects have been observed during treatment with BPs and denosumab.⁸¹ Acute-phase-like reaction (i.e. systemic pro-inflammatory response triggered by infection,

injury, or immunological disorders which originates symptoms such as fever, nausea, arthralgia and myalgia)¹⁰⁴, renal toxicity (although reversible after drug discontinuation for zoledronic acid and not severe in denosumab, it can be irreversible for patients treated with pamidronate, for instance)^{81,100}, osteonecrosis (i.e. death of bone cells surrounding a joint as a result of an ischemic environment) of the jaw, one of the most common adverse effects,¹⁰⁵ and hypocalcemia (higher risk for denosumab in comparison with zoledronic acid)^{100,106} have been registered. Additionally, RANKL and its receptor are not exclusively involved in osteoclastogenesis and bone homeostasis; mammary physiology and the immune system are amongst the processes involving the RANK-RANKL axis.⁵⁶ Hence, unspecific and undesirable effects might arise from treatment with denosumab.

6.2 Analgesics

Different classes of analgesics are recommended according to pain's severity.¹⁰⁷ Mild to moderate pain is treated with non-steroidal anti-inflammatory drugs (NSAIDs) and acetaminophen (paracetamol), whereas weak opioids (e.g. codeine, hydrocodone, tramadol) are prescribed for moderate pain and strong opioids (e.g. fentanyl, morphine, oxycodone) for severe pain. Although recommended by the World Health Organization, none of these drugs is specific for bone pain, the resulting pain relief is temporary and this medication might have side effects.^{13,29,39,97} Paracetamol is generally regarded as safe, although it increases the risk of chronic liver failure in the case of overdose. NSAIDs, on the other hand, convey a higher risk of gastrointestinal adverse events that range from moderate complications (heartburn, nausea, dyspepsia and abdominal pain) to severe symptoms (e.g. ulcers, bleeding or even perforation). Opioids, which are used to treat more than 80% of oncologic patients¹³, are the gold standard for CABP and are included in European guidelines to control moderate to severe CABP. Nevertheless, they are associated with several side effects, including dry mouth, constipation, nausea and vomiting, vertigo and somnolence. Moreover, misleading opinions from the clinicians and the patients regarding opioid addiction often lead to suboptimal dosages and insufficient pain relief.^{29,97} Additionally, pharmacological studies revealed that drugs from this therapeutic category have a diminished effect in CABP, in comparison with other pain conditions.^{57,108}

6.3 Anti-NGF treatments

Most bone-innervating sensory nerve fibers (80%) express the TrkA receptor, the cognate receptor for NGF. Consequently, sensory fibers are excited/sensitized in the presence of this neurotrophin, whose functions (release of neurotransmitters, increased expression of channels and receptors) are intrinsically involved in pain transmission.^{28,38,44} Blocking NGF action follows as logical approach to treat CABP. Different strategies have been explored for this purpose: sequestering NGF using antibodies, preventing NGF from binding and activating TrkA or inhibiting TrkA function. Anti-NGF antibodies were the most promising methodology in clinical trials. In addition, antibodies usually obtain a faster US FDA approval, on the account of their specificity and diminished off-target effects. Tanezumab, a humanized monoclonal antibody with high affinity and specificity for NGF, prevents its interaction with TrkA receptor, therefore blocking NGF activity.¹⁰⁹⁻¹¹¹ This antibody has efficiently reduced pain in patients with OA and chronic lower back pain, with a safety profile comparable with currently used NSAIDs (valid for lower doses of Tanezumab).^{109,110} Regarding the use as a cancer pain agent, preclinical

data revealed that treatments with anti-NGF blocked not only bone pain, but also the associated ectopic sprouting and neuroma formation in CABP animal models.^{31,75,80} Clinical data are still scarce, but Tanezumab reduced CABP in two different phase 2 trials, as well as in a few phase 3 trials.^{109,111} However, some patients receiving the treatment manifested side effects such as headaches, dizziness, myalgia, peripheral edema, extremity pain, arthralgia and abnormal peripheral nerve sensations (hypoesthesia, paresthesia).^{39,109,110} In fact, FDA suspended all clinical trials with anti-NGF antibodies in 2010, because extensive bone damage and joint destruction were reported; joint replacement was even required in many patients. The suspension was abandoned in the meantime and there are some recent clinical trials being established. Nevertheless, the safety profile of anti-NGF antibodies is far from being consensual.³⁹ NGF has a pivotal role in the differentiation and maintenance of sympathetic and primary sensory neurons. As such, the sequestration of this neurotrophin can generate or aggravate peripheral neuropathies, which is in line with the manifested side effects. It is also important to take into account that eliminating pain completely is undesirable, since it might lead to the inadequate use of damaged bone.¹¹² Moreover, TrkA is not exclusively expressed in bone tissue, therefore tanezumab also interferes with NGF signaling in muscle, skin and other organs.¹¹³ As a consequence, despite promising in the context of CABP, anti-NGF antibodies' long-term efficacy and safety profile must be carefully determined. In addition, the lack of neurotrophins' expression (NGF included) and Trk receptors activation in studies exploring the role of OCs in axonal outgrowth⁷⁶ might suggest there are other relevant targetable pathways to prevent ectopic sprouting and CABP.

Chapter II:

MOTIVATION & OBJECTIVES

Motivation

In 2018, there were 17 million new cancer cases and 9,6 million deaths caused by cancer worldwide. Considering current population ageing and growth, cancer incidence rate is expected to increase 62% until 2030.¹¹⁴ Both cancer itself and its associated treatments can cause significant pain. Bone pain is commonly caused by metastases derived from breast, prostate and lung cancer, which are on the top 5 of the most frequent cancer types worldwide.¹¹⁵ The burden of CABP (both in terms of quality of life and cost) on individuals and health care systems is expected to escalate within the next decades. Given the current lack of an efficient CABP treatment (50% of the cases are not solved, either due to inability to control the pain or adverse side effects)^{29-31,52,57}, a better understanding of the molecular mechanisms underlying CABP would certainly be of much help to develop more effective medication.

Relevant animal models and important information regarding CABP mechanisms arose in recent years.¹⁰⁰ The inappropriate sprouting of bone-innervating sensory and sympathetic fibers observed in several animal models of bone metastases is particularly interesting. As a matter of fact, whereas acid-evoked bone pain is considerably well-characterized, the mechanisms leading to the abnormal bone sprouting are widely unexplored. Given its association with breakthrough pain, the type of CABP most persistent and difficult to control, studying the nerve sprouting in the tumor-bearing bone is of irrefutable importance. Also, sprouting has been observed in other skeletal diseases apart from CABP, such as bone fractures, OA and degenerated vertebral disc.^{41,89} Consequently, studying the pathways that lead to sprouting might result in the discovery of an appropriate drug target for other bone related diseases. The suppression of CABP after administration of specific OCs inhibitors and the recent finding of OC-induced sensory innervation in an OA model suggest that OCs are an important player in bone pain. Hence, characterization of OCs' role in the pathophysiology of CABP represents the motivation for this work.

Objectives

The ultimate goal of the project was understanding the crosstalk between OCs and nerve cells in the context of bone cancer pain. In particular, unravelling the neurotrophic potential of OCs under physiological or malignant conditions, i.e., in the presence of BrCa cells secretome. This pathological scenario was studied in an *in vitro* experimental set up using murine cells.

In order to achieve the aforementioned goal, several specific tasks were defined.

Task 1 comprised the characterization of the morphology, cell number and activity of OCs under malignant stimuli. Mice bone marrow derived OCs were cultured in TCPS plates or upon a mineralized substrate (bone slices) and exposed to the CM of bone tropic BrCa cells (4T1.2 cell line). Upon termination of the stimulus, the OCs CM was collected to be used in the second task. Control conditions where OCs were not under tumorigenic stimulation were also included.

Task 2 corresponded to the evaluation of the neurotrophic potential of OCs under the effect of tumorigenic stimulation or in physiological conditions. Embryonic mice DRG explants were cultured in compartmentalized microfluidic devices according to a previously established protocol¹¹⁶ and their axonal terminals were exposed to the OCs CM earlier collected during Task 1. Axonal elongation was assessed using a neuronal cell marker and subsequently quantified using the semi-automated image analysis software AxoFluidic.¹¹⁶

Task 3 involved the identification of possible molecules responsible for the neurotrophic potential of OCs. Netrin-1 mRNA expression levels were assessed by RT-qPCR, both in OCs under tumorigenic stimulation, and in physiological conditions.

Chapter III:

MATERIALS & METHODS

All animal procedures were approved by the institutional (IBMC/INEB/i3S) ethical committee, together with the Portuguese Agency for Animal Welfare (*Direção-Geral de Alimentação e Veterinária*) and performed in accordance with the European directive (2010/63/EU) and the Portuguese law (DL 113/2013). Bone marrow was extracted from adult C57BL/6 male mice (6-8 weeks-old), maintained at 22 °C under a 12 h light/dark cycle and with *ad libitum* access to water and food. Pregnant females, from the same strain and age, as well as housed in the same conditions, were used to obtain murine embryos. Mice were euthanized by inhalation using carbon dioxide.

Interaction between BrCa cells and OCs: impact on morphology and activity

1. Cell culture

1.1 Bone tropic BrCa cell line

The 4T1.2 cell line was kindly provided by Dr. Robin Anderson, from Olivia Newton-John Cancer Research Institute (Australia). This cell line was originated from BALB/cfC3H mice as described elsewhere.¹¹⁷ Mycoplasma testing based on PCR amplification of mycoplasma 16S rRNA sequences was performed upon cells arrival. The cells were tested after 2 weeks in culture and the results were negative, revealing no contamination.

The 4T1.2 cell line was seeded on T75 cm² flasks and maintained in alpha-minimum essential medium (α -MEM) supplemented with 10% (v/v) fetal bovine serum (FBS) and 1% (v/v) penicillin/streptomycin (P/S) at 37 °C with 5% CO₂. The α -MEM submitted to supplementation was a solution prepared with α -MEM powder (10,17 g/L) and sodium bicarbonate (2,2 g/L), with an adjusted pH of 7,2. This solution was subsequently filtrated with a 0,22 μ m filter under sterile conditions and kept at 4 °C until supplementation and further use. Cells were subcultured at a 1:6 ratio, 3 days after seeding. Upon assessment of morphology and confluency with the optic microscope Olympus CKX41 (Olympus, Japan) at 10x objective (**Figure III. 1**), CM was collected, centrifuged (1600 rotations per minute (rpm), 5 minutes) and stored at -80 °C. Once the media was removed, cells were gently washed with warm phosphate buffered saline (PBS) and the culture medium was replaced by α -MEM supplemented only with 1% (v/v) P/S. The cells were incubated in the FBS free media at 37 °C with 5% CO₂ for 24 h. Once the 24 h period had expired, the CM was processed using the procedure previously described. CM was collected when cells were 80-95% confluent. All steps were performed under sterile conditions in a laminar flow chamber.

Once the FBS free CM was collected, cells were trypsinized and centrifuged (1100 rpm, 7 minutes). Next, the pellet was resuspended in PBS and again centrifuged under the same conditions. Supernatants were removed and cell pellets were ultimately used for gene expression analysis (kept at -80 °C until said analysis).

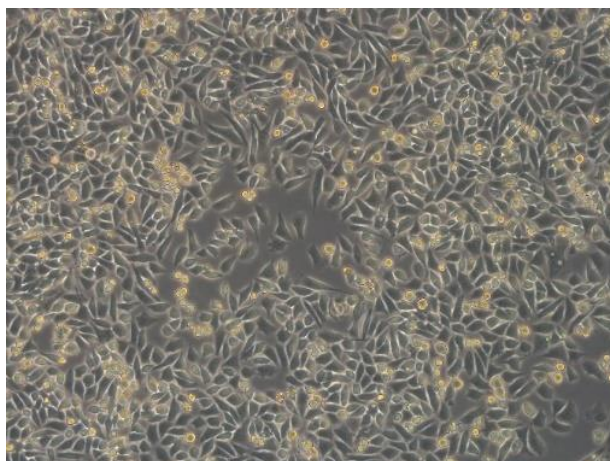


Figure III. 1 - Representative image of the 4T1.2 cell line morphology. 4T1.2 Cells were cultured on T75 cm² flasks and CM was collected once cells were between 80-95% confluent. Acquired with microscope Olympus CKX41 (Olympus, Japan) at 10x objective equipped with AnalySISgetIT 5.1 software (Olympus Soft Imaging Solutions GmbH, Germany).

1.2 Murine OCs

1.2.1 Isolation and differentiation

Tibiae and femurs of adult C57BL/6 male mice (7-8 weeks) were collected and flushed with α -MEM supplemented with 10% (v/v) FBS and 1% (v/v) P/S, to isolate bone marrow cells. After homogenization, filtration (70 μ m cell strainer) and centrifugation (1600 rpm, 5 minutes) at room temperature (RT), the bone marrow cell suspension was incubated with ammonium-chloride-potassium lysing buffer for 1 minute at RT to remove the red blood cells. Subsequently, centrifugation was performed under the same conditions, cells were resuspended in α -MEM supplemented with 10% (v/v) FBS and 1% (v/v) P/S and incubated in the presence of 10 ng/mL M-CSF on 10-cm-diameter culture Petri dishes (3 per animal) for 24 h at 37 °C with 5% CO₂. Once the 24 h-incubation period was completed, the non-adherent cells were collected, centrifuged and resuspended in α -MEM supplemented with 10% (v/v) FBS and 1% (v/v) P/S, with an increased M-CSF concentration (30 ng/mL) and plated once again on 10-cm-diameter culture Petri dishes. Cells were incubated for three days at 37 °C with 5% CO₂ to generate preosteoclasts. A cell-scraper was then used to physically detach the adherent cells, which were subsequently plated in the presence of 30 ng/mL M-CSF and 100 ng/mL RANKL (added to the α -MEM supplemented with 10% (v/v) FBS and 1% (v/v) P/S) at a cellular density of $1,7 \times 10^4$ cells per well ($5,3 \times 10^4$ cells/cm²) to generate mature murine OCs.^{76,118,119} Cells were maintained at 37 °C with 5% CO₂ for 4 days (medium renewed on day 3). The progress of the cell culture was assessed with the optic microscope Olympus CKX41 (Olympus, Japan) at 10x objective. Cells were seeded both in TCPS based 96 well-plates and on top of commercially available cortical bovine bone slices (dimensions: 6 mm diameter/0,4 mm thickness; Boneslices, Jelling, Denmark) to assess OC resorption activity. Bone slices were preserved in ethanol at 4 °C; shortly before use, they were incubated in α -MEM supplemented with 10% (v/v) FBS and 1% (v/v) P/S at 37 °C and later placed in 96-well plates prior to cell seeding.

1.2.2 CM collection

CM from preosteoclasts and OCs was collected on days 0 and 4 of differentiation, respectively. Upon collection, CM was centrifuged (1600 rpm, 5 minutes) and stored at -80 °C.

All steps were performed under sterile conditions in a laminar flow chamber. A schematic description of the protocol can be found in **Figure III. 2**.

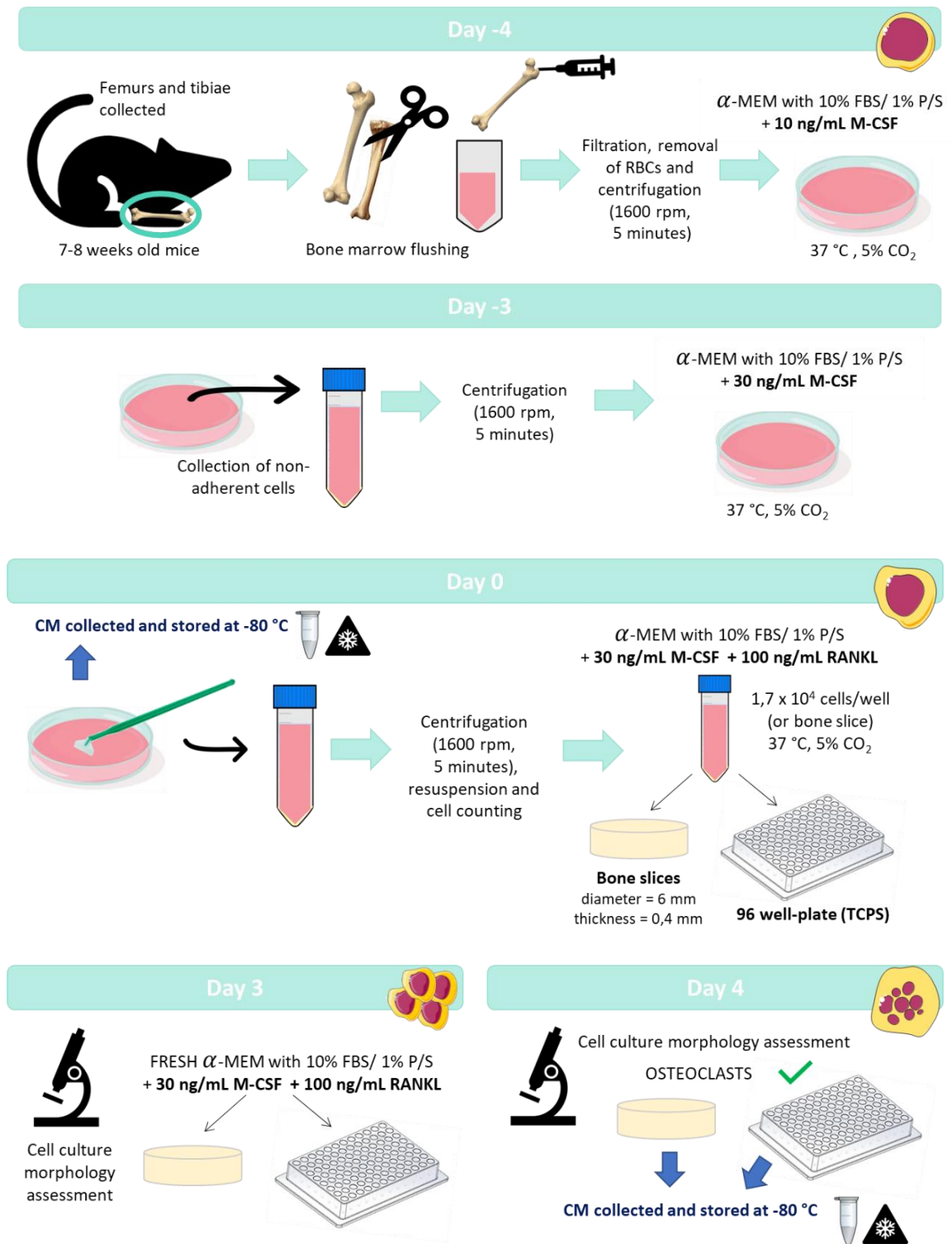


Figure III. 2 - Protocol for isolation and differentiation of murine OCs. Bone marrow cells were collected from femurs and tibiae of 7-8 weeks mice and underwent an 8-day differentiation process to generate mature OCs, either on TCPS well-plates or on bone slices.

1.2.3 Treatment with 4T1.2 CM

Treatment with bone tropic BrCa cells CM (4T1.2 CM) was only initiated upon confirmation of the presence of large, multinucleated OCs (**Figure III. 3**) covering nearly all the surface of each well. OCs were incubated with serum free 4T1.2 CM alone (100%) or in a 1:1 proportion to OC culture media (α -MEM 10% FBS/1% P/S, either supplemented with 30 ng/mL M-CSF and 100 ng/mL RANKL or not) for 6 or 24 h.

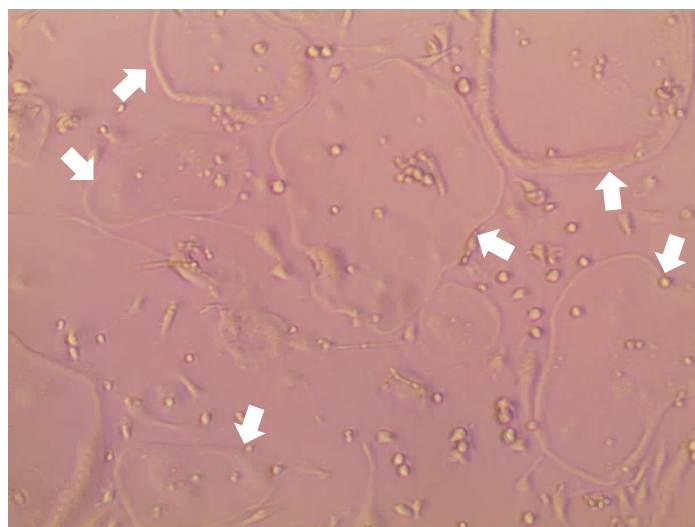


Figure III. 3 - Representative image of mature murine OCs (day 4 of cell culture). Arrows indicate OC-like cells. Image acquired with the optic microscope Olympus CKX41 (Olympus, Japan) at 10x objective, using the AnalySISgetIT 5.1 software (Olympus Soft Imaging Solutions GmbH, Germany).

Three control conditions with no CM were also included (consult **Table III. 1** for a summary of the experimental conditions):

- OC culture media: α -MEM supplemented with 10% FBS, 1% P/S, 30 ng/mL M-CSF and 100 ng/mL RANKL (positive control);
- 4T1.2 culture media: α -MEM medium 1% P/S;
- 50% OC culture media + 50% 4T1.2 culture media: α -MEM medium supplemented with 10% FBS, 1% P/S, 30 ng/mL M-CSF and 100 ng/mL RANKL in a 1:1 proportion with α -MEM medium 1% P/S.

Table III. 1 - Summary of experimental conditions used for the evaluation of the paracrine effect of 4T1.2 cells on OCs. The purpose is concluding about the effect of CM alone or combined with exogenous cytokines.

	Positive control	Control	CM	Control	CM (50%) + cytokines	CM (50%)
4T1.2 CM (%)	0	0	100	0	50	50
M-CSF (ng/mL)	30	0	0	15	15	0
RANKL (ng/mL)	100	0	0	50	50	0
FBS (%)	10	0	0	5	5	5

Additionally, α -MEM supplemented with 10% FBS, 1% P/S and α -MEM alone were also incubated at 37 °C with 5% CO₂, with no cells added. For all conditions, 5 replicates were used for the several assays performed. Once the 6 h or 24 h treatment was completed, the CM of OCs

under tumoral cells' paracrine effect was collected, centrifuged at 1600 rpm for 5 minutes and kept at -80 °C until use. The workflow followed can be found in **Figure III. 4**. All steps were performed under sterile conditions.

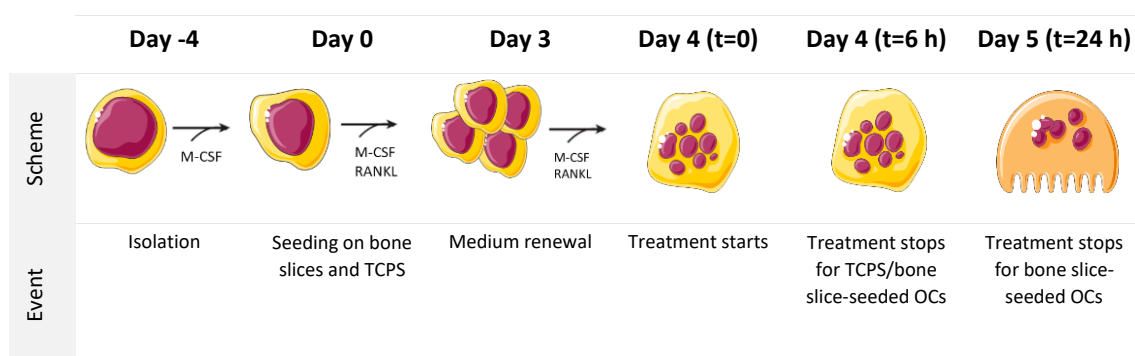


Figure III. 4 - Workflow for OC treatments. After isolation, cells were differentiated by adding M-CSF and RANKL, the key cytokines involved in osteoclastogenesis. The treatment with 4T1.2 CM was initiated on day 4 and it stopped 6 (TCPS and bone slices) or 24 h (bone slices) later. In order to evaluate the cancer cells effect on OCs, both morphology and activity were assessed.

2. OC characterization

The impact of the tumoral cells' paracrine effect on the OCs was evaluated through different techniques. TRAP staining and F-actin immunostaining were used to evaluate cell morphology (OCs seeded on TCPS). On the other hand, toluidine blue staining of resorption cavities (OCs seeded on bone slices) and TRAP activity (both OCs seeded on TCPS and on bone slices) were assessed to understand the impact on OC activity. Additionally, bone slices were stained with calcein acetoxymethyl (AM) to perform a morphometric analysis of bone matrix resorption.

2.1 Cell morphology

2.1.1 F-actin immunostaining

Firstly, cells were fixed with 4% paraformaldehyde (PFA) in PBS. Subsequently, permeabilization was performed by incubation with 0,1% (v/v) ice-cold Triton X-100 in PBS for 5 minutes, followed by a washing step with PBS. Then cells were incubated with a blocking solution composed of 1% (w/v) bovine serum albumin (BSA) in PBS for 30 minutes at 37 °C, to avoid antibody unspecific binding. The following step was the incubation with Flash Phalloidin Green 488 (1:80 in PBS) for 1 h, in the dark, at RT. The fluorescently labeled phalloidin binds cytoskeletal F-actin with high selectivity and photostability. Once completed this incubation period, cells were washed with PBS and nuclei were stained with 4',6'-diamino-2-fenil-indol (DAPI), 1:10 000 (in PBS) for 5 minutes, in the dark. The samples were stored in PBS at 4 °C, protected from the light, until the moment of analysis. For each experimental condition, 5 replicates were performed.

Six representative images from each replicate were captured through the inverted fluorescence microscope Axiovert 200M (Carl Zeiss, Germany) coupled to a camera AxioCam HRc, using the AxioVision SE 64 438 Rel 4.8 software (Carl Zeiss, Germany). Cells with more than 3 nuclei were manually counted as OCs.

2.1.2 TRAP staining

TRAP staining was performed on TCPS seeded-OCs, using the acid phosphatase, leucocyte kit according to the manufacturer's instructions. Cells were fixed with a citrate/acetone solution for 30 seconds at RT, rinsed with deionized water and left to air dry for at least 15 minutes. The subsequent step involved the incubation with previously warmed (to 37 °C) TRAP Solution (containing deionized water, acetate solution, naphthol AS-BI phosphoric acid solution, tartrate solution and fast garnet GBC salt) at 37 °C for 1 h, in the dark. Once the incubation period was completed, cells were washed in deionized water for 3 minutes and then incubated with acid hematoxylin solution for 5 minutes; both steps were performed at RT. Lastly, cells were rinsed in deionized water for 3 minutes (at RT), allowed to air dry and kept at 4 °C (in the dark) until further analysis.

TRAP⁺ cells with more than 3 nuclei were manually counted as OCs. In order to perform such quantification, an image of the whole well was obtained from each replicate using the MosaicX module of the inverted fluorescence microscope Axiovert 200M (Carl Zeiss, Germany), coupled to a camera AxioCam HRC with the AxioVision SE 64 Rel. 4.8 software (Carl Zeiss, Germany).

2.2 Cell activity

2.2.1 TRAP activity

TRAP enzyme activity in OC CM was measured by the conversion of p-nitrophenyl phosphate to p-nitrophenol (yellow compound) in the presence of sodium tartrate. In order to do so, a solution buffer containing 1 M acetate, 0,5% Triton X-100, 1 M sodium chloride, 10 mM ethylenediaminetetraacetic acid (EDTA), 8,8 mg/mL L-ascorbic acid, 46 mg/mL disodium tartrate and 18 mg/mL 4-nitrophenyl was added to OC CM and the mix was incubated for 1 h at 37 °C, in the dark. Afterwards, 0,3 M sodium hydroxide was added to stop the reaction. Optical absorbance was read at 405 nm using Synergy Mx microplate reader (BioTek Instruments, Inc., USA) coupled to a computer equipped with the Gen5 1.09 data analysis software (BioTek Instruments, Inc., USA). TRAP activity was measured against a standard curve of p-nitrophenol and later normalized by time of reaction. All measurements were performed in triplicate.

2.2.2 Toluidine blue resorption assay

Resorption cavities were stained with toluidine blue, allowing a qualitative and quantitative analysis of OC activity. Once the OCs CM was collected, it was replaced by deionized water, in order to help removing cells from the bone matrix. Bone slices were rinsed in deionized water and then cells were scraped off with a cotton stick (one bone slice at a time). Once dried with paper, bone slices were incubated for 15 seconds in toluidine blue solution (containing 0,01 g/mL toluidine blue and 0,01 g/mL sodium borate in miliQ water). The excess of staining solution was dried off with paper and the bone slices were transferred to a 48-well plate. All steps were performed at RT. The resorption activity was quantified by the percentage of total eroded surface (%ES), in accordance to **Equation 1**. The percentage of eroded surface represented by trenches (%trench surface/ES) was also calculated using **Equation 2**. To each experimental condition, 5 replicates were performed.

Equation 1:

$$\%ES = \frac{\text{No. of pits} + \text{no. of trenches}}{\text{No. of grids used to cover the bone slice}}$$

Equation 2:

$$\%trench\ surface/ES = \frac{\text{No. of trenches}}{\%ES}$$

In order to count the number of resorption events (pits and trenches) (**Figure III. 5A**), each bone slice was observed under an optic microscope Olympus BH-2 (Olympus, Japan) with the 10x objective and a 100-point grid (Pyser optics, G50 graticule) placed in the ocular lens (**Figure III. 5B**). Only pits and trenches overlapping with the grid intersections (crossing of vertical and horizontal lines) were counted. The grid was successively shifted across the bone slice until all surface was covered. Quantification was performed as a blinded procedure to avoid bias in the execution. Conditions were revealed afterwards (unblinding) so the results could be analyzed, and conclusions withdrawn.

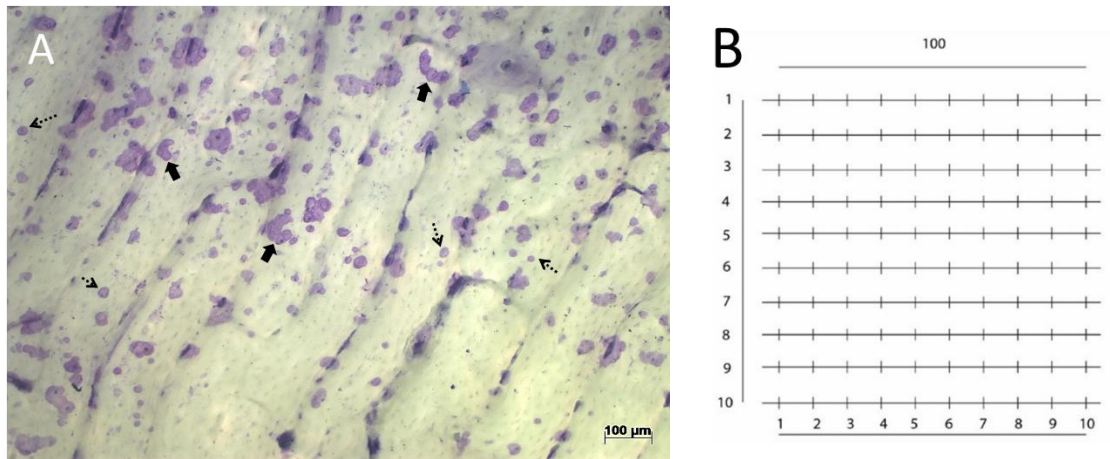


Figure III. 5 - Quantification of bone resorption. **A.** OCs were seeded on top of bovine bone slices and carved the bone matrix, creating two different types of resorption events: deep round/circular shaped pits (dashed arrows) or elongated trenches (solid arrows). Only cavities with a visible depth were considered as resorption events. **B.** A 100-point grid placed on the microscope ocular to count resorption events. Scale bar indicates 100 µm.

2.2.3 Analysis of three-dimensional (3D) resorption pits

Bone slices were rinsed in deionized water, cells were scraped off with a cotton stick (one bone slice at a time) and bone slices were rinsed in deionized water once again. Afterwards, bone slices were washed with PBS twice and then stained with 10 µg/mL calcein AM for 30 minutes, in the dark. Subsequently, they were washed with PBS and allow to air dry. Samples were kept at 4 °C (protected from the light) until further analysis.

Images were acquired with the laser scanning confocal microscope Leica TCS SP5 (Leica Microsystems, Germany), coupled to a computer equipped with the LAS AF software (Leica Microsystems, Germany) at a resolution of 1024 x 1024 pixels with a 40x oil objective. Samples were scanned with a 488 nm laser through a pinhole setting of 1 airy. Images of resorption cavities acquired were averaged twice, and stacked images with a voxel size of 0,3662 × 0,3662 × 0,29 µm were generated. The 3D reconstruction of resorption cavities was achieved using BonePit (available at computools.i3s.up.pt/BonePit/), a program written using MATLAB 2013a

(MathWorks, USA). Stacked images were loaded into the program and the outline of each resorption cavity was manually defined in every stack. A mask containing the defined outlines was created and used to obtain the 3D reconstruction of the resorption event (consult **Figure III. 6** for the protocol).¹¹⁹

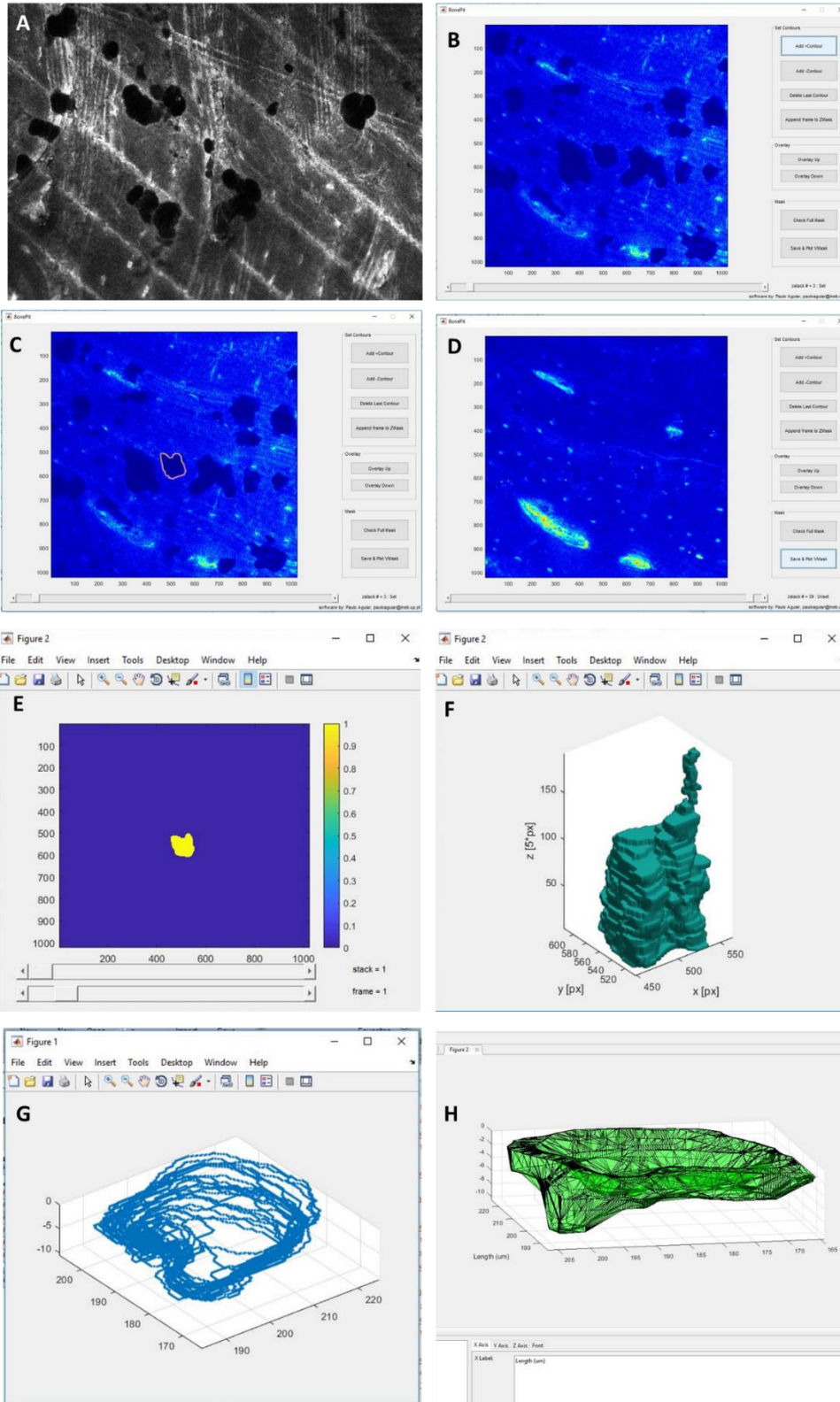


Figure III. 6 - Steps for 3D reconstruction of resorption events using BonePit. **A.** The lif files of calcein-stained bone slices obtained with the software coupled to the confocal microscope were converted to tiff files using ImageJ 1.51j8 (National Institutes of Health, USA); each stack corresponds to a frame in the tiff file. **B.** Tiff files were subsequently loaded into the BonePit software. To make it easier to identify the resorption events, a Gaussian filter is applied by the program – background noise is diminished and a color representation that correlates with pixel intensity is obtained (deeper parts appear in darker shades of blue, while more superficial points are represented in yellow/orange). Once the file is loaded, one can move between z stacks with the slider on the bottom of the panel. **C.** Starting on the z stack where the resorption event begins, the function *Add+ Contour* was used to manually outline its contour. When a satisfactory contour was drawn, it was saved into a mask by pressing the button *Append frame to ZMask* (if a mistake happens, the contour can be removed using *Delete Last Contour* and a new outline can be defined by pressing *Add+ Contour* again). **D.** This procedure was repeated in each stack until the bottom of the resorption event was depicted (which is to say, when the region in darker blue ceased to exist). **E.** To confirm that the right contours were defined in each stack, *Check Full Mask* can be used. A new figure with the outlines drawn in each stack appears. Subsequently, all the contours in each stack were compiled into a mask using *Save & Plot Mask*. **F.** An example of a Mask plot obtained after pressing the aforementioned button. Afterwards, the Mask file previously saved was used as input for the BonePit's function responsible for the volumetric reconstruction and three different outputs are returned: **G.** Figure with the outlines defined in each stack; **H.** Figure with the 3D reconstruction mesh of the resorption event (axes' scale and labels, as well as the mesh color can be edited; the file can be saved into the desired format once the layout is established) and the calculations for volume (μm^3), depth (μm), top section area (μm^2) and aspect ratio (dimensionless).

Evaluation of neurotrophic potential of BrCa and OCs CM

1. Preparation of microfluidic devices

The microfluidic devices used for the DRG cultures corresponded to a molded poly(dimethylsiloxane) (PDMS) chamber sealed by a glass coverslip. The procedure to obtain these chambers (adapted from¹²⁰) involved a set of several steps, starting with the manufacture of the master mold, which is reusable, therefore indefinite PDMS devices can be fabricated by replica molding (**Figure III. 7**). The next step was to clean and then plasma treat PDMS devices and glass coverslips. Once plasma treatment was completed, chambers were assembled and coated with poly-D-lysine (PDL) and laminin.

1.1 Microfluidics fabrication

Mold production was performed at INESC – Microsystems and Nanotechnologies (Portugal). The devices comprised somal and axonal chambers connected by 100 μm high, 1,5 mm wide and 7 mm long channels; somal and axonal chambers were isolated by microgrooves, which assured that only axons could cross the channels and reach the axonal compartment. The master mold was placed in a Petri dish and around 10 g of thoroughly mixed and degassed (around 30 minutes in a vacuum desiccator were required to eliminate all air bubbles) PDMS mixture (10:1 ratio of silicone elastomer base to silicone elastomer curing agent) were poured into the mold (**Figure III. 7B**). If present, any remaining air bubbles or impurities (e.g. hairs) were removed with a needle (**Figure III. 7C**) before incubating the preparation for 2 h at 70 °C in a laboratory oven. Once cured, individual PDMS pieces were carefully cut and separated with a scalpel blade (**Figure III. 7F and G**). The microfluidic chambers were perforated with a 5 mm diameter puncher to obtain the larger reservoirs (**Figure III. 7H**) and with a 3 mm diameter puncher to define the small reservoir (**Figure III. 7I**) for DRG insertion (placed immediately before the microgrooves, without touching them). Any remaining debris or dust was removed using scotch tape (**Figure III. 7J**). Afterwards, under sterile conditions in a laminar flow chamber,

the chambers were rinsed in 70% ethanol (**Figure III. 7K**), left to air dry (**Figure III. 7L**), exposed to ultraviolet (UV) radiation for 15 minutes and stored until further use.

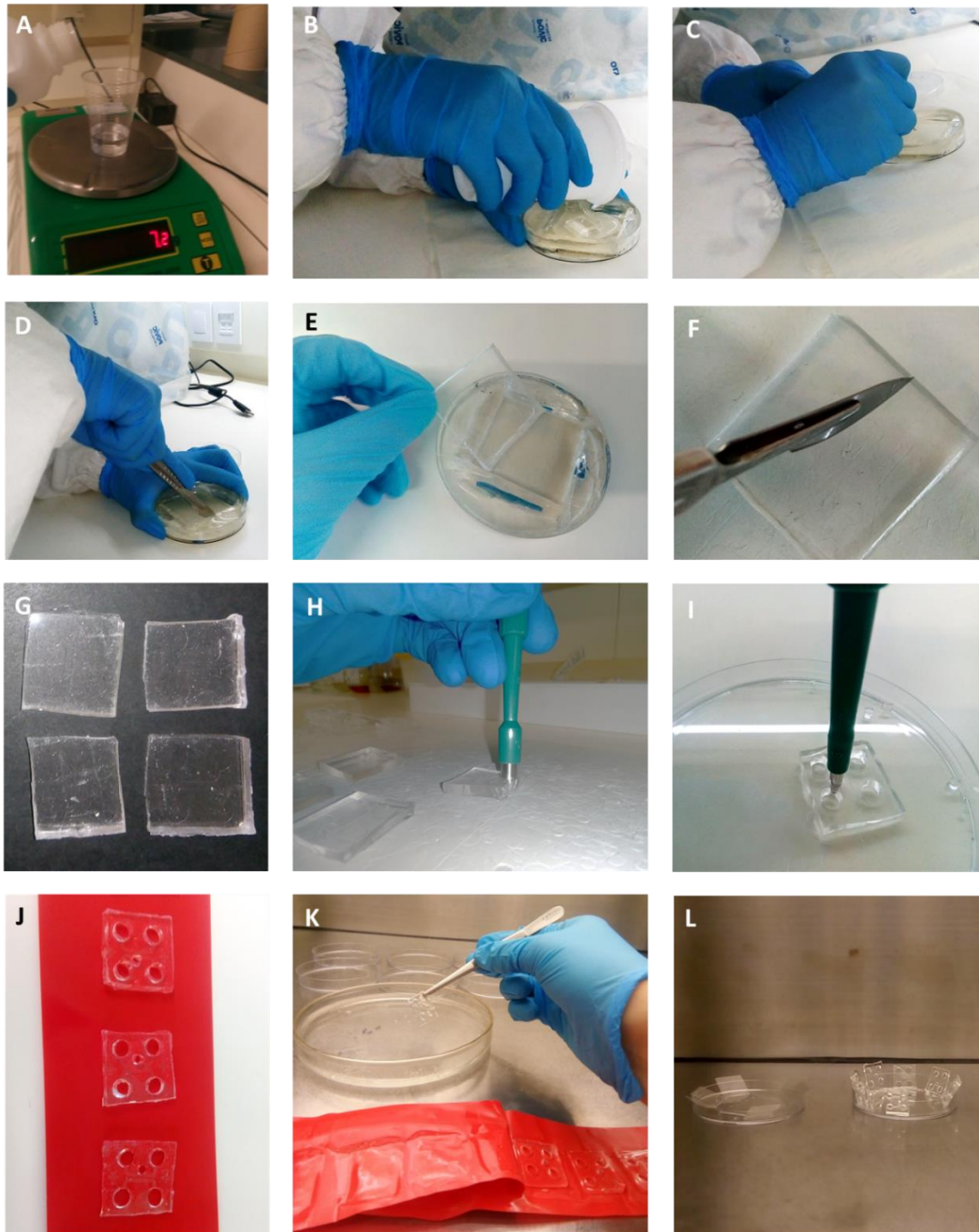


Figure III. 7 - Steps for microfluidic fabrication. **A.** Both the silicone elastomer base and the silicone elastomer curing agent were weighted in an analytical balance using a plastic cup. The mix was subsequently degassed in a desiccator coupled to a vacuum pump and **B.** poured into the Petri dish with the master mold. **C.** Bubbles or impurities were removed using a needle. After 2 h at 70 °C, the Petri dishes were removed from the oven, allowed to cool and **D & E.** the PDMS was cut from the mold with a scalpel blade. **F.** Each mold was cut into **G.** 4 individual pieces. Afterwards, the PDMS structures were perforated with **H.** a 5 mm diameter puncher and then with **I.** a 3 mm diameter puncher to obtain the large and the small reservoirs, respectively. The puncher was placed as vertical as possible to ensure the right structure. **J.** The microfluidic devices were covered with scotch tape to remove any debris or dust. **K.** Under sterile conditions, they were removed from the scotch tape with a clamp and rinsed in 70% ethanol for a few minutes. **L.** Subsequently, they air dried inside the laminar flow hood and were exposed to UV radiation for 15 minutes. Once the 15 minutes period was completed, microfluidics were stored in sterile Petri dishes protected with parafilm until further use.

1.2 Coverslip preparation

Glass coverslips were washed with Alconox 1% during 2 h at 65 °C with continuous stirring and then rinsed thoroughly with deionized water several times. Subsequently, under sterile conditions in a laminar flow chamber, coverslips were rinsed in ethanol 70% for 2-5 minutes, allowed to air dry (**Figure III. 7L**) and exposed to UV radiation for 15 minutes. Coverslips were then stored in sterile petri dishes sealed with parafilm until further use.

1.3 Microfluidics assembling

Both coverslips and PDMS devices (with the microchannel side up) were plasma cleaned with oxygen flux for 30 seconds. Once this processed was completed, the PDMS devices were firmly pressed against the glass coverslip, establishing an irreversible bonding. Assembled devices were coated with PDL by incubation with 0,1 mg/mL PDL solution overnight at 37 °C. Finished the incubation period, the microfluidic devices were washed with autoclaved deionized water three times. Lastly, the microfluidics were coated with a 5 µg/mL laminin solution in neurobasal medium, overnight at 37 °C.

2. Embryonic DRG culture

2.1 Isolation and seeding

Pregnant female mice were euthanized by inhalation using carbon dioxide in order to extract the murine embryos (16-18 days-old), which were maintained on ice-cold Hank's balanced salt solution (HBSS). Spinal cord was removed from the embryos and the DRG were accessed through the dorsal side. Once the DRG was isolated, the meninges and the roots were cut. Isolation was performed under a stereoscopic microscope (SZX10, Olympus, USA). DRG were seeded on the small reservoir of the microfluidic devices. DRG were cultured in neurobasal medium supplemented with 2% (v/v) B-27 Serum-Free Supplement® (B-27), 60 µM 5-fluoro-2'-deoxyuridine (FDU), 25 mM glucose, 1 mM pyruvate, 50 ng/mL NGF, 2 mM Glutamax and 1% P/S. DRG were left undisturbed at 37 °C in 5% CO₂ for 24 h.

2.2 Treatment with 4T1.2 and OCs CM

One day after the seeding, DRG were observed with the optic microscope Olympus CKX41 (Olympus, Japan) at 10x objective to confirm they were in good condition and some neurites had already appeared. The neurobasal medium was then removed only from the axonal compartment and replaced with 4T1.2 CM, as well as CM from either untreated OCs or OCs that were submitted to the paracrine effect of BrCa cells. A positive control with neurobasal medium supplemented with NGF was also included. To assure fluidic isolation, the neurobasal medium was not removed from the somal compartment and, in addition, an equal volume of fresh neurobasal medium supplemented with NGF was added. Thus, the volume on the somal side was superior to the volume on the axonal compartment. A complete description of the experimental conditions used can be found in **Table III. 2**.

Table III. 2 - Experimental conditions used for the evaluation of neurotrophic potential. The conditions were chosen so one could conclude about the neurotrophic potential of the bone tropic BrCa cell line, the untreated OCs and the OCs previously submitted to the paracrine effect of the bone tropic BrCa cell line.

Somal compartment	Axonal compartment
Neurobasal medium + NGF	Neurobasal medium + NGF (positive control) 4T1.2 CM (100%) 50% of 4T1.2 CM + 50% of α -MEM medium 1% P/S TCPS seeded OCs CM maintained for 6 h in: <ul style="list-style-type: none"> • α-MEM medium 10% FBS, 1% P/S, 30 ng/mL M-CSF, 100 ng/mL RANKL • α-MEM medium 5% FBS, 1% P/S, 15 ng/mL M-CSF, 50 ng/mL RANKL (50% OC culture media + 50% 4T1.2 culture media) • α-MEM medium 5% FBS, 1% P/S, 15 ng/mL M-CSF, 50 ng/mL RANKL + 4T1.2 CM (50%) Bone slice seeded OCs CM maintained for 24 h: <ul style="list-style-type: none"> • α-MEM medium 10% FBS, 1% P/S, 30 ng/mL M-CSF, 100 ng/mL RANKL • α-MEM medium 5% FBS, 1% P/S, 15 ng/mL M-CSF, 50 ng/mL RANKL (50% OC culture media + 50% 4T1.2 culture media) • α-MEM medium 5% FBS, 1% P/S, 15 ng/mL M-CSF, 50 ng/mL RANKL + 4T1.2 CM (50%)

The treatment stopped after 72 h of stimulus and axonal outgrowth was evaluated. The experimental set up followed is described in **Figure III. 8**.

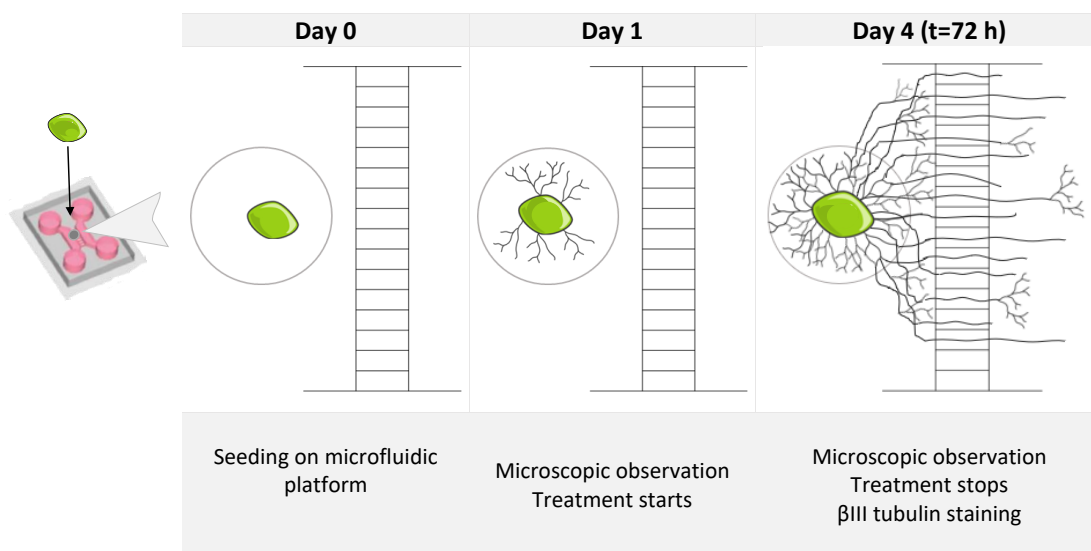


Figure III. 8 - Experimental setup for axonal simulation with CM. DRG were seeded as close to the microgrooves as possible to favor the neurite growth towards the axonal compartment. During treatment, the microfluidic devices were closely monitored to ensure there was enough media on both somal and axonal compartments.

3. Quantification of axonal growth

3.1 β III tubulin immunostaining

Media was removed from the reservoirs; subsequently, DRG samples were fixed with a solution of 2% PFA, 2% sucrose in PBS for 20 minutes, followed by additional 20 minutes of incubation with 4% PFA, 4% sucrose in PBS. Permeabilization and blocking to avoid unspecific binding were performed simultaneously by incubating the DRG with 0,25% (v/v) Triton X-100, 5% (v/v) FBS, 5% (v/v) horse serum in PBS for 30 minutes. All steps described so far were performed at RT. Afterwards, the DRG were incubated with an antibody against the neuronal marker β III tubulin (1:1000 in blocking solution, 5% (v/v) FBS, 5% (v/v) horse serum in PBS), overnight at 4 °C. Following a washing step with PBS, DRG were incubated with the secondary antibody (AlexaFluor 488 anti-Mouse, 1:1000 in PBS) for 1 h at RT, in the dark. Subsequently, DRG were again washed with PBS and nuclei were stained with DAPI (1:10000 in PBS; 5 minutes incubation at RT, in the dark). Lastly, the DAPI solution was removed and the DRG were kept in PBS at 4 °C, protected from the light, until the moment of imaging.

3.2 Imaging and quantification with AxoFluidic software

In order to assess the axonal outgrowth, image acquisition was done using the automated fluorescence widefield microscope IN Cell Analyzer 2000 (GE Healthcare, UK) equipped with IN Cell Investigator software (GE Healthcare, UK). Images were assembled and treated using IN Cell Developer Toolbox 1.9.3 software (GE Healthcare, UK) and ImageJ 1.51j8 software (National Institutes of Health, USA). Subsequently, axonal outgrowth was quantified using a custom-made program previously developed by the group: AxoFluidic (available at www.tinyurl.com/AxoFluidic). The algorithm was written with MATLAB R2010a (MathWorks, USA). As it can be seen in **Figure III. 9**, the segment of interest of each image was loaded into the program and the three domains present in the microfluidic device were defined: the blue line corresponds to the somal side lower border, while the red line defines the axonal side upper border; the space between the two lines corresponds to the microgrooves. Once the limits were established, the profile of each picture was calculated; an exponential fit function that models the fluorescence decay along a longitudinal axis returned two parameters: A , which corresponds to the quantity of axons that reach the axonal side (dimensionless) and λ , which represents the distance the axons reach in the axonal side (in μm).

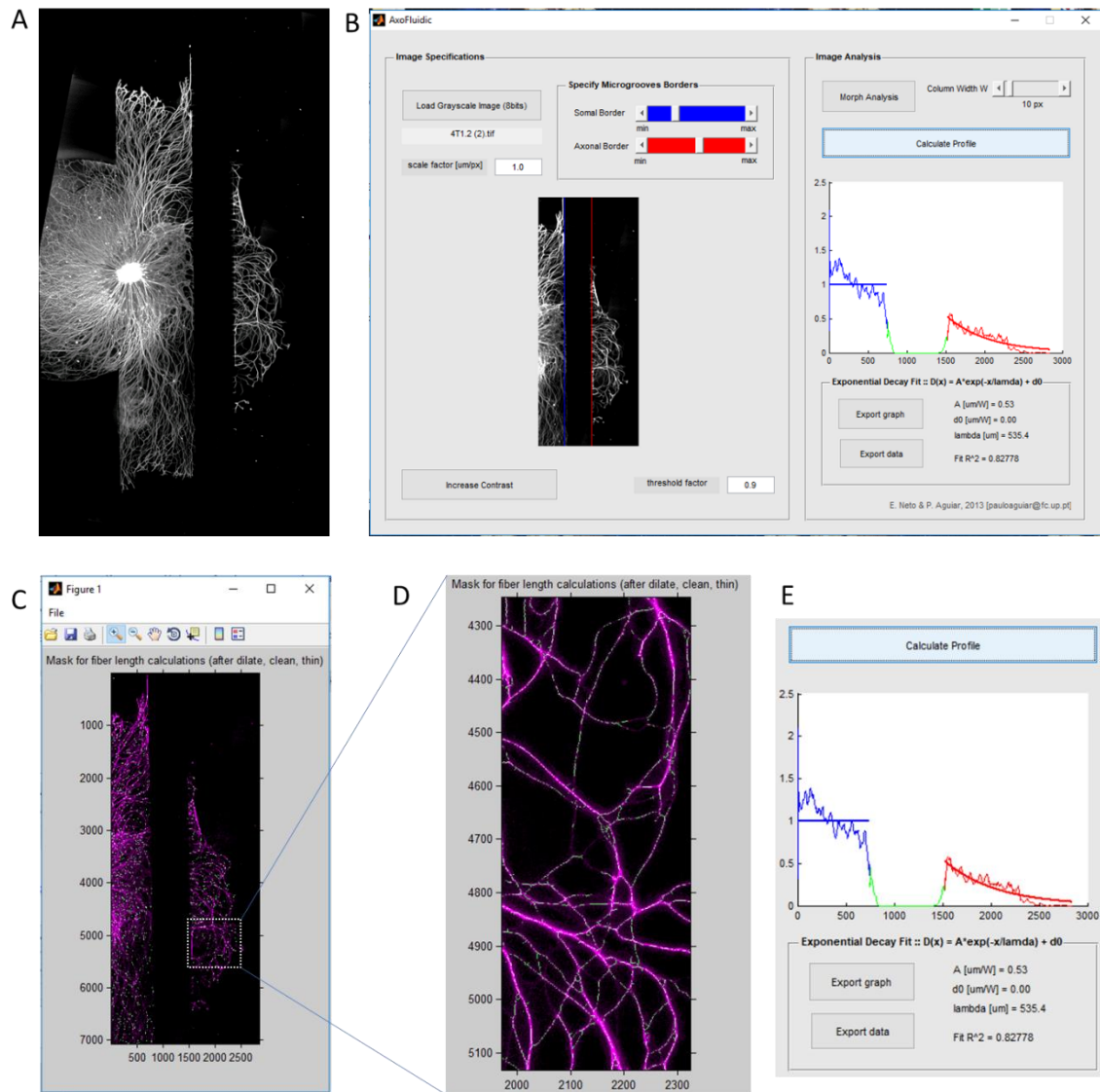


Figure III. 9 - Steps for axonal outgrowth quantification with AxoFluidic. **A.** Example of image obtained after adjusting the brightness and contrast to suitable levels using ImageJ. **B.** Once a good definition of the axons was obtained, the segment of interest was cropped from the full image, saved as an 8-bit Tiff file and subsequently uploaded to the AxoFluidic software. **C.** Preprocessed image to remove background gradients obtained using the function *Morph Analysis*. **D.** Zooming in the preprocessed image, only neurites should appear as green lines. In case there is not enough contrast between the neurites and the background, the *Increase Contrast* function can be used, or the threshold factor can be modified to avoid background noise to be detected as axonal outgrowth. **E.** When the appropriate preprocessed image is generated by *Morph Analysis*, the profile can be calculated (by pressing *Calculate Profile*), and the A and λ values are returned.

Gene and protein expression analysis

1. RNA extraction and quantification

RNA from murine OCs seeded on TCPS (at a cellular density of $5,3 \times 10^4$ cells/cm²) was extracted immediately after culture, once the 6 h treatment stopped, by adding TRIzol reagent to lyse cells. The samples were then stored at -80 °C until further usage. Regarding the 4T1.2 cell line, the cell pellets were stored at -80 °C, thawed at the time of RNA purification and the TRIzol reagent was added. Having all cell lysates properly homogenized in TRIzol reagent, Direct-zol™ RNA MiniPrep kit was used for RNA extraction and purification according to the manufacturer's protocol. Briefly, ethanol 96% was added to the samples (same volume of ethanol and TRIzol)

and vortexed. The mixture was transferred to a Zymo-Spin™ IIIICG Column in a collection tube and centrifuged. Two washing steps followed by centrifugation were performed next. Finally, RNA samples were eluted with RNase free water. All centrifugation steps were performed at 13 000 g for 30 seconds, except for the last washing step before elution, which lasted 2 minutes. RNA final concentration and purity ($OD_{260/280}$) was determined using a NanoDrop 1000 Instrument (NanoDrop Technologies, Thermo Fisher Scientific, USA) coupled to a computer with the NanoDrop 3.0.1 software (Thermo Fisher Scientific, USA). The $OD_{260/280}$ ratio was used to evaluate the presence of pure RNA ($OD_{260/280} \sim 2,0$). Ratios between 2,0-2,2 were accepted as pure RNA, in accordance with the technical specifications provided by the instrument's manufacturer. Additionally, the $OD_{260/230}$ ratio was used as complementary measure of purity: values between 2,0-2,2 were accepted, since lower ratios point to contamination with molecules absorbing at 230 nm, such as phenol (which is present in the TRIzol reagent).

2. Evaluation of RNA integrity

Evaluating RNA integrity is essential to obtain reliable results in gene expression studies, for example involving RT-qPCR. In order to confirm that all samples were intact, the Experion™ automated electrophoresis system (Bio-Rad Laboratories, Inc., USA) was used. The electropherogram of RNA samples is compared to a series of standardized degraded RNA samples and the parameter RQI is returned for each sample. RQI varies between 1 - highly degraded RNA - and 10 - intact RNA. Only samples with $RQI > 7$ were considered for the gene expression studies (consult Appendix to observe the Experion analysis).

3. cDNA synthesis

Once RNA purity and integrity were evaluated, only the samples that satisfied the acceptable range defined for the assessed parameters ($OD_{260/230}$, $OD_{260/280}$, RQI) were used for cDNA synthesis. NZY First-Strand cDNA synthesis kit was used to reverse transcribe the RNA into cDNA according to manufacturer's protocol. RNA from each sample (between 200 or 400 ng) was incubated with the NZYRT 2x Master Mix, NZYRT Enzyme Mix and DEPC-treated water at 25 °C for 10 minutes and then for 30 minutes at 50 °C. The reaction was inactivated by subsequent heating at 85 °C for 5 minutes and posterior chilling on ice for around 10 minutes. With the purpose of removing the remnant RNA, 1 µL of NZY RNase H (*E.coli*) was then added to the mixture, followed by a 20 minute incubation at 37 °C. The cDNA products were stored at -20 °C until required.

4. RT-qPCR

All primers (Invitrogen, USA) were designed using NCBI primer-BLAST.¹²¹ Primers' sequences, as well as the length of the respective amplification product can be found in **Table III. 3**. RT-qPCR experiments were run on the CFX Biorad Instrument (Bio-Rad Laboratories, Inc., USA), making use of the Bio-Rad CFX Maestro 1.0 version 4.0 software (Bio-Rad Laboratories, Inc., USA) for the run setup and for the analysis. The mix used for the RT-qPCR contained 5 µL of iTaq Universal SYBR® Green Supermix, 0,25 µL of each primer (reverse and forward primers at 10 µM), 3,5 µL of nuclease free-water and 1 µL of cDNA product of each sample (or 1 µL of nuclease-free water for the blank). A master mix containing all required components except the cDNA template was prepared on ice and dispensed into the wells of a PCR plate. Triplicates were performed for each sample. The thermal cycling protocol involved a polymerase activation step

of 95 °C for 3 minutes, followed by 40 amplification cycles (denaturation step at 95 °C for 20 seconds; annealing step at 58 °C for 30 seconds and final extension at 72 °C for 20 seconds). Thereafter, the melting curve acquisition started at 55 °C, with a 0,5 °C temperature increment until 95 °C were reached.

Prior to the gene expression analysis for all the samples, different cDNA and primer concentrations were tested in the reaction mix setup. Using 20 ng of cDNA for 4T1.2 cells and 10 ng for murine OCs, together with primers at 10 µM guaranteed the best results. It should be noted that these concentrations are within the recommended range to use with iTaq Universal SYBR® Green Supermix. Furthermore, primers for the target genes and for the reference gene were tested and their efficiencies calculated (see Appendix). To that end, a series of dilutions (1x, 2x, 5x and 10x) was completed. Relative quantification of target gene expression levels was performed using the cycle threshold (C_T) values and calculated according to **Equation 3**. This methodology requires a similar efficiency (approximately 100%) in the amplification of target and reference genes. Mouse glyceraldehyde 3-phosphate dehydrogenase (GAPDH) was used as a reference gene, because it presented appropriate C_T values, as well as a good efficiency and amplification curve, considering the various samples.

Table III. 3 - Pairs of primers used in RT-qPCR analysis. Product length was within the recommended range to use with iTaq Universal SYBR® Green Supermix.

Gene	Forward Primer (5' to 3')	Reverse Primer (5' to 3')	Product length (bp)
GAPDH	GCC TTC CGT GTT CCT ACC	AGA GTG GGA GTT GCT GTT G	183
Netrin 1	GCA AGA CCT GCA ATC AAA CC	GAG GCC TTG CAA TAG GAG TC	199
RANKL	CCC ATC GGG TTC CCA TAAA GT	AGC AAA TGT TGG CGT ACA GG	114

Equation 3:

$$2^{(C_{T \text{ reference gene}} - C_{T \text{ target gene}})}$$

5. Quantification of RANKL in 4T1.2 secretome by ELISA

A commercial sandwich ELISA kit designed to measure mouse RANKL in cell culture supernatants and serum was used to quantify this cytokine in CM from 4T1.2 cells, collected as previously described. The manufacturers' protocol was followed to perform the assay. Briefly, the assay diluent was added to each well, then the CM (sample), the control or standards (a series of dilutions prepared from mouse RANKL included in the kit) were also added to the wells and incubated for 2 h at RT. Subsequently, the contents of each well were removed and replaced by wash buffer. After 5 washes, mouse RANKL conjugate was loaded to the wells and left to incubate at RT for 2 h. Finished the incubation period, the washing step was repeated and the substrate solution (composed of stabilized hydrogen peroxide and tetramethylbenzidine) was added and left to incubate for 30 minutes at RT, protected from light. Finally, the reaction was stopped using diluted hydrochloric acid (stop solution). Lastly, the optical density was read at 450 nm and at 540 nm. Quantification was performed against the standard calibration curve, using the corrected optical density, obtained by subtracting the measurements at 540 nm to the optical density read at 450 nm. Measurements were performed using Synergy Mx microplate reader (BioTek Instruments, Inc., USA) coupled to a computer equipped with the Gen5 1.09 data

analysis software (BioTek Instruments, Inc., USA). All measurements were performed in duplicate.

Statistical analysis

All experiments were repeated two or three times. Data analysis was performed using GraphPad Prism 5.02 for Windows (GraphPad Software, San Diego CA, USA). Statistical differences between groups were calculated using one-way analysis of variance (ANOVA), more precisely, the non-parametric Kruskal-Wallis test followed by Dunns post test for multiple comparisons. The non-parametric Mann-Whitney t-test was used to identify statistical differences when only two groups were being compared. Differences between groups were considered statistically significant when * $0.01 < p < 0.05$, ** $0.001 < p < 0.01$, *** $p < 0.001$.

All the reagents used throughout the different steps of the experimental work can be found in **Table III. 4**, together with the respective supplier and country of origin.

Table III. 4 - List of reagents used for the experimental work. Suppliers and country of origin are displayed.

Reagent	Supplier	Country
4-nitrophenylphosphate disodium salt hexahydrate	EMD Millipore Corporation	USA
4-nitrophenol standard	Sigma-Aldrich	USA
Acetate solution	Sigma-Aldrich	USA
Acid phosphatase, leucocyte kit	Sigma-Aldrich	USA
Ammonium-chloride-potassium lysing buffer	Gibco	USA
Alconox [®] detergent	Sigma-Aldrich	USA
Alexafluor 488 donkey anti-mouse	Invitrogen	USA
Anti- β III Tubulin mouse monoclonal antibody	Promega	USA
B-27	Invitrogen	USA
BSA	VWR Chemicals	Belgium
Calcein AM	Molecular Probes, Life Technologies	USA
DAPI	Sigma-Aldrich	USA
Direct-zol [™] RNA MiniPrep kit	Zymo Research	USA
Disodium tartrate	EMD Millipore Corporation	USA
EDTA	VWR Chemicals	Belgium
FBS	Gibco	USA
FDU	Sigma-Aldrich	USA
Flash Phalloidin Green 488	BioLegend	USA
Glucose	Sigma-Aldrich	USA
GlutaMAX	Gibco	USA
HBSS	Gibco	USA
Horse serum	Invitrogen	USA
iTaq Universal SYBR [®] Green Supermix	Bio-Rad Laboratories, Inc.	USA
L-ascorbic acid	Sigma-Aldrich	USA
Laminin	Sigma-Aldrich	USA
M-CSF	PeptoTech	USA
MEM Alpha medium	Gibco, Thermo Fisher Scientific	USA
Neurobasal medium	Gibco	USA
NGF	Calbiochem, Merck Millipore	Germany
NZY First-Strand cDNA synthesis kit	NZYTech	Portugal
PDL	Sigma-Aldrich	USA
PFA	Calbiochem, Merck Milipore	Germany
P/S	Gibco	USA
Quantikine ELISA (mouse TRANCE/RANKL/TNFSF11 Immunoassay)	R&D systems, Bio-techne	USA
RANKL	PeptoTech	USA
Sylgard 184 silicone elastomer kit (silicone elastomer base + silicone elastomer curing agent)	Dow	Germany
Sodium bicarbonate	Sigma-Aldrich	USA
Sodium borate	Sigma-Aldrich	USA
Sodium chloride	VWR Chemicals	Belgium
Sodium hydroxide	Merck	Germany
Sodium pyruvate	Gibco	USA
Sucrose	Sigma-Aldrich	USA
Toluidine blue	Sigma-Aldrich	USA
Triton X-100	Sigma-Aldrich	USA
TRizol	Ambion, Life Technologies	USA

Chapter IV:

RESULTS & DISCUSSION

General overview

Bone is often colonized by metastases derived from solid tumors. Bone metastases assume particular relevance in BrCa, considering their presence in 75% of patients in the latest stages of the disease.^{47,122} Cancer cells change bone microenvironment, disrupting the equilibrium between bone formation and resorption.⁵³ BrCa is associated with osteolytic metastasis, which implies increased bone resorption or blocking of bone formation. Factors released by cancer cells can directly or indirectly stimulate OCs activity.^{47,122}

The *in vitro* experimental set up followed to understand the crosstalk between OCs and nerve cells in the context of CABP intended to replicate the timeline observed *in vivo* throughout the evolution of bone metastasis. As such, on the first part, the impact of cancer cells CM in OCs was evaluated. This corresponds to the initial interaction that results in a disrupted and permissive bone microenvironment, which later allows the colonization by cancer cells and the establishment of metastases. For the majority of patients (75-90%), the formation of bone metastases is accompanied by CABP, a condition associated with the disruption of bone innervation, manifested by the inappropriate sprouting of sensory fibers.^{32,57} Accordingly, the neurotrophic potential of BrCa and OCs was assessed on the second part, by applying the secretome of BrCa cells and OCs to the axonal terminals of DRG. Primary cultures of both OCs and nerve cells were preferred, since they are more physiologically relevant than cell lines, given the closer representation of the signaling pathways observed *in vivo*. For the same reason, all cells (OCs, DRG and cancer cells) were of murine origin, to ensure the system was recapitulating pathways from a specific species.

In this work, the CM of BrCa and OCs was collected for the purpose of OCs and DRG stimulation. The CM or cell secretome corresponds to the ensemble of proteins released by cells into the extracellular space at a specific moment or under specific circumstances. Secreted proteins represent a class of molecules of paramount importance, because they are involved in vital processes such as cell migration, signaling or communication, playing a central part in both physiological and pathological mechanisms.^{123,124} For all above reasons, the use of CM is a convenient strategy to understand the crosstalk between BrCa, OCs and nerve cells in the context of bone metastases.

Interaction between BrCa cells and OCs: impact on morphology and activity

The 4T1.2 cell line was chosen to represent the BrCa cells. It was derived from the parental 4T1 cell line, previously isolated from a spontaneous carcinoma in BALB/cfC3H mice, by single cell cloning. What is particularly interesting about this cell line is the fact that its bone tropic phenotype was confirmed not only through the presence of bone metastases following the intra-cardiac inoculation of 4T1.2 cells, but also in a natural model of mammary metastases. For the latter, 4T1.2 cells were injected into the mammary fat pad in female BALB/c mice (7-8 weeks).¹¹⁷

Mature OCs are defined as large, multinucleated cells, characterized by the expression of osteoclastic specific markers, such as TRAP, cathepsin K or MMP-9, which are all involved in matrix degradation. Nevertheless, TRAP staining stands out, as it has long been used as a trustworthy technique to identify the unique OC morphology; additionally, it consistently reflects the number of terminally differentiated OCs.^{17,23,125,126} F-actin staining with fluorescent labeled phalloidin was used as an additional technique to evaluate the number and morphology of OCs. The formation of resorption cavities on a mineralized surface is the gold standard to determine osteoclastic activity.^{21,127,128} Therefore, toluidine blue staining was used to characterize cell activity of OCs seeded on bovine bone slices, together with the quantification of TRAP activity, which was also performed for the TCPS seeded OCs.

4T1.2 CM supplemented with exogenous cytokines maintained osteoclastic morphology but did not increase the number of TRAP⁺ cells/OCs

In order to evaluate the effect of BrCa cells on OCs morphology, OCs were seeded on TCPS well plates at a density of $5,3 \times 10^4$ cells/cm², cultured until complete differentiation (day 4) and then treated with 4T1.2 CM for 6 h. Once this period was complete, TRAP or F-actin staining were performed. Different treatment regimens were evaluated: cells were incubated with 100% of 4T1.2 CM or 4T1.2 CM in a 1:1 proportion with OCs culture media (α -MEM with 10% FBS), either supplemented with cytokines (RANKL and M-CSF) or not (in another words, 50% 4T1.2 CM). A different animal (donor) was considered for each independent experiment. When working with CM is rather important to carefully acknowledge the appropriate controls. OCs maintained in α -MEM supplemented with 10% FBS, 30 ng/mL M-CSF and 100 ng/mL RANKL, the ideal differentiation media, were thereby used as positive control. One must exclude the possible influence of the 4T1.2 basal media (without 4T1.2 secretome), so OCs maintained in α -MEM medium were used both as a negative control for the overall experience and as control for the treatment with 100% 4T1.2 CM. For the treatment regimen with 50% 4T1.2 CM, the respective control contained the same concentration of cytokines and serum (5% FBS, 15 ng/mL M-CSF and 50 ng/mL RANKL), lacking only BrCa cells secretome. It should be noted that this condition also worked as the control for the treatment without exogenous cytokines.

TRAP staining showed that the 4T1.2 CM by itself was unable to maintain the osteoclastic phenotype (**Figure IV. 1C and F**). Although the overall cell culture appearance was not as impaired as in the negative control (cells incubated in α -MEM without any serum or cytokines), where nearly no cells remained (**Figure IV. 1B**), very few multinucleated cells were visible when OCs were incubated with 100% 4T1.2 CM or diluted 4T1.2 CM (**Figure IV. 1F**). Furthermore, the remaining multinucleated cells were smaller. On the other hand, when

exogenous RANKL and M-CSF were provided in combination with BrCa cells secretome (50%), larger multinucleated TRAP⁺ cells were more abundant (**Figure IV. 1E**). For this condition, cell culture appearance resembled its control (**Figure IV. 1D**). Nonetheless, the positive control was the condition that resulted in larger and more profuse TRAP⁺ cells (**Figure IV. 1A**).

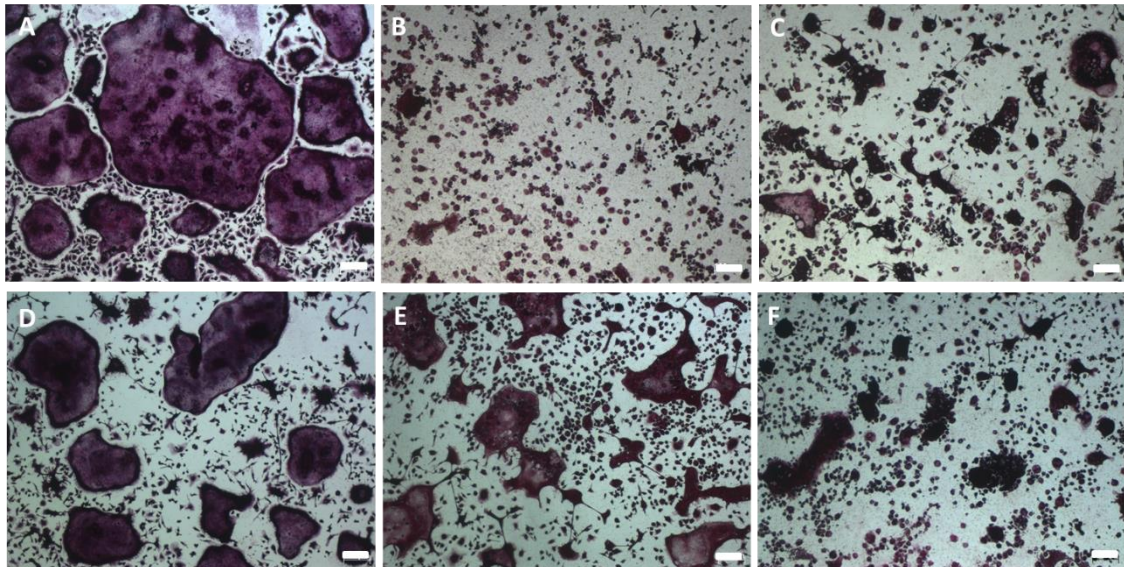


Figure IV. 1 - Representative images of OC morphology in each condition after TRAP staining (Day 4). OCs cultured in **A.** α -MEM supplemented with 10% FBS, 30 ng/mL M-CSF and 100 ng/mL RANKL (positive control). **B.** α -MEM medium (negative control) **C.** 100% 4T1.2 CM. **D.** α -MEM medium supplemented with 10% FBS, 30 ng/mL M-CSF and 100 ng/mL RANKL in a 1:1 proportion with α -MEM medium (control for conditions depicted in E and F) **E.** α -MEM medium supplemented with 10% FBS, 30 ng/mL M-CSF and 100 ng/mL RANKL in a 1:1 proportion with 4T1.2 CM . **F.** α -MEM medium supplemented with 10% FBS in a 1:1 proportion with 4T1.2 CM. Scale bar indicates 100 μ m.

Analyzing the images of F-actin immunostained samples, it was possible to make a clear distinction between the three different types of characteristic actin structures (**Figure IV. 2**) and identify the distinctive OC morphology. Large, multinucleated cells, with fine delineated podosomes (**Figure IV. 2A**, white arrows), actin rings (**Figure IV. 2B**, white arrows) and filopodia (**Figure IV. 2C**, white arrows) were observable.

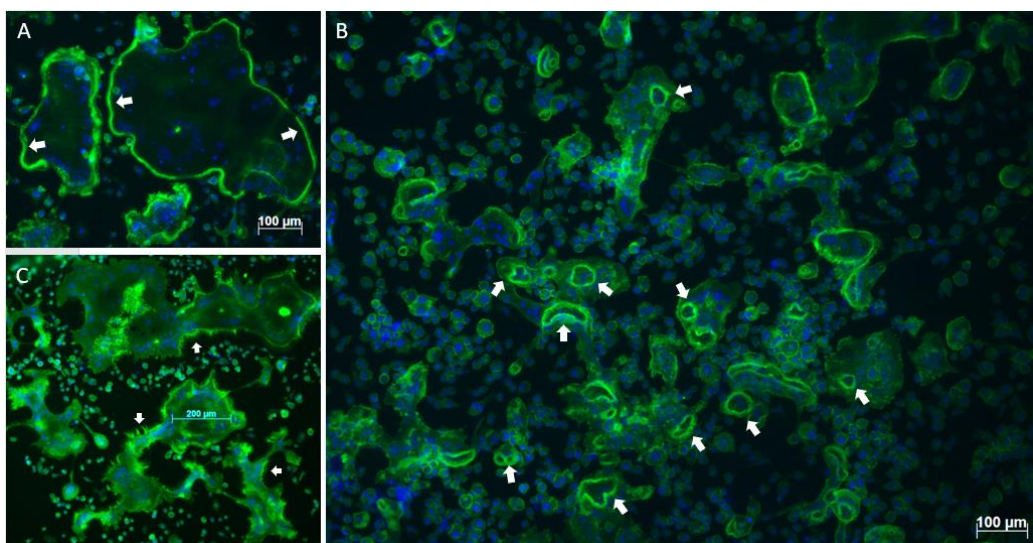


Figure IV. 2 - Representative images of characteristic actin structures found in OCs. Fully polarized OCs with rearranged cytoskeleton were observed in culture. Arrows indicate **A.** podosomes, **B.** actin rings or **C.** filopodia. Nuclei were stained with DAPI (blue), while F-actin staining appears in green. Scale bar is indicated in the images.

F-actin staining further confirmed the previous results obtained with TRAP staining. Indeed, few multinucleated cells were present when OCs were exposed to 100% (Figure IV. 3C) or 50% 4T1.2 CM without cytokines (Figure IV. 3F). In addition, the characteristic actin structures were deteriorated; actin rings and filopodia were still visible in some cells, but less defined. The addition of cytokines to the 50% 4T1.2 CM guaranteed the maintenance of the osteoclastic morphology: large, multinucleated cells, with well-defined podosomes, actin rings and filopodia were visible (Figure IV. 3E). Cell culture appearance was again very similar to the respective control (Figure IV. 3D). Nonetheless, OCs were usually smaller than in ideal physiological conditions (Figure IV. 3E versus Figure IV. 3A).

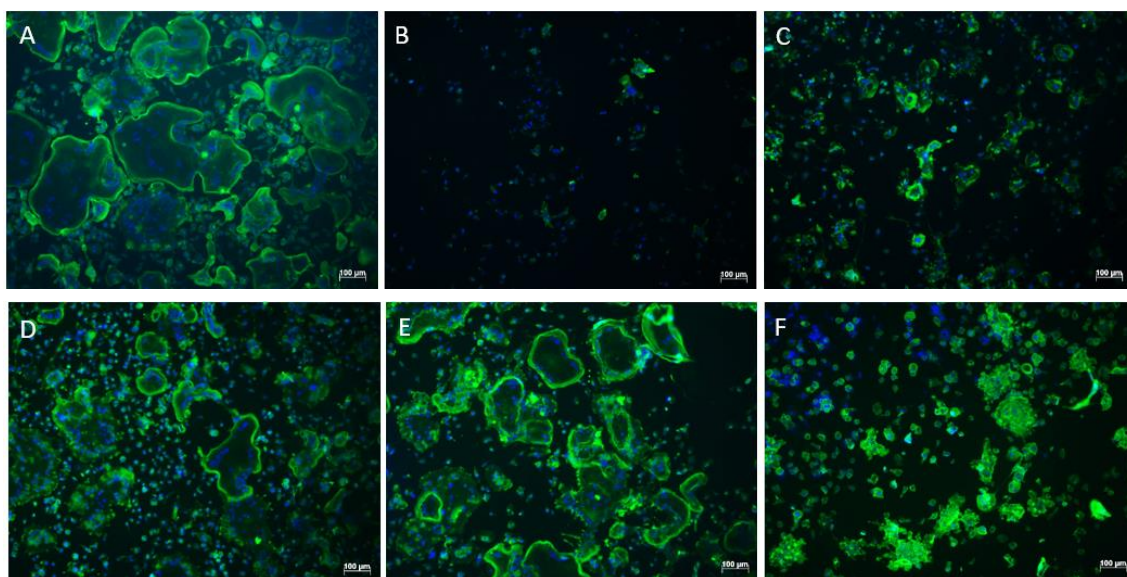


Figure IV. 3 - Representative images of OC morphology in each condition after F-actin immunostaining (Day 4). OCs cultured in A. α -MEM supplemented with 10% FBS, 30 ng/mL M-CSF and 100 ng/mL RANKL (positive control). B. α -MEM medium (negative control) C. 100% 4T1.2 CM. D. α -MEM medium supplemented with 10% FBS, 30 ng/mL M-CSF and 100 ng/mL RANKL in a 1:1 proportion with α -MEM medium (control for conditions depicted in E and F) E. α -MEM medium supplemented with 10% FBS, 30 ng/mL M-CSF and 100 ng/mL RANKL in a 1:1 proportion with 4T1.2 CM. F. α -MEM medium supplemented with 10% FBS, in a 1:1 proportion with 4T1.2 CM. Nuclei were stained with DAPI (blue), while F-actin staining appears in green. Scale bar indicates 100 μ m.

The qualitative TRAP staining analysis was confirmed by the quantitative results. The highest number of TRAP⁺ cells was achieved for the positive control, while the negative control presented a residual number of positive stained cells (Figure IV. 4A). The number of TRAP stained OCs treated with 100% 4T1.2 CM was higher in comparison with its negative control, although this difference did not achieve statistical significance (Figure IV. 4A). Treatment with 4T1.2 CM in a 1:1 proportion with OCs culture media supplemented with cytokines (RANKL and M-CSF) showed a number of TRAP⁺ cells similar to its control and no different from the overall positive control. Together, the results displayed so far led to the conclusion that, in the absence of exogenous cytokines, 4T1.2 secretome by itself was incapable of maintaining the osteoclastic phenotype or number. Nevertheless, when cytokines were added, the number of TRAP⁺ cells remain not statistically different from the positive control.

The same tendency was observed with the F-actin staining, except the number of OCs per well between the treatment (100% 4T1.2 CM) and the negative control was significantly higher (Figure IV. 4B). Again, the combination of cancer cells secretome with exogenous cytokines led to comparable results to the respective control and to the positive control. The

exact same tendency was observed in terms of cell number either using TRAP or F-actin staining (Figure IV. 4) for all conditions, thus the results were consistent.

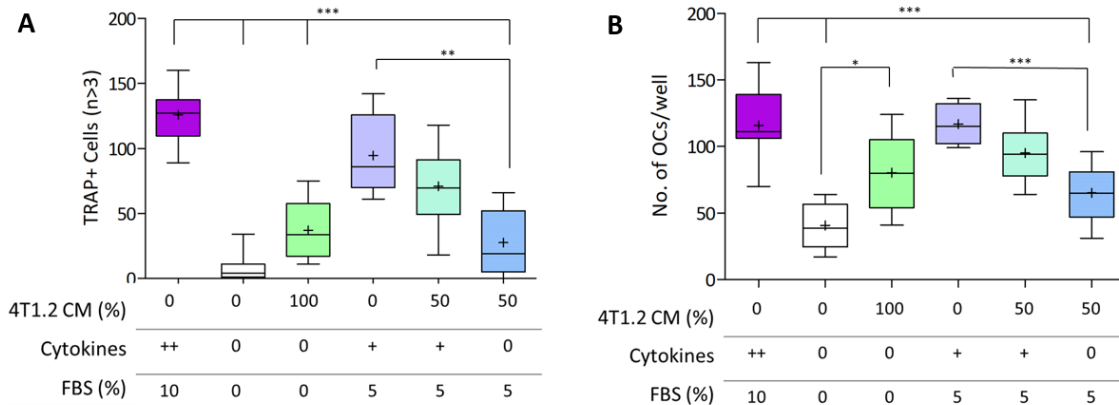


Figure IV. 4 - Evaluation of cell number after treatment with 4T1.2 CM. A. Quantitative analysis of TRAP⁺ stained cells with more than 3 nuclei. **B.** Number of cells with more than 3 nuclei. Regarding the symbols used in the descriptive tables below each condition: ++ = 30 ng/mL M-CSF and 100 ng/mL RANKL, + = 15 ng/mL M-CSF and 50 ng/mL RANKL. Data represented as box & whiskers plots (box from the first quartile to the third quartile, line represents the median, + corresponds to the mean and whiskers represent minimum to maximum range); n=3 independent experiments, 5 technical replicates per experiment. Statistical analysis was performed using one-way ANOVA (Kruskal-Wallis test) and Dunns' post test for multiple comparisons (* 0.01 < p < 0.05, ** 0.001 < p < 0.01, *** p < 0.001).

Starting the treatment at a late stage of differentiation (day 4) was a decision driven by the goal of understanding the impact of BrCa cells in fully mature OCs, which started to be visible in culture around this time. Regarding the timepoint chosen for stopping the stimulus, other treatment durations (24, 48 and 72 h) were also tested, but proved too long, because very few cells were observed in any condition by the end of the treatment, even in the positive control (data not shown). The life span of murine OCs is estimated to be approximately 3 days, when in physiological conditions, in the normal bone.¹²⁹ The bone niche corresponds to a highly complex network of different cell types (OCs, OBs, osteocytes, HSCs, MSCs, nerve cells, etc.) and growth factors/cytokines. The system used for OCs culture was a simplified version of such environment, not mimicking all the stimuli that OCs would normally be exposed to. Hence, the decreased life span of OCs.

It is relevant to perform a critical examination of the treatment regimens considered, along with their respective controls. CM is frequently used in combination with fresh media, since some waste metabolites derived from the incubation with the cells are present. Consequently, a treatment regimen using 100% CM might not be ideal to support cell survival. The ideal proportion between CM and fresh media depends on the provenience of CM, as well as on the cells that are exposed to it. In the present work, 100% 4T1.2 CM proved too aggressive to OCs, as it was demonstrated by the results in terms of cell number and morphology, whereas 50% 4T1.2 CM ensured better outcomes. Over and above, the regimen where OCs are simultaneously exposed to their own culture media and cancer cells CM is more physiologically relevant. In fact, in an *in vivo* scenario, the factors secreted by cancer cells are mingled with other growth factors and cytokines present in the bone niche. In addition, it is known that cancer cells influence differentiation and activity of OCs both directly and indirectly in the context of bone metastases. The indirect interplay often involves OBs (and other stromal cells), since the

BMFs released by cancer cells increase their RANKL production and reduce the release of OPG. Accordingly, the treatment regimen composed by a combination of cancer cells CM and OCs culture media, supplemented with key cytokines for osteoclastogenesis simulates a possible indirect mechanism for cancer cells effect in OCs, with the exogenous cytokines representing the contribution of OBs and other stromal cells. Since the suitable conditions were included in the experiment, we could reliably conclude that the 4T1.2 cells appear to interfere indirectly with OC morphology and number.

4T1.2 CM did not increase osteoclastic activity, trench-resorption mode was predominant

To assess the influence of BrCa cells on the osteoclastic resorption activity, cells were seeded on top of bone slices, using the same cell density as for the assessment of morphology. Treatments with 4T1.2 CM started on the same stage of differentiation (day 4), lasted 6 h and the same conditions were tested. Toluidine blue staining is an easy and fast procedure that enabled the visualization and analysis of resorption events, once cells were removed. The %ES was calculated for each condition, considering both pits and trenches.

Few resorption events were present regardless the condition, still in the positive control more pits and trenches were visible on the bone slices (**Figure IV. 5A**). In contrast, virtually no resorption event was detected when OCs were incubated with α -MEM without FBS or cytokines (**Figure IV. 5B**). Conditions where OCs were exposed to 4T1.2 CM (either 100% or 50%, with or without cytokines for the latter concentration) were a midterm between the two previous controls. However, qualitatively, it was not possible to distinguish them (**Figure IV. 5C, E and F**). In addition, there was no clear difference between the treatments with 50% 4T1.2 CM (**Figure IV. 5E and F**) and their respective control (**Figure IV. 5D**), as resorption events were overall rare.

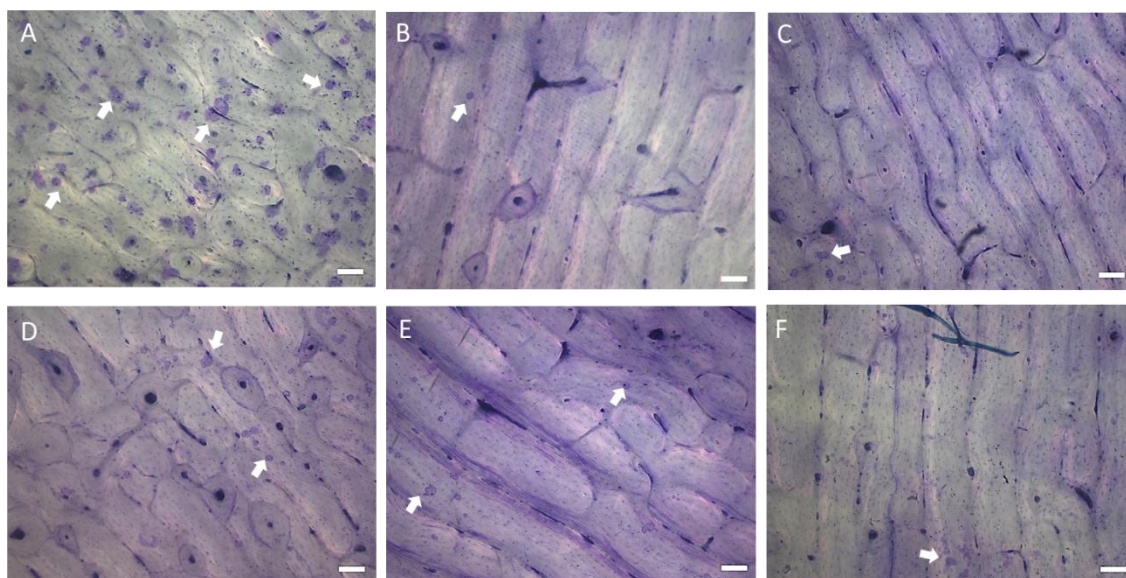


Figure IV. 5 - Representative images of toluidine blue stained bone slices for each condition (Day 4, 6 h of stimulus). OCs cultured in **A.** α -MEM supplemented with 10% FBS, 30 ng/mL M-CSF and 100 ng/mL RANKL (positive control). **B.** α -MEM medium 0% FBS (negative control) **C.** 100% 4T1.2 CM. **D.** α -MEM medium supplemented with 10% FBS, 30 ng/mL M-CSF and 100 ng/mL RANKL in a 1:1 proportion with α -MEM medium 0%FBS (control for conditions depicted in E and F) **E.** α -MEM medium supplemented with 10% FBS, 30 ng/mL M-CSF and 100 ng/mL RANKL in a 1:1 proportion with 4T1.2 CM. **F.** α -MEM medium supplemented with 10% FBS in a 1:1 proportion with 4T1.2 CM media. Arrows correspond to examples of resorption events. Scale bar indicates 100 μ m.

Looking to the quantitative data, when OCs were submitted to a 6 h treatment, bone resorption was generally low (%ES < 2%, considering either the mean value or the third quartile for each condition) and no significant differences were detected between conditions, confirming previous conclusions. The only exception was the treatment with 4T1.2 CM in a 1:1 proportion with OCs culture medium, without cytokines supplementation, which significantly lowered the %ES in comparison to its control (**Figure IV. 6A**). There was some heterogeneity between samples, which can justify the lack of significant differences. Interestingly, the same trend was observed in terms of cell morphology and cell activity (**Figure IV. 4** and **Figure IV. 6A**). Thus, the results obtained during the assessment of the resorptive activity corroborated the previous observations with respect to the morphology and cell number, i.e., 4T1.2 CM by itself was not able to increase the activity of OCs, but the addition of exogenous cytokines resulted in activity levels comparable with the control.

To address if there were alterations on osteoclastic aggressiveness upon stimulation with 4T1.2 cancer cells secretome, the predominant type of resorption event (pit or trench) was determined by calculating the %trench surface/ES. If trenches represented more than 50% of the eroded surface, this type of resorption event was considered predominant and OCs classified as more aggressive, whereas values below that limit defined less aggressive OCs. No significant differences were detected between conditions; therefore, the treatment did not interfere with the level of aggressiveness of the cultured cells (**Figure IV. 6B**). Trench-resorption mode was the predominant profile, even though there was a high variability within each condition. In fact, some bone slices did not present any resorptive events, which lowered the average %trench surface/ES and increased the variability. Pits are associated with intermittent resorption, which is interrupted by migration episodes. On the other hand, trenches result from longer and faster (two times faster) continuous resorption concomitant with cell migration, generating long-distance erosion surfaces (several 100 μm). Hence, the trench-resorption mode is usually associated with higher aggressiveness, even because trench-shaped resorption events favor bone fragility.^{21,130} Consequently, OCs were committed to the most aggressive mode, albeit exhibiting a low resorptive activity.

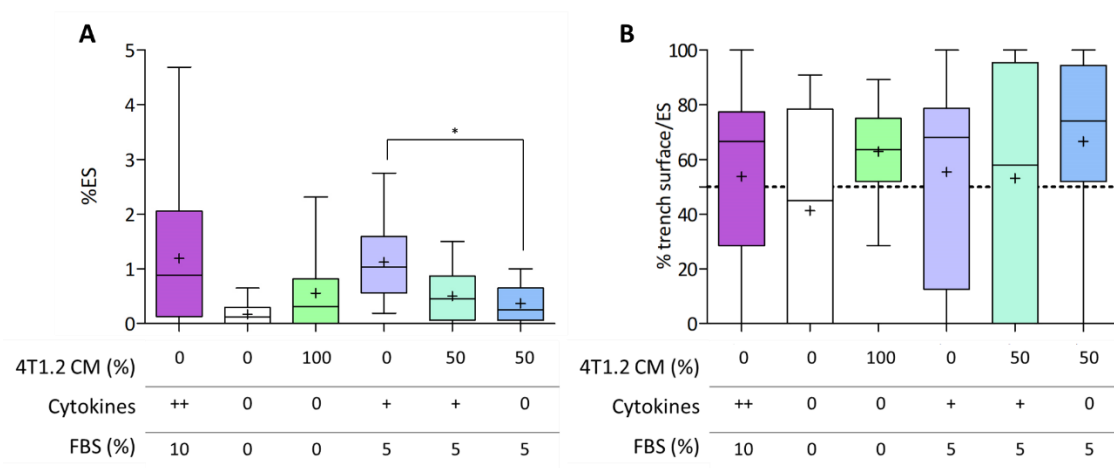


Figure IV. 6 – Effect of 4T1.2 CM on OC activity (Day 4, 6 h of stimulus). **A.** Resorptive activity of OCs represented by %ES. **B.** %trench surface/ES. The dashed line corresponds to %trench surface/ES = 50. Regarding the symbols used in the descriptive tables below each condition: ++ = 30 ng/mL M-CSF and 100 ng/mL RANKL, + = 15 ng/mL M-CSF and 50 ng/mL RANKL. Data represented as box & whiskers plots (box from the first quartile to the third quartile, line represents the median, + corresponds to the mean and whiskers represent minimum to maximum range); n=3 independent experiments, 5 technical replicates per experiment. Statistical analysis was performed using one-way ANOVA (Kruskal-Wallis test) and Dunns’ post test for multiple comparisons (* 0.01 < p < 0.05).

As aforementioned, the %ES was low for all conditions. Furthermore, in some of the bone slices, particularly among those used for the positive control, it was possible to observe impressions made by the OCs that were not deep enough to be considered resorption events (**Figure IV. 7A**). Nevertheless, these imprints would probably reach sufficient depth to be classified as resorption events (**Figure IV. 7B**), if OCs were stimulated for longer periods. These observations gave impetus to test an extended treatment. Although the 24 h treatment proved too long for TCPS-seeded OCs, resulting in very few cells by the end of the stimulus, bone slices correspond to a mineralized surface, providing a more favorable substrate for OCs culture. Hence, prolonging the treatment to 24 h appeared as a reasonable strategy.

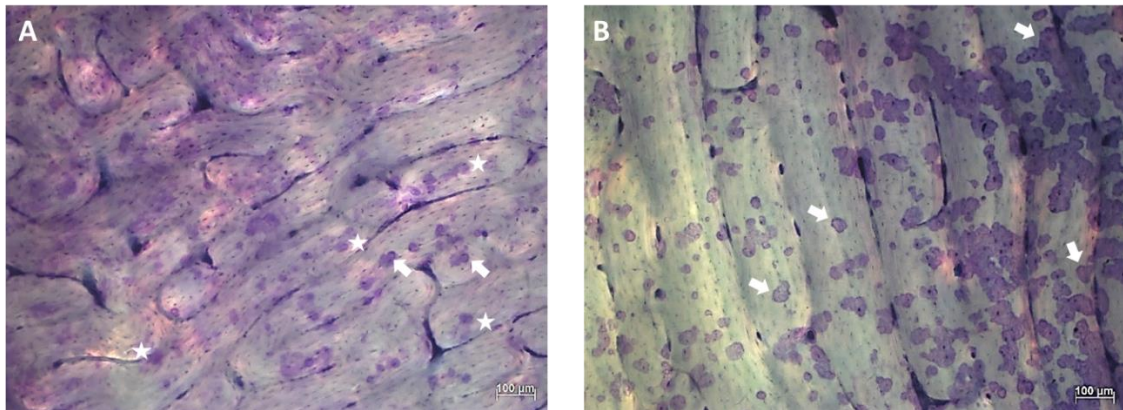


Figure IV. 7 - Impact of longer stimulus on the depth of impressions left by OCs. OCs cultured in α -MEM supplemented with 10% FBS, 30 ng/mL M-CSF and 100 ng/mL RANKL (positive control) submitted to a stimulus of **A.** 6 h or **B.** 24 h. Arrows correspond to examples of resorption events. Stars correspond to impressions made by the OCs that were not deep enough to be considered resorption events. Scale bar indicates 100 μ m.

Altogether, a qualitative analysis of representative images for each condition (**Figure IV. 8**) pointed to an increased %ES with a longer treatment. It should be highlighted that the difference was particularly prominent for the positive control (**Figure IV. 8A**). There was not a striking difference between the conditions where OCs were submitted to 4T1.2 CM and the respective controls (**Figure IV. 8C versus 8B** or **Figure IV. 8E and F versus 8D**).

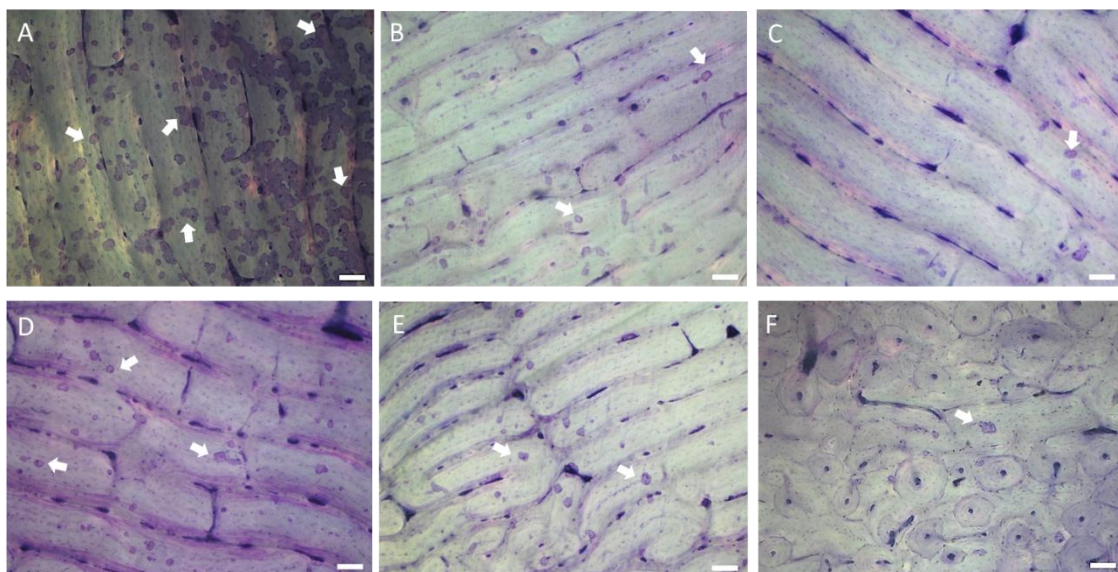


Figure IV. 8 - Representative images of toluidine blue stained bone slices for each condition (Day 5, 24 h of stimulus). OCs cultured in **A.** α -MEM supplemented with 10% FBS, 30 ng/mL M-CSF and 100 ng/mL RANKL (positive control). **B.** α -MEM medium (negative control) **C.** 100 % 4T1.2 CM. **D.** α -MEM medium supplemented with 10% FBS, 30 ng/mL M-CSF and 100 ng/mL RANKL in a 1:1 proportion with α -MEM medium (control for conditions depicted in E and F) **E.** α -MEM medium supplemented with 10% FBS, 30 ng/mL M-CSF and 100 ng/mL RANKL in a 1:1 proportion with 4T1.2 CM. **F.** α -MEM medium supplemented with 10% FBS, in a 1:1 proportion with 4T1.2 CM. Arrows indicate examples of resorption events. Scale bar indicates 100 μ m.

These conclusions were confirmed by the quantitative analysis. Indeed, there were bone slices with nearly %ES = 15 (positive control) or %ES > 5 (OCs in differentiation media in a 1:1 proportion with cancer cells culture media). Furthermore, the mean %ES for these two control conditions was above 2%. However, none of the treatments with 4T1.2 CM led to an augmented osteoclastic activity, not even when key cytokines for osteoclastogenesis were added. As a matter of fact, these conditions had significantly lower levels of %ES when compared with the positive control. On the whole, conditions where 4T1.2 CM was applied to OCs led to the lowest values of %ES (**Figure IV. 9A**). Regarding the predominant type of resorption event, it became more evident that the trench-resorption mode was the prevalent profile with a longer treatment, since the mean %trench surface/ES was above 50% for all conditions. Once again, the treatment did not interfere with the predominant type of resorption mode, as there were no significant differences (**Figure IV. 9B**).

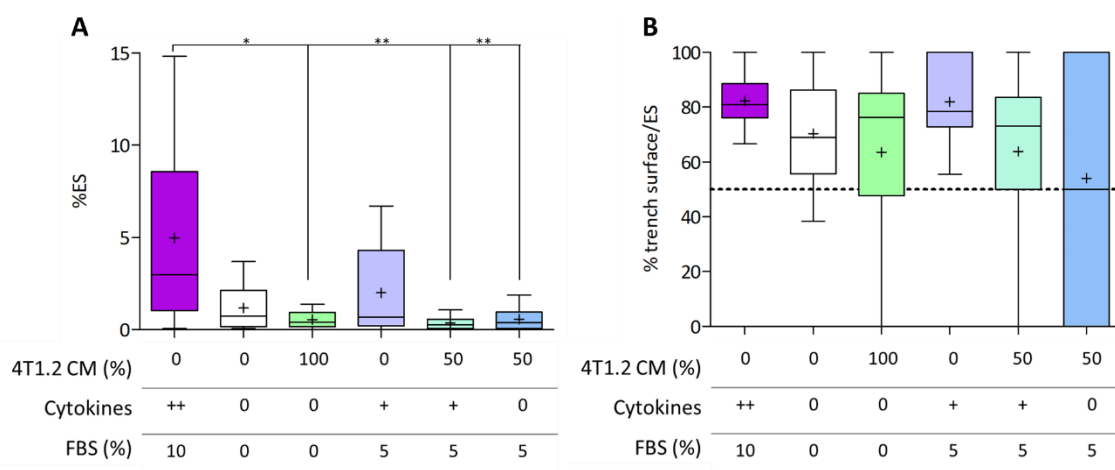


Figure IV. 9 - Effect of 4T1.2 CM on OC activity (Day 5, 24 h of stimulus). **A.** Resorptive activity of OCs represented by the %ES. **B.** %trench surface/ES. The dashed line corresponds to %trench surface/ES = 50. Regarding the symbols used in the descriptive tables below each condition: ++ = 30 ng/mL M-CSF and 100 ng/mL RANKL, + = 15 ng/mL M-CSF and 50 ng/mL RANKL. Data represented as box & whiskers plots (box from the first quartile to the third quartile, line represents the median, + corresponds to the mean and whiskers represent minimum to maximum range); n=3 independent experiments, 5 technical replicates per experiment. Statistical analysis was performed using one-way ANOVA (Kruskal-Wallis test) and Dunns' post test for multiple comparisons (* 0.01 < p < 0.05, ** 0.001 < p < 0.01).

These results were partially in line with what was observed in terms of morphology and cell number. Indeed, when OCs were stimulated with 100% 4T1.2 CM or 50% 4T1.2 CM without the addition of cytokines, there were fewer cells than in the positive control and the characteristic osteoclastic morphology was impaired. Meanwhile, the addition of RANKL and M-CSF to the 50% 4T1.2 CM led to comparable results with the control in terms of cell number, both when the TRAP staining and the F-actin immunostaining were performed. The osteoclastic phenotype was also preserved, and the characteristic actin structures were noticed. Consequently, it was expected that the addition of cytokines (RANKL and M-CSF) to the 4T1.2

CM would guarantee equivalent levels of eroded surface in comparison with the control condition, which did not occur (**Figure IV. 9A**).

To better understand the impact of an extended treatment in the resorption activity, the %ES was compared between the two timepoints for all conditions (**Figure IV. 10**). The %ES was higher with the 24 h treatment, but the difference was only significant in the positive control. There was also an increase for the two remaining controls (0% 4T1.2 CM, no cytokines, 0% FBS and 0% 4T1.2 CM, cytokines +, 5% FBS), but the difference did not reach statistical significance. However, for the conditions where OCs were exposed to 4T1.2 CM, the %ES was only very slightly increased with a prolonged treatment. These findings ruled out the possibility of having a reduced %ES when applying 4T1.2 CM due to a short stimulus, because 24 h were clearly sufficient to have appreciable resorption in the control conditions.

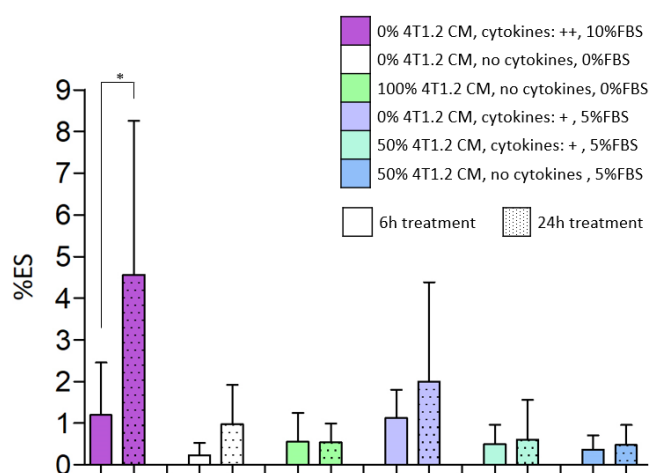


Figure IV. 10 - Impact of longer stimulus in %ES. Cytokines: ++ corresponds to the presence of RANKL at 100 ng/mL and M-CSF at 30 ng/mL, while cytokines: + corresponds to RANKL at 50 ng/mL and M-CSF at 15 ng/mL. Results are expressed as mean + SD (n=3 independent experiments, 5 technical replicates per experiment). Statistical analysis was performed using one-way ANOVA (Kruskal-Wallis test) and Dunns' post test between the two timepoints for each condition (* 0.01 < p < 0.05).

In similar assays with human OCs, resorption pits usually appear only after 3-14 days (varies in accordance with the maturation stage of the OCs when seeded and the factors present in the culture medium). Notwithstanding, human OCs have a longer lifespan than murine OCs (2-3 weeks *versus* 3 days)¹²⁹. Thus, assuming there is a proportion between the lifespan of OCs and the time required for resorption to start, resorption pits should appear after 0,5-3 days in assays with murine OCs. In view of the above, the shorter treatment (6 h) corresponded indeed to a narrow time window, not providing enough time for OCs to complete the resorption process. On the other hand, 24 h were within the timeframe required for resorption events to be formed. Hence, the reduced %ES calculated for all conditions (excluding the positive control) was puzzling, particularly because the addition of exogenous cytokines previously guaranteed the maintenance of OC morphology and number. Nonetheless, the concentration used might not be enough to foster OC activity, since resorbing bone matrix represents an additional effort for the cells. Accordingly, increasing cytokines concentration is a possible solution to overcome the low %ES. In addition, it should be noted that even under some cell damage, OCs are still able to degrade the bone matrix. As such, prolonging the stimulus for more than 24 h (up to 3 days,

for example) could result in higher %ES for the remaining conditions, where OCs were not under optimal circumstances.

Exposure to 50 % 4T1.2 CM resulted in deeper and bigger resorption events

The previous analysis focused mainly on the quantitative aspect of resorption, expressed as percentage of %ES, although the type of resorption event was also considered. Aiming towards a more comprehensive analysis of the impact of tumor cells on OCs resorption activity, the BonePit software¹¹⁹ was used as complementary tool to quantify some pertinent morphologic parameters, such as depth, volume, aspect ratio and top surface area, in 3D reconstructions of resorption events, also produced by the software. In order to do so, a representative bone slice was chosen for each condition (both %ES and %trench surface/ES were considered for this choice) and stained with calcein. Images from selected sections were acquired using a confocal microscope. Subsequently, for all conditions, a pool of 6 resorption events was analyzed with the software and the morphological parameters already mentioned were calculated. Given that the previous results showed 24 h were required for resorption events to be completely formed, only the bone slices from this timepoint were used for the study.

The 3D reconstructions represented an extremely valuable tool, as they provided a clear depiction of the resorption events for each condition (**Figure IV. 11**). The condition replicating OCs in physiological environment (positive control) led to the resorption events with the highest volume and top section area (**Figure IV. 12A and C**), following the same trend as the results obtained in terms of %ES, which also reached the maximum value for this condition (**Figure IV. 9A**). The negative control and the condition in which OCs were submitted to 100% of 4T1.2 CM resulted in the resorption events with the lowest values of volume, top section area and depth. Surprisingly, the tendency noticed in terms of volume and depth for the last three conditions was in opposition with the previous observations with regard to %ES. Indeed, exposure to 50% 4T1.2 CM did not increase the total area of resorption but resulted in bigger and deeper resorption events (**Figure IV. 12A and B**, respectively). Perhaps more surprisingly, this effect was more pronounced when no exogenous cytokines were added. With respect to the top section area, exposure to 50% 4T1.2 CM (with or without supplementation of cytokines) produced values comparable to the control. Concerning the aspect ratio, which is a measure of the circularity of the resorption event, no major differences were observed between conditions (**Figure IV. 12D**). The mean aspect ratio was globally close to 1, regardless the condition.

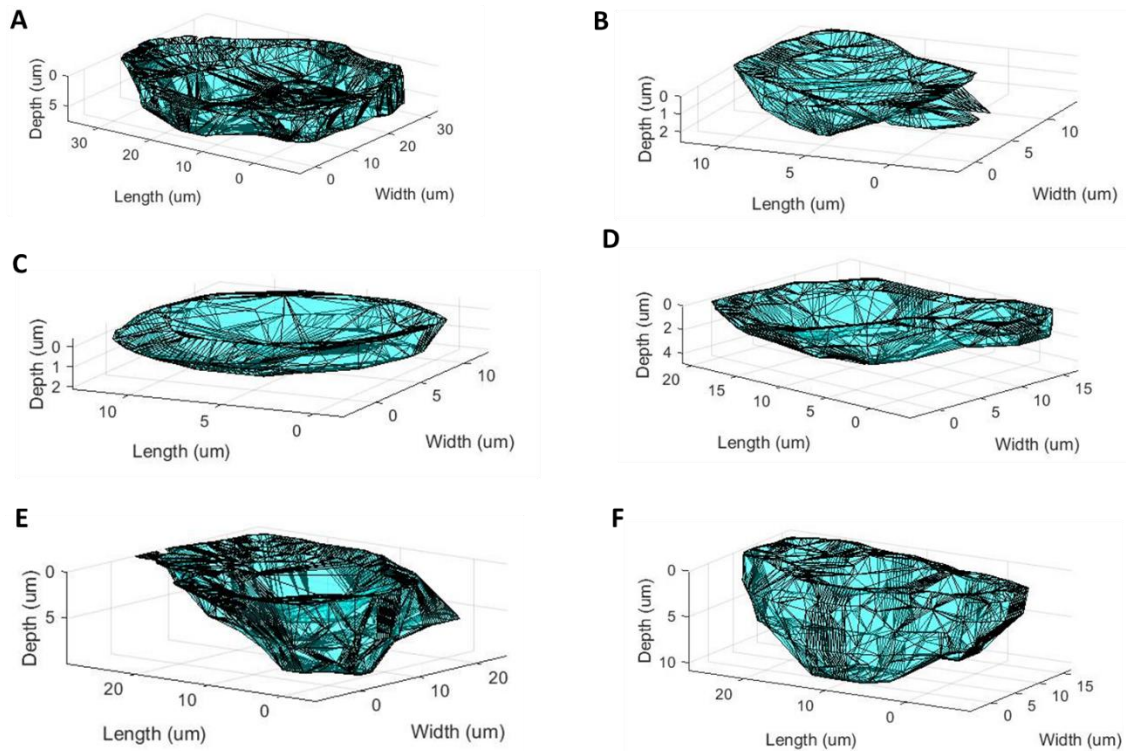


Figure IV. 11 - Representative 3D reconstructions of resorption events obtained using BonePit. Resorption events created by OCs cultured in **A.** α -MEM supplemented with 10% FBS, 30 ng/mL M-CSF and 100 ng/mL RANKL (positive control). **B.** α -MEM medium (negative control) **C.** 100% 4T1.2 CM. **D.** α -MEM medium supplemented with 10% FBS, 30 ng/mL M-CSF and 100 ng/mL RANKL in a 1:1 proportion with α -MEM medium (control for conditions depicted in E and F) **E.** α -MEM medium supplemented with 10% FBS, 30 ng/mL M-CSF and 100 ng/mL RANKL in a 1:1 proportion with 4T1.2 CM. **F.** α -MEM medium supplemented with 10% FBS, in a 1:1 proportion with 4T1.2 CM.

The increase in the depth and volume of resorption events when OCs were exposed to 50% 4T1.2 CM (comparing with the respective control), which was even more pronounced for the condition lacking exogenous cytokines, opened the door for a possible connection between the impact of cancer cells' secretome on morphology and the effect on the resorptive activity. It was observed that the characteristic actin structures usually found in OCs, such as filopodia, were deteriorated in the TCPS-seeded OCs in the analogous condition. Filopodia are cellular projections used for cell migration; if these structures are somehow damaged, OCs cannot competently migrate. Hence, OCs could be active and able to carve the bone slice, but perhaps were not able to migrate. Consequently, resorption occurred on the same site continuously, which resulted in less but deeper and bigger resorption events.

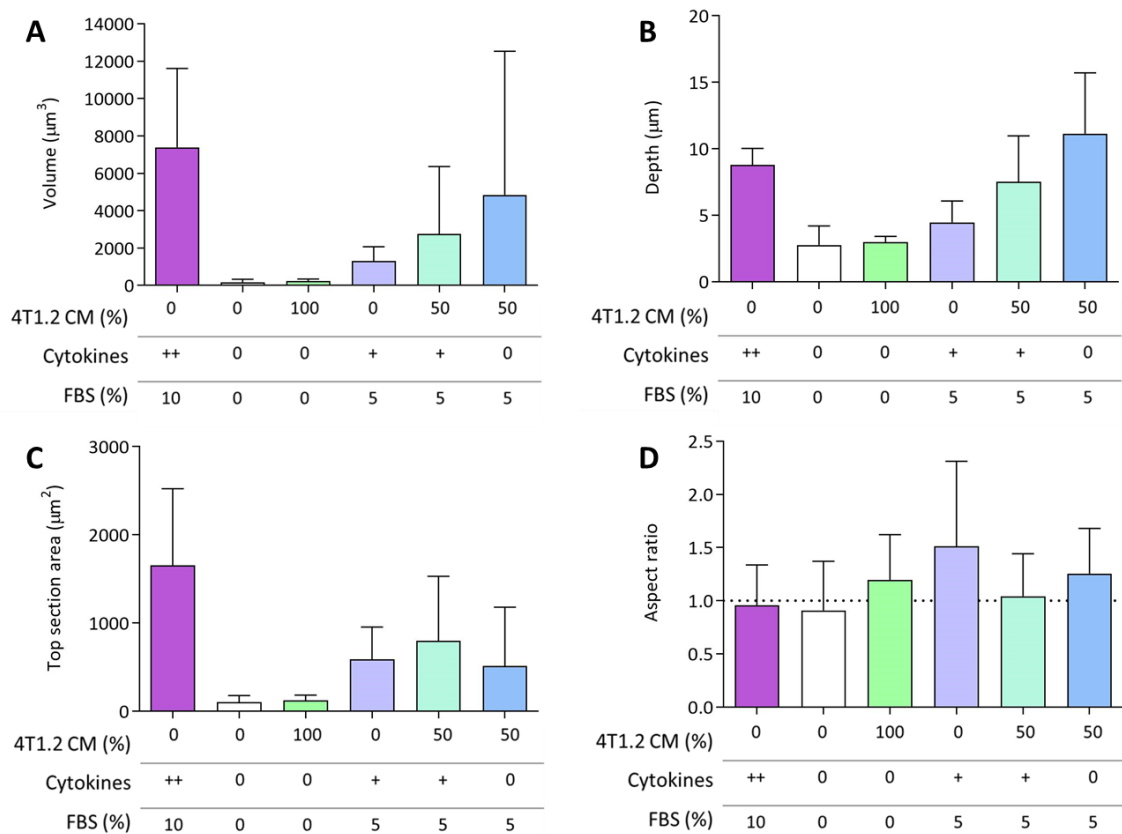


Figure IV. 12 - Quantification of morphologic parameters in 3D reconstructions of resorption events using BonePit. **A.** Volume is obtained by multiplying the number of pixels in the outline per the voxel size. **B.** Depth is calculated by subtracting the minimum layer index from the maximum layer index and then multiplying that result by the step size used to acquire the stacked images (0,29 µm). **C.** Top section area corresponds to the multiplication between the number of pixels on the first outline (first layer of the resorption event) by the pixel area. **D.** Aspect ratio is the result of the division between the maximum length and the perpendicular maximum width of the resorption event. Regarding the symbols used in the descriptive tables below each condition: ++ = 30 ng/mL M-CSF and 100 ng/mL RANKL, + = 15 ng/mL M-CSF and 50 ng/mL RANKL. Results are expressed as mean + SD (n=1, 6 replicates). No statistical analysis was performed.

It should be stressed that the values calculated for the depth, volume and top section area were within the same range of what was previously obtained using this computational tool to analyze resorption events created by bone marrow derived murine OCs.¹¹⁹ Most importantly, similar values for resorption depth were calculated using other techniques.²¹ Additionally, studies with human OCs where the distribution of cell area was assessed show a range that goes from 1000 to 4900 µm²,¹⁸ but murine OCs are usually smaller.^{14,119} Pits and trenches result from the degradation of the bone matrix underneath OCs; thus, their top surface area must be of the same order of magnitude as the size of the OCs. As such, the values found in literature for the size of murine OCs validate our findings.

Higher levels of TRAP activity were detected in TCPS versus bone-slices seeded OCs. TRAP activity correlated with the eroded surface

For a more comprehensive analysis of the BrCa cells' effect in the OC activity, OCs were seeded either on top of TCPS well plates or bovine bone slices, at a density of 5,3 x 10⁴ cells/cm². Treatments with 4T1.2 CM started when fully mature OCs were visible (day 4 of differentiation) and the same conditions previously described were tested. When 6 h of stimulus had passed,

the medium in contact with OCs was collected and the levels of TRAP activity were quantified. Only the CM from OCs submitted to a 6 h stimulus was analyzed, so OCs seeded on a mineralized substrate (bone slices) and a non-mineralized substrate (TCPS) could be compared.

TRAP activity did not differ between conditions for the OCs seeded on the TCPS, which was portrayed by the lack of significant differences (**Figure IV. 13A**). The most distinctive outcome was the positive control, with a significantly higher value of TRAP activity in comparison with the remaining conditions (excluding the negative control). As for the OCs seeded on bone slices, the positive control guaranteed once more the highest levels of TRAP activity (**Figure IV. 13B**). Considering the treatment regimen involving the exposure to 50% 4T1.2 CM combined with exogenous cytokines, TRAP activity was equivalent to the respective control and even to the positive control (**Figure IV. 13B**). The lack of exogenous RANKL and M-CSF, on the other hand, led to significantly lower levels of TRAP activity. When OCs were exposed to 100% 4T1.2 CM, TRAP activity dropped to the levels observed with the negative control. Interestingly, the levels of TRAP activity in TCPS seeded-OCs were higher than the ones calculated for OCs seeded on bone slices. Indeed, almost all plotted values were above 1000 pmol/min in TCPS, whereas all the measurements in bone slices were below this level.

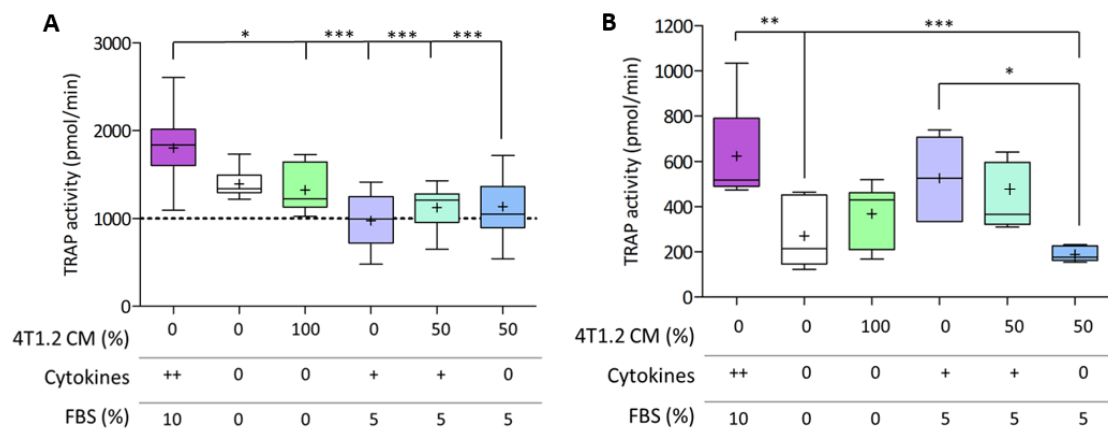


Figure IV. 13 - Quantification of TRAP activity in OCs CM. Values obtained for **A.** TCPS-seeded OCs or **B.** bone slice-seeded OCs. TRAP activity was normalized for the reaction time in each experiment. Regarding the symbols used in the descriptive tables below each condition: ++ = 30 ng/mL M-CSF and 100 ng/mL RANKL, + = 15 ng/mL M-CSF and 50 ng/mL RANKL. Data represented as box & whiskers plots (box from the first quartile to the third quartile, line represents the median, + corresponds to the mean and whiskers represent minimum to maximum range); n=3 independent experiments, 3 technical replicates per experiment. Statistical analysis was performed using one-way ANOVA (Kruskal-Wallis test) and Dunns' post test for multiple comparisons (* 0.01 < p < 0.05, ** 0.001 < p < 0.01, *** p < 0.001).

The higher levels of TRAP activity in TCPS seeded-OCs in comparison with bone slices were not unforeseen, because a similar tendency was observed in other studies, comparing the TRAP activity levels in the CM of OCs seeded on different substrates.²⁴ There is no mineralized substrate to degrade when the OCs were seeded on TCPS, therefore TRAP was merely released to the medium. On the other hand, when OCs were seeded on top of bone slices, the enzyme actively degrades bone matrix. Interestingly, the active isoform 5b has been described to be partly internalized during matrix degradation¹³¹, which might explain the lower levels of TRAP activity detected in the media when bone slices were the substrate.

Evidences indicate both an extracellular and an intracellular role for TRAP. In fact, TRAP is found in the extracellular bone matrix, close to the ruffled border of resorbing OCs. The medium collected for the quantification of TRAP activity was in contact with OCs. Therefore, the focus of the analysis was on the extracellular TRAP levels. It should be noted that TRAP is sensitive to pH and studies have shown its activity *in vitro* can vary considerably, even with small pH fluctuations. Inclusively, the extracellular levels of TRAP activity were higher at a neutral pH (7.0) than at a more acidic pH (6.8) for OCs seeded on TCPS. *In vitro* studies have shown a correlation between the quantification of TRAP activity and the number of OCs formed on TCPS and bone slices.²⁴

In the present work, the profile obtained for the OCs seeded on the bone slices in terms of TRAP activity (**Figure IV. 13B**) was analogous to the results with the toluidine resorption assay (**Figure IV. 6A**). Hence, the enzyme activity was consistent with the eroded surface. On the other hand, treatment with 50% 4T1.2 CM supplemented with exogenous cytokines led to a higher cell number than the negative control and the treatment with 100% 4T1.2 CM (**Figure IV. 4**). In addition, the osteoclastic morphology was undeniably more preserved in this condition than with 100% CM. However, in terms of TRAP activity, these two conditions resulted in equivalent outcomes. Consequently, there was not a perfect correlation between the quantification of TRAP activity and the number of OCs formed on TCPS. It is important to refer the last three conditions portrayed on the graphs resulted in a higher cell number in comparison with the negative control and 4T1.2 CM (100%). More cells imply more metabolites, which acidify the medium, especially considering it was an OC cell culture. Consequently, a possible explanation for the discrepancy between the quantification of TRAP activity and the number of OCs formed lays on a lower pH for the conditions with more cells, which resulted in suboptimal TRAP activity. These results were established by 3 independent experiments and there is some variability between assays. Therefore, increasing the number of experiments could help clarifying and confirming these outcomes.

The objective for the first part of the work comprised the characterization of the morphology, cell number and activity of OCs under malignant tumorigenic stimulus. In view of all the results presented above, the take home messages regarding the cancer cells effect on OCs were the following:

- The 4T1.2 CM was only able to maintain a reasonable OC morphology and cell number if supplemented with exogenous cytokines (M-CSF and RANKL).
- The 4T1.2 CM supplemented with exogenous cytokines did not increase osteoclastic activity, rather maintaining the %ES and TRAP activity at the same levels or lower than the control. However, resorption events resulting from this treatment exhibited an increased volume and depth.

BrCa is associated with osteolytic bone metastases, thus increased bone resorption. The vicious cycle established between BrCa cells and OCs is thoroughly described: cancer cells release BMFs that ultimately increase osteoclastic activity, which results in enhanced bone resorption and release of BSGFs that contribute to increased proliferation of tumor cells.^{20,32,132} Hence, at first sight, the results obtained were surprising, because an increase in cell number

and/or activity following the treatment with 4T1.2 CM was expected and did not occur. Nevertheless, a key player to take into consideration in the equation is RANKL, which is directly responsible to increase osteoclastogenesis and osteoclastic activity, because it is the factor prompting OC precursors' differentiation into OCs.¹³³

4T1.2 cells had residual RANKL mRNA expression. No RANKL protein was detected in the CM

In order to understand the mechanism of action behind the impact of BrCa cells in bone dynamics, 4T1.2 cells were cultured in serum-free medium for 24 h, their CM was collected and, subsequently, RNA was extracted from the BrCa cells. RANKL mRNA was then quantified by RT-qPCR, while ELISA was used to quantify RANKL protein levels in the CM. RANKL mRNA expression levels were residual (below $2,0 \times 10^{-6}$) and markedly lower than the positive control (**Figure IV. 14**). RNA extracted from MC3T3-E1 cells, a preosteoblastic cell line, widely used for studies involving *in vitro* OB differentiation, with proved RANKL expression¹³⁴⁻¹³⁶ was used as control. Regarding the protein levels, no RANKL was detected in the 4T1.2 CM. The sensitivity limit of the assay is 5 pg/mL, so RANKL was either present at a very residual level or not present at all, which was in compliance with the outcome at the transcriptional level.

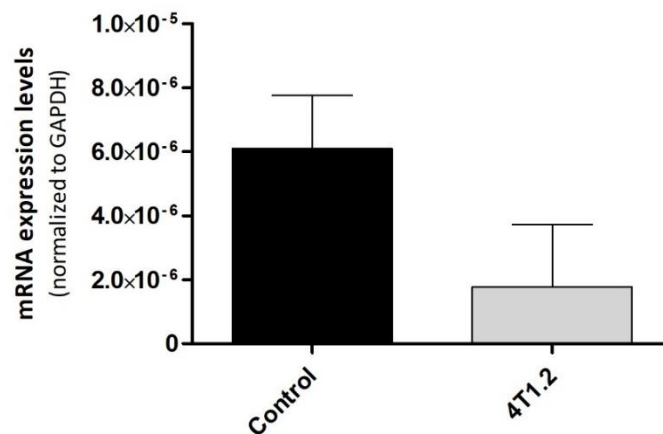


Figure IV. 14 - RANKL expression levels in the 4T1.2 cell line. Expression was normalized to the reference gene GAPDH. Data is expressed as mean + SD (n=2, 3 replicates per experiment). Statistical analysis was performed using Mann-Whitney t test. Statistical differences were considered when $p < 0.05$.

Data from different studies regarding RANKL expression in BrCa cell lines are contradictory.^{137,138} For example, no RANKL expression was detected at the mRNA level in MCF-7 and MDA-MB-231¹³⁹, two cell lines widely used in BrCa research. However, RANKL protein expression was detected in the same cell lines in different studies.^{140,141} As aforesaid, the impact of BrCa cells in OCs can be direct or indirect and that seems to differ according to the cell line used. The 4T1.2 cell line has been described to increase plasma PTH-rP and calcium levels and actively secrete PTH-rP,¹¹⁷ which are markers of increased bone resorption. No data was found regarding RANKL expression. Nonetheless, a murine pre-OC cell line (RAW 264.7) was maintained for 6 days in 4T1.2 CM or in normal cell culture media supplemented with a low concentration of RANKL (20 ng/ml) and no CM. An equivalent number of OCs was observed in the two conditions. Moreover, treatment with 4T1.2 CM supplemented with RANKL (20 ng/mL) led to similar levels of OCs, in comparison with a high concentration of RANKL (50 ng/mL),¹⁴² which is in line with what was portrayed in this work. Additionally, a different study showed a 4T1 CM induced RANKL expression in OBs.¹⁴³ Combining all these findings with the presented

results, an indirect impact on osteoclastic maintenance and activity, mediated by 4T1.2 CM-induced RANKL expression in OBs and stromal cells, rose as the most likely mechanism of action behind the impact of this cell line in bone dynamics. As a matter of fact, bone marrow stromal cells, OBs and osteocytes have been described as the major source of M-CSF and RANKL in the normal bone microenvironment.¹³³ The absence of OBs, osteocytes or stromal cells in the studied model can explain why cell number and activity was not increased in the presence of 4T1.2 CM, meeting comparable levels with the control only upon exogenous cytokine supplementation.

Technical considerations

Microfluidics, an array of technologies operating with volumes that range from pL to μL ¹⁴⁴, were the platform chosen to support the second part of the studies, where the nervous system comes into play. These platforms have been widely used for the assembly of *in vitro* models, as they allow a reliable miniaturization of biological processes, coupled with design flexibility to personalize each device to mimic a specific cellular microenvironment. A higher control of experimental parameters, easy handling, good reproducibility or efficient combination with high throughput imaging analysis techniques are further advantages. In addition, their production is a cheap process and implies less consumption of reagents.^{116,144,145} This last characteristic is particularly important given the fact that our study involved the use of a limited stock of CM. The same volume of CM could be used for more replicas of the same experiment in microfluidics than in macroscopic cell culture platforms (such as well plates or Petri dishes). That said, a more robust set of results could be obtained, further solidifying the withdrawn conclusions. There is a segment within the microfluidic platforms that offered special advantages for our study: the compartmentalized microfluidic devices. In fact, only the axonal terminals of the sensory neurons are present in the bone tissue, since their cell bodies are contained in the DRG next to the spinal cord.^{26,76,146} Accordingly, a correct recapitulation of the interaction between OCs and nerve cells should contemplate the physical separation between soma and axonal structures. The microfluidic devices chosen followed the most traditional design – two compartments parted by microgrooves that enabled axonal isolation from the cell body, with an additional smaller open compartment that allowed the DRG seeding (organotypic culture). This architecture has been effectively used with mouse embryonic DRG cultures.^{76,116}

Another relevant aspect to take into consideration was the material selected for the microfluidics. PDMS is one of the most common materials in microfluidics for cell culture due to properties such as its biocompatibility, optical transparency (required for microscopy analysis) and gas permeability, which allows oxygen supply to the culture, as well as the removal of the carbon dioxide arising from cellular activity. Additionally, it is flexible and elastic, thus easy to mold. Hence, it can be used to produce microfluidic devices with complex architectures, using soft lithography, in a cost-effective manner. Furthermore, PDMS can be reversibly and irreversibly bond to glass, plastic and other materials to create closed chambers, avoiding culture medium leakage.^{144,145} Most importantly, PDMS based microfluidic devices have been efficaciously used for murine DRG explant cultures.^{76,146} Considering all the above characteristics, PDMS arose as a suitable material for our studies. The surface properties were an additional aspect to be considered when using this material. PDMS is hydrophobic, therefore it had to be coated with molecules that promote cellular attachment, namely PDL and laminin. PDL creates a net positive charge on the surface, due to the amino groups located at the extremity of each lysine, increasing the hydrophilicity and promoting the interaction with the negatively charged membrane.¹⁴⁵ Laminin is a large adhesive glycoprotein essential for the axonal extension. It binds to the positive charges of PDL, further enhancing cell adhesion and making PDMS a suitable material for the DRG (and other neuronal cultures).^{147,148} The PDMS pieces were sealed with a glass coverslip; so DRG (cell body and the axons) were in contact with the glass. Consequently, it is worth noticing that this surface was also coated with PDL and laminin.

While the substrate for cell culture is an important building block of the *in vitro* model, cells play the central role in the study. The axons of the sensory nerve fibers found in bone tissue have their correspondent cell bodies located on the DRG next to the spinal cord.^{26,28} Moreover, rodent DRG have been extensively and successfully used in studies exploring the cellular mechanisms behind pain and neurodegeneration associated with disorders of the peripheral nervous system.¹⁴⁹ For these reasons, mouse DRG appeared as a logic choice for the current *in vitro* model. After being dissected from the spinal column, DRG can be dissociated to obtain primary neuronal cultures. Alternatively, the entire DRG can be used for cell culture, which is designated as an explant organotypic culture. This option resembles more closely the physiological structure, since the extracellular microenvironment is maintained, and the entire neuronal network is preserved. Therefore, using DRG explants is a more robust and flexible system to model peripheral neuropathies and explore disease mechanisms,^{150,151} which justifies their inclusion in the experimental setup. Although studying a condition usually observed in adult patients, embryonic DRG explants proved preferable due to their technical advantages, namely the ability to establish a complete neurite network in a shorter period in comparison with adult DRG explants.¹⁵²

Evaluation of neurotrophic potential of BrCa and OCs CM

DRG explants obtained from 16-18 days mouse embryos were seeded on PDMS based microfluidics previously coated with PDL and laminin. DRG were left undisturbed for 24 h in neurobasal medium supplemented with NGF. Subsequently, the axonal terminals were stimulated with CM from the different conditions for 72 h. Finished the stimulus, an immunostaining against β III-tubulin was performed so the axonal outgrowth could later be quantified. AxoFluidic, a semi-automated algorithm written using MATLAB¹¹⁶, was used to perform the quantification. Embryonic DRG obtained from a different female were considered for each independent experiment. While on the somal compartment, DRG were always maintained in neurobasal medium supplemented with NGF regardless the condition, different combinations were used to stimulate the axonal compartment according to the question to be answered. It is worth mentioning that a volume difference of over 75 μ L was maintained between the two compartments during the treatment with CM, to ensure an efficient fluidic isolation and exclusive localization of the CM in the axonal compartment. This volume difference is in accordance with the recommendations provided in standard protocols for the microfluidic platforms used for neuronal culture.¹²⁰

DRG need to be manipulated very cautiously, since they are delicate and small. Thus, excessive handling can lead to the dissociation of the explant. Consequently, not all DRG were seeded precisely at the same distance from the microgrooves, because repositioning them could eventually result in their disaggregation. Although 24 h proved enough to observe the formation of a neurite network in DRG (ensuring the correct development of the explant), some neurite networks were denser and/or longer than others. To guarantee that this variability did not have an impact on the conclusions about the axonal outgrowth, in each experiment, all DRG were assessed before starting the treatment, using an optic microscope. Subsequently, a pool of explants was chosen for each condition in such a way that there was an equivalent distribution in terms of distance of the DRG to the microgrooves, density of the neurite network and neurite length among the various conditions. A stimulus of 72 h has proven long enough for the axons to cross the microgrooves and reach the axonal compartment. At the same time, the length of the stimulus was not too long, so small differences between conditions could still be noticed. The methodology used for the quantification of axonal elongation was based on β III tubulin immunostaining, which is particularly useful for the quantification of axonal outgrowth, since it allows visualizing fine details of axons and its terminations. Manually counting the axons that reached the axonal compartment would be time-consuming and prone to operator error. The semi-automated algorithm used allowed a fast, robust and precise quantification, built on a reproducible image analysis method. In this way, the subjectivity associated with a manual quantification was eliminated and more information could be extracted from each image.

Cancer cells secretome enhanced axonal outgrowth

To understand if either the 4T1.2 CM or the CM of OCs in physiological conditions had an impact on the axonal outgrowth, DRG were cultured as earlier described and three conditions were considered for the stimulus: neurobasal medium supplemented with NGF (positive control), 100% 4T1.2 CM and CM from OCs seeded on TCPS, maintained in α -MEM 10% FBS supplemented with M-CSF (30 ng/mL) and RANKL (100 ng/mL) for the differentiation period (4 days) plus the 6 h of treatment during the study of osteoclastic morphology.

Axonal outgrowth was measured after staining against β III-tubulin (**Figure IV. 15A**) and quantified using AxoFluidic. This software provides two important measures: on one hand, it returns the quantity of axons from the somal compartment that reached the axonal compartment (A), a parameter that evaluates the permissiveness to axonal growth. On the other hand, it accurately calculates the axons' length (λ), a parameter related with the ability to promote axonal extension. Concerning permissiveness, in comparison with the positive control, A values were increased under tumorigenic stimulus and decreased under the stimulus of OCs CM. (considering the mean value for each condition). However, the difference was not statistically relevant, which might be explained by the variability in the results (**Figure IV. 15B**). Hence, stimulation with either 4T1.2 or OCs secretome ensured permissiveness to axonal growth comparable to the stimulation with NGF. In terms of axonal extension, the axonal elongation induced by the BrCa cells secretome was significantly higher than the originated by the control or by the OCs CM (**Figure IV. 15C**). The OCs secretome reproduced the axonal elongation observed with NGF stimulation.

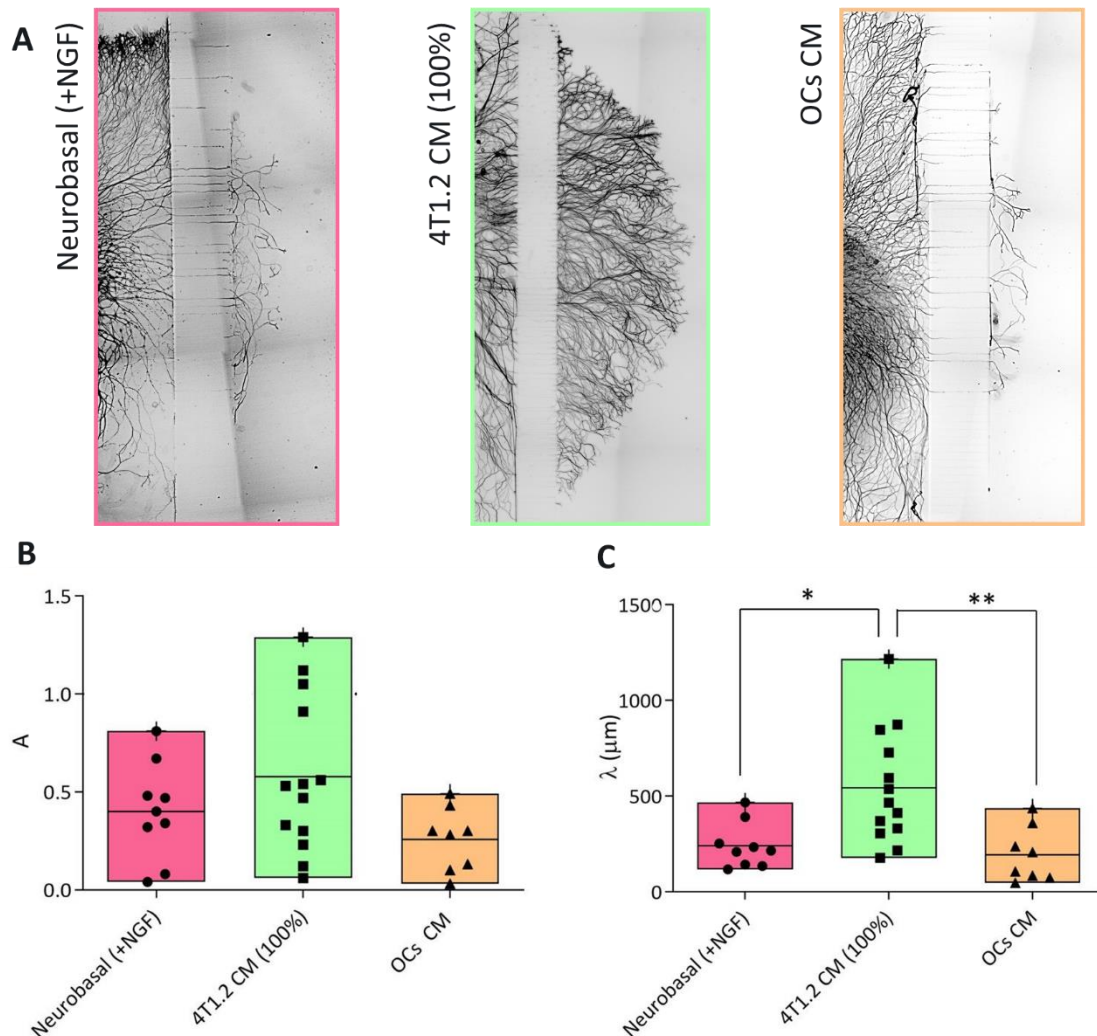


Figure IV. 15 - Assessment of the neurotrophic potential of 4T1.2 cell line and OCs CM. A. Representative images of each condition following β III-tubulin staining. Results obtained in terms of permissiveness, expressed by the B. A values and axonal extension, expressed by the C. λ values. Results are displayed as floating bars: box from minimum to maximum; line plotted at the mean value; the dots, squares or triangles visible in the bars represent replicates (n=3). Statistical analysis was performed using one-way ANOVA (Kruskal-Wallis test) and Dunns' post test for multiple comparisons (* 0.01 < p < 0.05, ** 0.001 < p < 0.01).

NGF tropic signaling is vital for neurons' ability to extend axons, both *in vivo* and *in vitro*.⁴² As such, NGF stimulation promotes axonal outgrowth. In the light of these data, cancer cells secretome demonstrated neurotrophic potential to an even higher extension than the physiological osteoclastic secretome. In conclusion, both cancer cells and OCs were able to promote axonal extension.

OCs neurotrophic potential was unaltered under the tumorigenic effect of 4T1.2 secretome

To evaluate if the neurotrophic potential of OCs could be boosted by previous stimulation with 4T1.2 secretome, the same procedure was followed, only with different conditions. The CM of TCPS-seeded OCs maintained in 50% 4T1.2 CM, 5% FBS, 15 ng/mL M-CSF and 50 ng/mL RANKL was chosen to represent the pathological situation, i.e., OCs under tumorigenic effect. The CM of OCs maintained in 5% FBS, 15 ng/mL M-CSF and 50 ng/mL RANKL was used as control (physiological scenario). It should be noted that the CM from OCs under tumorigenic effect was a combination of the altered OCs secretome plus the 4T1.2 CM, which demonstrated a neurotrophic effect (**Figure IV. 15**). Thus, both the molecules previously released by cancer cells or later by the OCs (under tumorigenic stimulus) could influence the axonal outgrowth. Consequently, an additional control was required: CM where only the 4T1.2 secretome was present, in the same concentration used to stimulate OCs (50%).

The neurotrophic potential was evaluated once again by staining DRG against β III-tubulin (**Figure IV. 16A**) and quantifying axonal outgrowth using AxoFluidic. All conditions produced similar A values, which was corroborated by the lack of significant differences (**Figure IV. 16B**). In terms of axon extension, λ values were higher for all conditions in comparison with the positive control (considering both the average and the maximum values), but the differences did not reach statistical significance (**Figure IV. 16C**). As such, all conditions showed a neurotrophic potential equivalent to the stimulation with NGF. The neurotrophic potential was not boosted when OCs were submitted to the tumorigenic effect, since the results were comparable with the condition representing OCs in physiological conditions, both in terms of permissiveness and axonal extension.

Previously, when addressing OCs morphology and activity, two different 4T1.2 CM concentrations were used – 100% and 50%, the latter being tested both with and without cytokines supplementation. All these three conditions were possible candidates to portray OCs under tumorigenic effect. The one with 50% 4T1.2 CM supplemented with exogenous cytokines was preferred to pursue the neurotrophic effect studies for several reasons. Firstly, it is more physiologically relevant, because factors released by BrCa cells would always be combined with the essential factors for OC development present in the bone microenvironment. Secondly, the results obtained in the first part, together with similar studies exploring the interaction between cancer cells and OCs⁴⁶, indicate the increased OC activity associated with BrCa-derived bone metastases is triggered by cytokine production from OBs and other stromal cells, which is enhanced by tumor cells. This indirect effect on OCs was simulated by the supplementation with cytokines. Lastly, this condition secured the best results with respect to maintenance of OC morphology, while simultaneously holding levels of TRAP activity within the same order of magnitude as the positive control. Hence, the CM collected resulted unequivocally from active OCs.

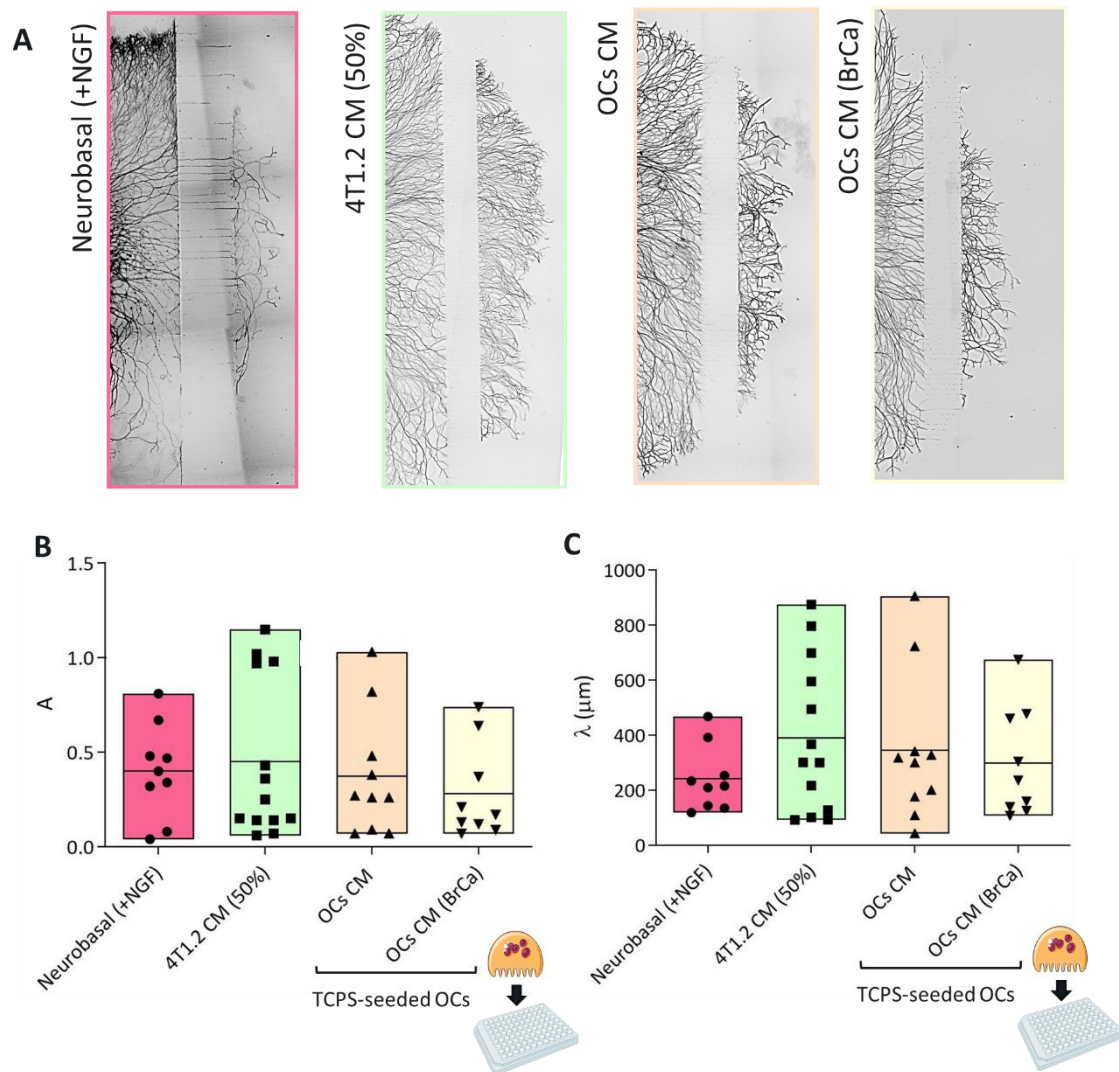


Figure IV. 16 - Assessing how 4T1.2 secretome impacts OCs neurotrophic potential. **A.** Representative images of each condition following β III-tubulin staining. Results obtained in terms of permissiveness, expressed by the **B.** A values, as well as axonal extension, expressed by the **C.** λ values. CM was collected from TCPS-seeded OCs, either in differentiation medium (OCs CM) or stimulated with 4T1.2 CM in the regimen formerly described– OCs CM (BrCa). Results are displayed as floating bars that go from minimum to maximum; the line is plotted at the mean value in each bar; the dots, squares or triangles visible in the bars represent replicates (n=3). Statistical analysis was performed using one-way ANOVA (Kruskal-Wallis test) and Dunns’ post test for multiple comparisons. Statistical differences were considered significant for $p < 0.05$.

Considering the ectopic sprouting observed in the context of CABP, it was anticipated that the tumorigenic effect enhanced OCs neurotrophic potential in comparison with the physiological scenario, which did not occur. Looking back at the results obtained in terms of number of OCs (**Figure IV. 4**) or TRAP activity (**Figure IV. 13A**), there were no significant differences between these two conditions (OCs maintained in 0% CM, 5% FBS, 15 ng/mL M-CSF and 50 ng/mL RANKL *versus* OCs maintained in 50% CM, 5% FBS, 15 ng/mL M-CSF and 50 ng/mL RANKL). OCs were not as active as expected under tumorigenic effect, therefore the neurotrophic potential associated with the corresponding CM was not as high as predicted. It is also relevant to mention that BrCa cells demonstrated some neurotrophic potential. Given there were no significant differences between the control condition where DRG were exposed to 50% 4T1.2 CM and the one where they were stimulated with OCs under tumorigenic effect, it is not completely clear if the neurotrophic potential observed results from the molecules present in

the BrCa cells secretome or from the altered OCs secretome. Most likely, the impact on axonal elongation arose from a combination of both.

Bone matrix degradation products showed a tendency to increase OCs ability to enhance axonal extension in physiological conditions

With the purpose of comprehending if bone degradation products had an impact in the neurotrophic potential of OCs, DRG were cultured as described and stimulated with CM from OCs seeded on TCPS or bone slices, both maintained in α -MEM 10% FBS supplemented with M-CSF (30 ng/mL) and RANKL (100 ng/mL). The neurobasal medium supplemented with NGF was again used as positive control. Axonal outgrowth was measured after staining against β III-tubulin (**Figure IV. 17A**) and quantified using AxoFluidic. No significant differences were found between conditions, neither in terms of A nor λ values (**Figure IV. 17B** and **Figure IV. 17C**, respectively). There was a modest increase in axonal length when the bone matrix degradation products were present, although the difference did not reach statistical significance.

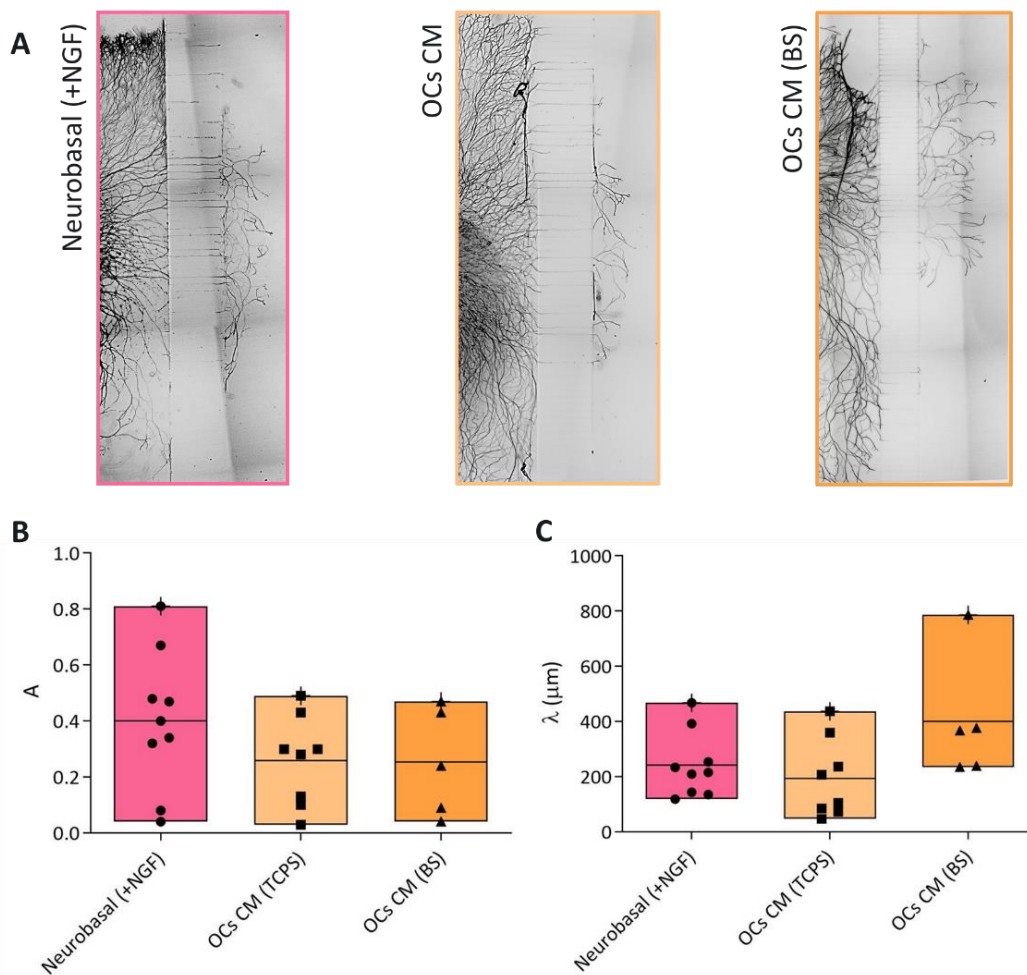


Figure IV. 17 - Impact of bone matrix degradation products in the neurotrophic potential. **A.** Representative images of each condition following β III-tubulin staining. Results obtained in terms of permissiveness, expressed by the **B.** A values, as well as the impact in axonal extension, expressed by the **C.** λ values. CM was collected both from TCPS-seeded (OCs CM (TCPS)) and bone slice-seeded OCs (OCs CM (BS)) cultured in normal differentiation medium. Results are displayed as floating bars that go from minimum to maximum; the line is plotted at the mean value in each bar; the dots, squares or triangles visible in the bars represent replicates (n=3). Statistical analysis was performed using one-way ANOVA (Kruskal-Wallis test) and Dunns' post test for multiple comparisons. Statistical differences were considered significant for $p < 0.05$.

Previous results made clear the described concentrations of cytokines were the ideal for the maintenance of OC morphology and activity (optimal cell culture conditions). Fundamentally, by comparing these two experimental groups, the effect of OCs secretome combined with the bone matrix degradation products (a closer situation to the *in vivo* scenario) *versus* OCs secretome was under review. Bone resorption carried by OCs implies the release of matrix degradation products to the extracellular fluid. Consequently, since OCs were seeded on top of bovine bone slices (a mineralized substrate), the CM collected was enriched with collagen degradation products, together with higher levels of calcium, phosphate and magnesium.^{1,153} The increase in calcium levels is of particular interest because this ion is involved in the regulation of excitable tissues (such as nerve fibers). Complementarily, calcium is involved in signaling pathways associated with the regulation of cytoskeleton, which is highly connected with axon growth and guidance.¹⁵⁴ As a matter of fact, CdCl₂, a CaMKII activator, significantly increased axon length in mice adult DRG neurons. Also expressed in mice embryonic ganglia¹⁵⁵, CaMKII is a kinase activated upon calcium binding, which triggers its autophosphorylation.¹⁵⁶ Calcium-sensing receptor (caSR) is responsible for monitoring systemic, extracellular, free calcium ions, being present in tissues involved in calcium homeostasis. On a similar note to the previous data, elevated extracellular calcium concentrations or the presence of a calcimimetic triggered caSR's activation in late fetal sympathetic neurons, which translated into the enhancement of axonal growth, both in terms of length and branching density.¹⁵⁷ Moreover, studies have showed that hydroxyapatite crystals (the structural unit of bone tissue's mineral component) enhanced axonal outgrowth in the context of nerve injury.¹⁵⁸ Analyzing these findings, the presence of calcium enriched CM, resulting from the contact with OCs seeded on a mineralized substrate, could justify the tendency for a boosted ability to promote axonal length.

Bone resorption also implies the release of BSGFs (such as TGF- β or IGF) from the bone matrix. TGF- β is involved in nerve repair following injury, taking part in the regulation of several associated processes, from glial scar formation to neurite outgrowth.¹⁵⁹ This growth factor was able to foster neurite outgrowth, both in dopaminergic cells¹⁶⁰, differentiated retinal ganglion cells (RGCs)¹⁶¹ and cultured myenteric neurons. In addition, mRNA expression of NGF was increased in cultured rat astrocytes following exposure to TGF- β 1.¹⁵⁹ Likewise, IGF-1 proved necessary to promote axonal growth, either in adult CNS neurons or in RGCs.^{162,163} Such observations support the inclusion of TGF- β and IGF on the list of possible bone degradation products responsible for the tendency to stimulate axonal extension. Quantifying calcium, TGF- β and IGF levels in the CM, containing only the secretome or the later along with degradation products, would be a suitable approach to confirm this hypothesis.

Stimulation with CM from OCs under tumorigenic effect (seeded on a mineralized substrate) replicated the axonal outgrowth observed with NGF stimulation

Lastly, to understand if the neurotrophic potential of OCs was increased following the exposure to the BrCa cells' secretome when OCs were cultured on a mineralized substrate, CM from OCs seeded on the top of bone slices was collected and used to stimulate the axon terminals. Three different conditions were included for this part: CM from OCs maintained in α -MEM 5% FBS supplemented with M-CSF (15 ng/mL) and RANKL (50 ng/mL) during 5 days (differentiation period plus the 24 h treatment) – physiological status; CM from OCs maintained in α -MEM 5% FBS supplemented with M-CSF (15 ng/mL) and RANKL (50 ng/mL) plus 4T1.2 CM

(50%) for the same period – pathological status. The last condition corresponds to the positive control – stimulation with neurobasal medium supplemented with NGF.

For axonal outgrowth to be quantified, DRG maintained in the different conditions were stained against β III-tubulin (**Figure IV. 18A**). In comparison with the condition representing the physiological status, the CM from OCs under tumorigenic effect did not produce a modification in the permissiveness (**Figure IV. 18B**), or in the axonal length (**Figure IV. 18C**). Interestingly, stimulation with OCs CM, either representing the physiological or the pathological status resulted in longer axons in comparison with positive stimulation with NGF. Nonetheless, none of the mentioned differences reached statistical significance. Thereupon the neurotrophic potential associated with OCs secretome combined with bone matrix degradation products was not increased by the exposure to tumorigenic effect, rather replicating the positive stimulation with NGF.

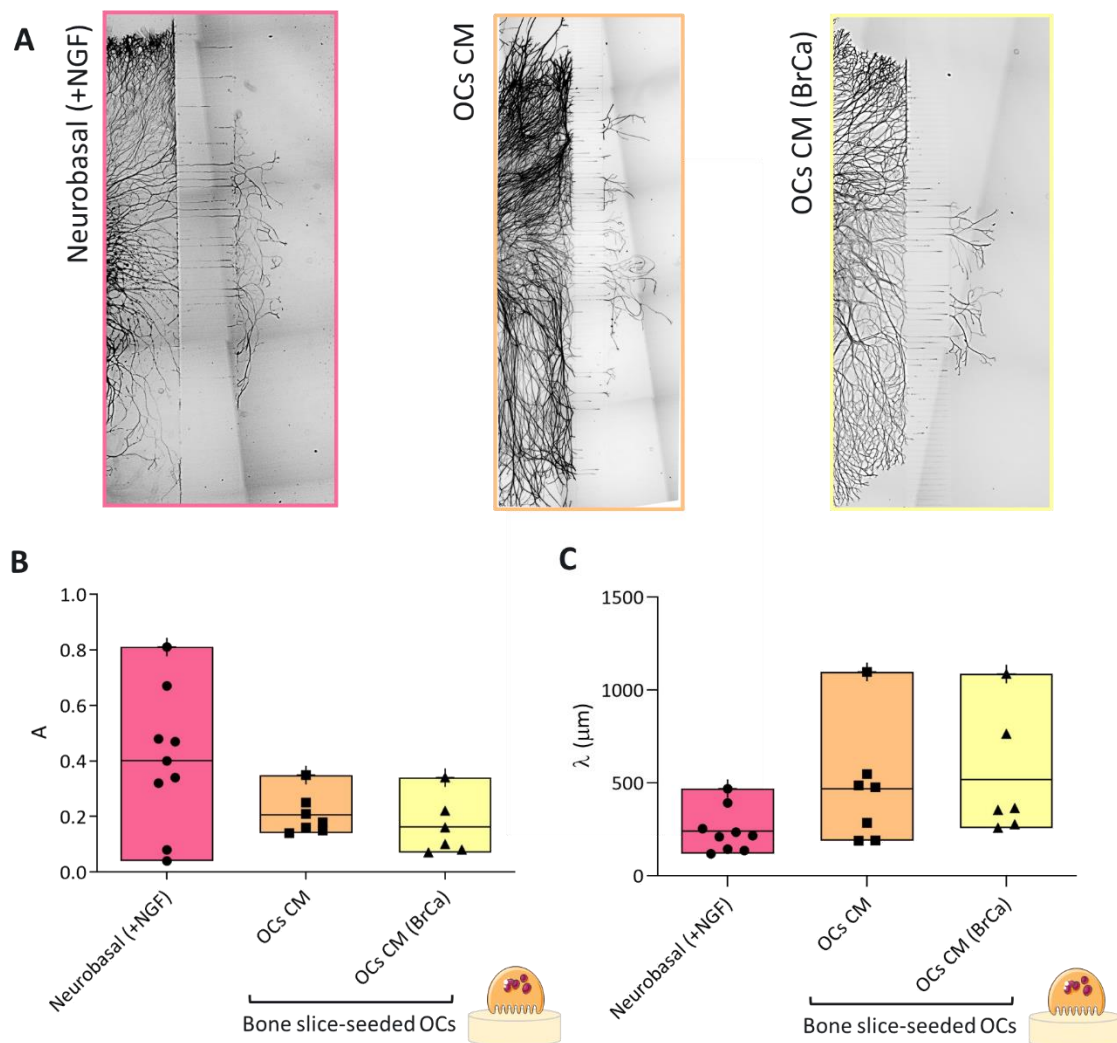


Figure IV. 18 - Evaluation of the tumorigenic effect in the axonal outgrowth for OCs seeded on a mineralized substrate. **A.** Representative images of each condition following β III-tubulin staining. Results obtained in terms of permissiveness, expressed by the **B.** A values, as well as the impact in axonal extension expressed by the **C.** λ values. OCs were either maintained in differentiation media (OCs CM) or exposed to 4T1.2 CM – OCs CM (BrCa). Results are displayed as floating bars that go from minimum to maximum; the line is plotted at the mean value in each bar; the dots, squares or triangles visible in the bars represent replicates (n=3). Statistical analysis was performed using one-way ANOVA (Kruskal-Wallis test) and Dunns' post test for multiple comparisons. Statistical differences were considered significant for $p < 0.05$.

Increasing the number of replicates per condition could ultimately show a more prominent difference between the disease and the normal status, particularly because there was some variability in the results. One must not forget that there is always some heterogeneity between independent experiments. This issue assumes even more relevance when working with primary cultures, in comparison with cell lines. Here, DRG were treated with CM collected on a previous task, so there is a cumulated variability.

Using CM from OCs seeded on bone slices implied that the effect of OCs secretome combined with the bone matrix degradation products was evaluated. The reasons behind the selection of the treatment regimen with 50% 4T1.2 CM combined with exogenous cytokines to represent the pathological situation were formerly explained. Yet again, the fairest comparison with the condition portraying the physiological status implies OCs should be exposed to the same concentration of exogenous cytokines. This being said, the experimental set up was properly established to address the proposed scientific question. As previously explained, an uncontrolled ectopic axonal outgrowth has been detected in numerous animal models of BrCa derived bone metastases. The core objective of the work was to understand if OCs were somehow responsible for this axonal sprouting. Having this in mind, an enhancement of the neurotrophic potential under tumorigenic stimulus was expected, but it did not happen. Recalling the earlier outcomes, where the impact of BrCa cells secretome in OCs was covered, there was not a significant increase in the osteoclastic activity, neither when the TRAP activity levels were quantified (**Figure IV. 13B**), nor when the eroded surface was calculated (**Figure IV. 9A**). As such, the maintenance of the neurotrophic potential was in accordance with the maintenance of osteoclastic activity.

OCs express Netrin 1 at low levels

Overall, the CM from OCs maintained in normal conditions or stimulated with BrCa cells CM promoted axon extension, as the results were comparable with the outcomes under NGF stimulation. In a quest to identify the molecules released by OCs that could trigger axonal outgrowth, OCs were seeded in TCPS well plates, differentiated for 4 days and then submitted to a 6 h stimulus, upon which the RNA was extracted. Subsequently, Netrin 1 expression was quantified by RT-qPCR. The analysis was performed only for the conditions whose CM entered the evaluation of neurotrophic potential. Results showed reduced levels of expression in comparison with the control (total RNA extracted from 16-18 days mouse embryos' lung tissue, where Netrin-1 expression has been described¹⁶⁴) regardless the condition. Indeed, mRNA expression was 10 to 20-fold higher in the control (data not shown). Focusing on the experimental conditions, Netrin 1 expression was slightly higher when OCs were submitted to the tumorigenic effect, but the difference was too modest to reach statistical significance (**Figure IV. 19A**). Likewise, the neurotrophic potential did not increase under tumorigenic stimulus (**Figure IV. 19 B and C**).

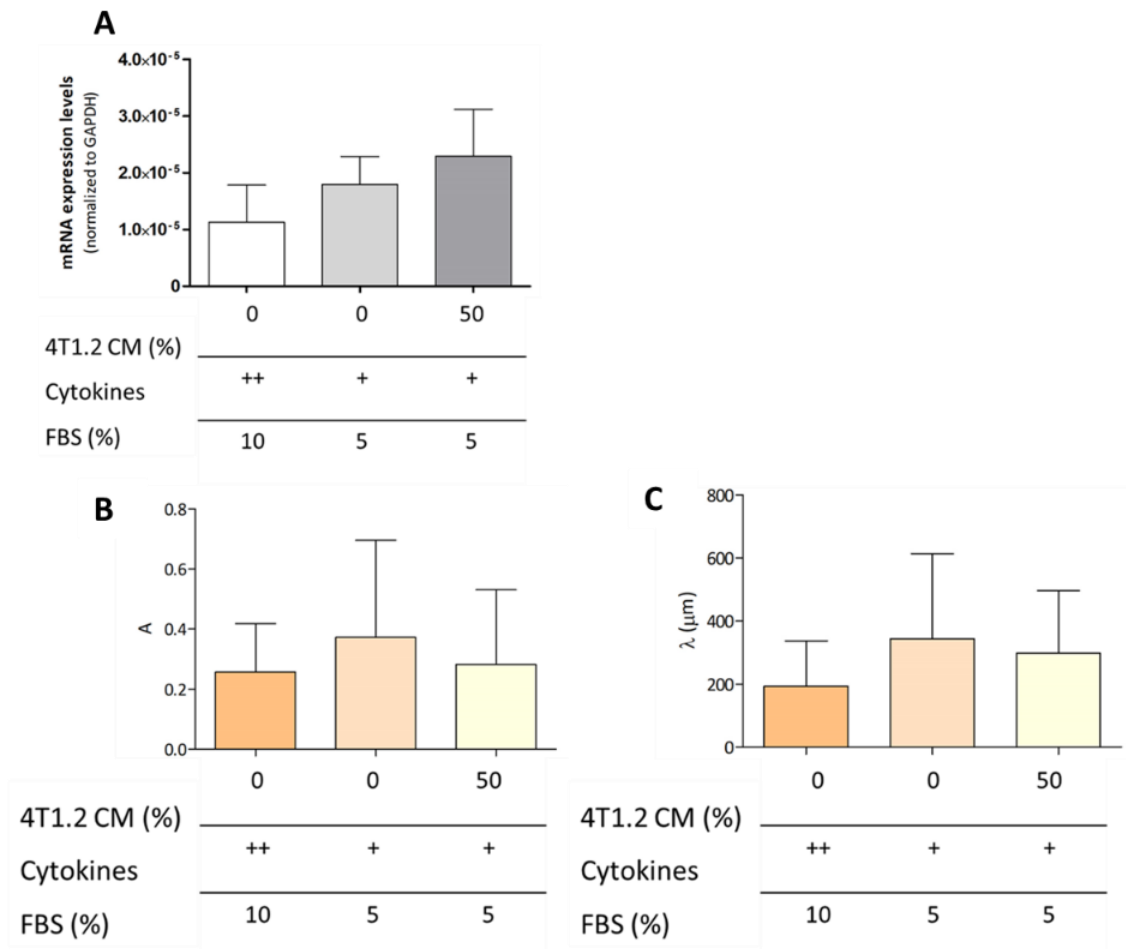


Figure IV. 19 - Comparison between Netrin 1 expression and the neurotrophic potential. **A.** Netrin 1 mRNA expression levels (normalized to the reference gene GAPDH) detected in TCPS-seeded OCs. **B.** A values (permissiveness) and **C.** λ values (axon extension) obtained when DRG were stimulated with OCs CM (same conditions considered for both analysis). Regarding the symbols used in the descriptive tables below each condition: ++ = 30 ng/mL M-CSF and 100 ng/mL RANKL, + = 15 ng/mL M-CSF and 50 ng/mL RANKL. Results are expressed as mean + SD (n=2 for A; n=3 for B and C). Statistical analysis was performed using one-way ANOVA (Kruskal-Wallis test) and Dunns' post test for multiple comparisons. Statistical differences were considered significant for p<0.05.

At first glance, NGF or other neurotrophins would be more obvious targets to be considered in this analysis than an axon guidance molecule. However, previous studies evaluating the neurotrophic potential of OCs revealed that NGF, BDNF, NT-3,4 and 5 were not present in the mature OCs secretome.⁷⁶ While going through the selection of putative molecules that could justify the observed neurotrophic potential, Netrin-1 emerged as a possible candidate for several reasons. Firstly, for its long-time recognized role in axonal guidance. In fact, Netrin-1 is included in a family of laminin-related secretory proteins, which are involved in the nervous system development, by controlling axonal and cellular migration during embryogenesis. Netrin-1 binds to its transmembrane receptors (DCC and UNC5), activating intracellular signaling pathways that trigger cytoskeleton rearrangements, resulting in either axon attraction or repulsion. These reorganizations assume particular relevance in the growth cone, at the end of the extending axon.^{165,166} Secondly, it was discovered that OC precursors have an increased expression of Netrin-1 and its UNC5 receptor, because this protein acts as an autocrine and paracrine factor to promote OC differentiation. The absence of Netrin-1 in both *in vitro* and *in vivo* studies resulted in a reduced OC number and activity.¹⁶⁷ Most importantly, a recent study

showed that OC-induced sensory nerve sprouting observed in OA, another condition that causes skeletal pain, appears to be modulated by the secretion of Netrin-1, which acts through the binding to the DCC receptor expressed by DRG neurons.⁸⁹ Therefore, a similar mechanism could be behind the neurotrophic potential associated with OCs, even because the analysis of tissue and plasma samples revealed increased levels of this protein in BrCa patients.¹⁶⁶ Our group has showed that OC secretome is able to increase axonal outgrowth in physiological conditions. The inappropriate sprouting of bone sensory fibers has been observed in animals of bone metastases. Additionally, the administration of specific inhibitors of osteoclastic activity reduced CABP in clinical trials. It follows that an increase in the OCs neurotrophic potential was expected under tumorigenic stimulation, which did not occur. Looking back at the analysis of the impact of 4T1.2 CM in the number and activity of OCs, previous results did not show an increase in TRAP activity or %ES. Refining the setup in the first part until an effective increase in the OCs activity was observed, subsequently collecting a new batch of OC CM to be used in this second part, is a possibility that could ensure a boost in the neurotrophic potential associated with OCs triggered by BrCa stimuli.

In conclusion, OCs demonstrated neurotrophic potential both in physiological conditions and under tumorigenic effect, supporting a possible role in the ectopic sprouting observed in bone metastases. The comparison between the effect of OCs secretome combined with the bone matrix degradation products (a closer situation to the *in vivo* scenario) versus OCs secretome by itself was also covered, with the first showing a tendency to boost the ability to promote axonal extension.

Chapter V:

CONCLUDING REMARKS & FUTURE WORK

The bone niche is highly complex, comprising a set of different components whose interaction is of extreme importance for the maintenance of homeostasis. Different insults can disturb bone dynamics and deeply impair skeletal functions. BrCa derived bone metastases convey an increased osteoclastic activity, resulting in a weakened skeleton, together with intense pain, which is well recognized as one of the major life quality impairing factors among cancer patients.

At the moment, there are no effective treatments for CABP, because the available drugs do not solve the pain and/or cause adverse side effects. The burden of CABP will presumably escalate in the future, considering the increasing cancer incidence and life expectancy. Accordingly, clinicals and researchers have been fervently pursuing an appropriate drug target for this condition. Understanding the crosstalk between the different cell types involved in this illness rises as a necessity and an opportunity to provide targeted therapies. In particular, the molecular mechanisms behind the ectopic sprouting of bone innervating sensory fibers observed in animal models of bone metastases are largely unknown. The suppression of CABP after administration of specific OCs inhibitors, as well as the neurotrophic potential associated with OCs secretome, allow to foresee a window of opportunity towards the discovery of an efficient therapeutic target by exploring the role of OCs in the pathophysiology of CABP. For this reason, the main goal of the work presented in this thesis was understanding the crosstalk between OCs and nerve cells, as a part of bone cancer pain.

Firstly, the impact of tumorigenic stimuli on the morphology, number and activity of OCs was assessed through an *in vitro* setup used to modulate the interaction between OCs and tumor cells in the context of bone metastases. Essentially, the CM of the bone tropic 4T1.2 BrCa cell line was collected and applied to OCs cultured in TCPS plates or on bone slices (mineralized substrate). The present work showed the treatment regimen where OCs were stimulated with 50% 4T1.2 CM combined with RANKL and M-CSF resulted in mature, large multinucleated, TRAP⁺ OCs, with characteristic actin structures (podosomes, filopodia and actin rings), capable of resorbing bone and secreting TRAP. Contrarily to what was expected, the BrCa cells CM itself did not increase the number or activity of OCs, generating outcomes comparable with the control only when exogenous cytokines (M-CSF and RANKL) were provided. In addition, the 4T1.2 cell line was characterized, revealing residual RANKL expression at the mRNA level and the absence of the correspondent protein in the CM. These results suggest an indirect interaction between OCs and BrCa cells in the scenario of bone metastases.

Moreover, the results showed the *in vitro* setup used requires further refinement for a closer depiction of the pathological situation, where there is an increased osteoclastic activity. As a matter of fact, the chosen model is a simplified version of the bone microenvironment. Indeed, OCs do not exist as an isolated entity in the bone. Quite the contrary, they are in close interaction with stromal and bone cells, which secrete RANKL and M-CSF, two key cytokines required for osteoclastogenesis to happen. This crosstalk assumes a pivotal role not only under physiological conditions, but also in the vicious cycle associated with bone metastases, where stromal cells and bone cells act as intermediaries between BrCa cells and OCs. In this way, using the 4T1.2 CM to stimulate OCs in co-culture with OBs or stromal cells would better mimic the disturbed bone niche created by BrCa derived metastases. The interaction between OBs and OCs should receive special emphasis, because OBs secrete RANKL, M-CSF and OPG, so they have

a key role in controlling the balance between bone formation and resorption.¹⁶⁸ Alternatively, a tri-culture with BrCa cells, OBs and OCs could also be tested as a reliable model of the metastatic bone microenvironment.

In vitro models combining different cell types are more complex and physiologically relevant than mono-culture systems, such as the one used to test the effect of BrCa cells on OCs. However, with increased complexity, comes increased difficulty in creating successful setups. Accordingly, the establishment of co-culture systems can be quite time-consuming and does not always guarantee a better understanding of the mechanisms under consideration. In fact, there are more variables involved, so it can be more difficult to reach clear conclusions. Hence, before attempting to set out a more complex model, it would be interesting to try other concentrations of 4T1.2 CM, as well as different concentrations of RANKL and M-CSF. Testing different combinations of CM and cytokines could reveal the proportion between fresh media and CM that resulted in increased OC activity, better mimicking the osteolytic metastatic lesions. This approach would be less laborious than establishing a co-culture or a triculture model, so it corresponds to a promising strategy in the short term. Still in the context of BrCa cells secretome, in the present work, CM was obtained by culturing a cell line, a feasible and time-effective strategy. Using primary cancer cells could be an interesting alternative for a better recreation of the tumor structure, but at the expense of increased variability between batches of CM collected in different experiments.

The second part of the work involved using the OCs CM collected in the first step to stimulate the axonal terminals of embryonic murine DRG, with the purpose of evaluating the neurotrophic potential of OCs. Complementarily, the neurotrophic potential of the BrCa cells' secretome was also analyzed. The ability of the OCs secretome to promote axonal extension was comparable to the positive stimulation with NGF. This was the outcome observed both under tumorigenic effect and in physiological conditions, given that no significant differences were detected between the two scenarios. On another note, bone degradation products revealed a tendency to increase axons' length, although it did not reach statistical significance. Apart from that, the results showed that the BrCa secretome itself was able to promote axonal elongation in a higher extent than the stimulation with NGF.

The high variability associated with the results, either in the parameter addressing permissiveness, or the one concerning axonal extension, was certainly a major obstacle to find statistically relevant differences. Thus, increasing the number of independent experiments would surely be a good strategy to confirm the previous conclusions. A successful refinement of the initial setup, i.e., observing an increase in the OC number and/or activity following the tumorigenic stimulation, could contribute to an enhanced axonal elongation in the condition representing the bone metastases scenario, which was anticipated but did not occur. A logic following step would be a more comprehensive analysis of the OCs secretome in a quest to identify the molecules responsible for the neurotrophic potential. Here, only the role of Netrin-1 was explored, appearing as a possible candidate. Although OCs revealed little expression at the mRNA level, protein should also be quantified to withdraw definite conclusions regarding the role of Netrin-1 in the neurotrophic potential associated with OCs. Extending this examination to other targets would certainly complement the study. There are various approaches to study the secretome, both at the transcriptomic and proteomic level. DNA and

RNA microarrays are examples for the first case, while proteomic analysis can be performed through protein microarrays (antibody and bead-based arrays) or mass spectrometry, for example.^{123,124,169}

A single device comprising the interaction between the three different cell types considered in this study – BrCa cells, OCs and DRG – would certainly be an interesting step towards the establishment of an *in vitro* model able to reproduce the complexity of bone microenvironment when affected by metastases. Compartmentalized microfluidic devices remain an appropriate platform to build such device. This system should include three different sections: the tumor compartment, the sensory compartment and the bone compartment. The sensory compartment should once again replicate the physical separation between the soma and axonal structures, with only the latter being exposed to OCs paracrine effect. The bone compartment should include both OBs and OCs, as the former proved critical for a correct simulation of bone dynamics. The cells used in the present study are relevant options for each of these compartments, for the reasons already exposed. In alternative to a murine model, human cells could be used. One of the advantages of microfluidics is the design flexibility that allows the production of customized devices for each study. Designing a device with coupled pumps or valves would enable spatiotemporally controlled stimulation, contributing to the establishment of an extremely relevant tool to study biological interactions. Such platform is obviously very complex; thus, the described system is presented as an interesting possibility in the long run.

So far, the focus has been on possible *in vitro* strategies to study the role of OCs under the frame of CABP. *In vivo* studies should also be considered. Both have benefits and limitations that are important to address. On one hand, *in vitro* studies allow faster and cheaper results, together with reduced animal sacrifice, removing ethical barriers. Additionally, *in vitro* systems can be used to model complex cellular interactions in a straightforward and simple way. As a consequence, they represent a very important intermediate step towards the comprehension of diseases, leading to the identification of the most relevant drug targets, which can later be tested in preclinical studies. On the other hand, the simplification of biological processes associated with *in vitro* models implies only animal testing and clinical trials provide definite evidence. As such, they are still the gold standard for studying diseases and testing new therapies.^{168,170} In the light of these considerations, once some relevant candidates behind OCs' neurotrophic potential are identified, inhibitors of those molecules could be administered in a murine model of BrCa bone metastases. Subsequently, an immunohistochemistry analysis of mice bones should be performed to assess the changes in the bone innervation pattern. Staining against SP, CGRP and TrkA should be performed, as these correspond to the key biomarkers used to identify sensory nerve fibers. Both healthy controls and a model of BrCa derived bone metastases would have to be included in the study to draw conclusions.

All in all, the results presented contributed for a better comprehension of the interaction between BrCa cells, OCs and nerve cells in the scenario of bone metastases. OCs demonstrated neurotrophic potential under tumorigenic effect, which supports the hypothesis stating they play a role in the ectopic sprouting observed in animal models of CABP.

References

1. Clarke, B. Normal Bone Anatomy and Physiology. *Clin. J. Am. Soc. Nephrol.* **3**, S131–S139 (2008).
2. Mantyh, P. W. The neurobiology of skeletal pain. *Eur. J. Neurosci.* **39**, 508–519 (2014).
3. Johnson, R. W. & Suva, L. J. Hallmarks of Bone Metastasis. *Calcif. Tissue Int.* **102**, 141–151 (2018).
4. Elefteriou, F. Impact of the Autonomic Nervous System on the Skeleton. *Physiol. Rev.* **98**, 1083–1112 (2018).
5. Theocharis, A. D., Skandalis, S. S., Gialeli, C. & Karamanos, N. K. Extracellular matrix structure. *Adv. Drug Deliv. Rev.* **97**, 4–27 (2016).
6. BC Faculty. 6.3 Bone Structure – Anatomy and Physiology. Available at: <https://opentextbc.ca/anatomyandphysiology/chapter/6-3-bone-structure/>. (Accessed: 25th January 2019)
7. Wellness Advocate. Haversian System (Osteon System). (2019). Available at: <https://wellnessadvocate.com/?dgl=4323>. (Accessed: 19th February 2019)
8. Marrella, A. *et al.* Engineering vascularized and innervated bone biomaterials for improved skeletal tissue regeneration. *Mater. Today* **21**, 362–376 (2018).
9. Cora, M. C., Latimer, K. & Travlos, G. S. Bone Marrow. in *Boorman's Pathology of the Rat* 495–519 (Academic Press, 2018). doi:10.1016/B978-0-12-391448-4.00025-3
10. Karampinos, D. C. *et al.* Quantitative MRI and spectroscopy of bone marrow. *J. Magn. Reson. Imaging* **47**, 332–353 (2018).
11. Manolagas, S. C. Birth and Death of Bone Cells: Basic Regulatory Mechanisms and Implications for the Pathogenesis and Treatment of Osteoporosis. *Endocr. Rev.* **21**, 115–137 (2000).
12. Katsimbri, P. The biology of normal bone remodelling. *Eur. J. Cancer Care (Engl)*. **26**, e12740 (2017). doi: 10.1111/ecc.12740
13. Aielli, F., Ponzetti, M. & Rucci, N. Bone Metastasis Pain, from the Bench to the Bedside. *Int. J. Mol. Sci.* **20**, 1–21 (2019).
14. Florencio-Silva, R., Sasso, G. R. da S., Sasso-Cerri, E., Simões, M. J. & Cerri, P. S. Biology of Bone Tissue: Structure, Function, and Factors That Influence Bone Cells. *Biomed Res. Int.* **2015**, 421746 (2015). doi: 10.1155/2015/421746
15. Boyle, W. J., Simonet, W. S. & Lacey, D. L. Osteoclast differentiation and activation. *Nature* **423**, 337–342 (2003).
16. Charles, J. F. & Aliprantis, A. O. Osteoclasts: more than ‘bone eaters’. *Trends Mol. Med.* **20**, 449–459 (2014).
17. Marino, S., Logan, J. G., Mellis, D. & Capulli, M. Generation and culture of osteoclasts. *Bonekey Rep.* **3**, 570–578 (2014).
18. Kleinhans, C., Schmid, F. ., Schmid, F. V. & Kluger, P. J. Comparison of osteoclastogenesis and resorption activity of human osteoclasts on tissue culture polystyrene and on natural extracellular bone matrix in 2D and 3D. *J. Biotechnol.* **205**, 101–110 (2015).
19. Tehrani, S., Faccio, R., Chandrasekar, I., Ross, F. P. & Cooper, J. A. Cortactin Has an Essential and Specific Role in Osteoclast Actin Assembly. *Mol. Biol. Cell* **17**, 2882–2895 (2006).
20. Yoneda, T., Hiasa, M., Nagata, Y., Okui, T. & White, F. Contribution of acidic extracellular microenvironment of cancer-colonized bone to bone pain. *Biochim. Biophys. Acta* **1848**, 2677–2684 (2015).
21. Merrild, D. M. *et al.* Pit- and trench-forming osteoclasts: a distinction that matters. *Bone*

- Res.* **3**, 15032 (2015). doi: 10.1038/boneres.2015.32
22. Szulc, P. & Bauer, D. C. Biochemical Markers of Bone Turnover in Osteoporosis. in *Osteoporosis* 1573–1610 (Academic Press, 2013). doi:10.1016/B978-0-12-415853-5.00067-4
 23. Cremers, S., Garnero, P. & Seibel, M. J. Biochemical Markers of Bone Metabolism. in *Principles of Bone Biology* 1857–1881 (Academic Press, 2008). doi:10.1016/B978-0-12-373884-4.00020-3
 24. Bernhardt, A., Koperski, K., Schumacher, M. & Gelinsky, M. Relevance of osteoclast-specific enzyme activities in cell-based in vitro resorption assays. *Eur. Cells Mater.* **33**, 28–42 (2017).
 25. Bull, H., Murray, P. G., Thomas, D., Fraser, A. M. & Nelson, P. N. Acid phosphatases. *Mol. Pathol.* **55**, 65–72 (2002).
 26. Catala, M. & Kubis, N. Gross anatomy and development of the peripheral nervous system. *Handb. Clin. Neurol.* **115**, 29–41 (2013).
 27. Noyes, F. Diagnosis and Treatment of Complex Regional Pain Syndrome. in *Noyes' Knee Disorders: Surgery, Rehabilitation, Clinical Outcomes* 1122–1160 (Elsevier, 2017). doi:10.1016/B978-0-323-32903-3.00040-8
 28. Jimenez-Andrade, J. M. *et al.* A phenotypically restricted set of primary afferent nerve fibers innervate the bone versus skin: therapeutic opportunity for treating skeletal pain. *Bone* **46**, 306–313 (2010).
 29. Frost, C. Ø., Hansen, R. R. & Heegaard, A.-M. Bone pain: current and future treatments. *Curr. Opin. Pharmacol.* **28**, 31–37 (2016).
 30. Nencini, S. & Ivanusic, J. J. The Physiology of Bone Pain. How Much Do We Really Know? *Front. Physiol.* **7**, 1–15 (2016).
 31. Mantyh, W. G. G. *et al.* Blockade of nerve sprouting and neuroma formation markedly attenuates the development of late stage cancer pain. *Neuroscience* **171**, 588–598 (2010).
 32. Mantyh, P. Bone cancer pain: Causes, consequences, and therapeutic opportunities. *Pain* **154**, S54–S62 (2013).
 33. Mantyh, P. W. Mechanisms that drive bone pain across the lifespan. *Br. J. Clin. Pharmacol.* **85**, 1103–1113 (2018).
 34. Serre, C. M., Farlay, D., Delmas, P. D. & Chenu, C. Evidence for a Dense and Intimate Innervation of the Bone Tissue, Including Glutamate-Containing Fibers. *Bone* **25**, 623–629 (1999).
 35. Gebhart, G. F. Neurofilament Protein NF200. in *Encyclopedia of Pain* 2046–2046 (Springer Berlin Heidelberg, 2013). doi:10.1007/978-3-642-28753-4_201396
 36. Dubin, A. E. & Patapoutian, A. Nociceptors: the sensors of the pain pathway. *J. Clin. Invest.* **120**, 3760–3772 (2010).
 37. Tyler, W. J., Perrett, S. P. & Pozzo-Miller, L. D. The role of neurotrophins in neurotransmitter release. *Neuroscientist* **8**, 524–531 (2002).
 38. Chao, M. V. Neurotrophins and their receptors: A convergence point for many signalling pathways. *Nat. Rev. Neurosci.* **4**, 299–309 (2003).
 39. Chang, D. S., Hsu, E., Hottinger, D. G. & Cohen, S. P. Anti-nerve growth factor in pain management: current evidence. *J. Pain Res.* **9**, 373–383 (2016).
 40. Rostock, C., Schrenk-Siemens, K., Pohle, J. & Siemens, J. Human vs. Mouse Nociceptors – Similarities and Differences. *Neuroscience* **387**, 13–27 (2018).
 41. Chartier, S. R., Mitchell, S. A. T., Majuta, L. A. & Mantyh, P. W. The Changing Sensory and

- Sympathetic Innervation of the Young, Adult and Aging Mouse Femur. *Neuroscience* **387**, 178–190 (2018).
42. Turney, S. G. *et al.* Nerve growth factor stimulates axon outgrowth through negative regulation of growth cone actomyosin restraint of microtubule advance. *Mol. Biol. Cell* **27**, 500–517 (2016).
 43. Kathryn, M. Albers; Brian, M. D. The Skin as a Neurotrophic Organ. *Neurosci.* **13**, 371–382 (2007).
 44. Mantyh, P. W. Bone cancer pain: from mechanism to therapy. *Curr. Opin. Support. Palliat. Care* **8**, 83–90 (2014).
 45. Johns Hopkins Medicine. What Are Tumors? (2018). Available at: <http://pathology.jhu.edu/pc/BasicTypes1.php>. (Accessed: 6th February 2019)
 46. Ren, G., Esposito, M. & Kang, Y. Bone metastasis and the metastatic niche. *J. Mol. Med. (Berl)*. **93**, 1203–1212 (2015).
 47. Simmons, J. K. *et al.* Animal Models of Bone Metastasis. *Vet. Pathol.* **52**, 827–841 (2015).
 48. Mourskaia, A. A. *et al.* ABCC5 supports osteoclast formation and promotes breast cancer metastasis to bone. *Breast Cancer Res.* **14**, R149 (2012). doi: 10.1186/bcr3361
 49. Riihimäki, M. *et al.* Metastatic sites and survival in lung cancer. *Lung Cancer* **86**, 78–84 (2014).
 50. Sousa, D. *et al.* Therapeutic Drugs in Bone Loss-Associated Disorders: Clinical Outcomes and Challenges. *Curr. Drug Targets* **18**, 696–704 (2017).
 51. Shiozawa, Y., Eber, M. R., Berry, J. E. & Taichman, R. S. Bone marrow as a metastatic niche for disseminated tumor cells from solid tumors. *Bonekey Rep.* **4**, 689 (2015). doi: 10.1038/bonekey.2015.57
 52. Park, S. H., Eber, M. R., Widner, D. B. & Shiozawa, Y. Role of the Bone Microenvironment in the Development of Painful Complications of Skeletal Metastases. *Cancers (Basel)*. **10**, 141–154 (2018).
 53. Yoneda, T., Hiasa, M. & Okui, T. Crosstalk Between Sensory Nerves and Cancer in Bone. *Curr. Osteoporos. Rep.* **16**, 648–656 (2018).
 54. International Agency for Cancer Research. Age standardized (World) incidence rates, breast, all ages. (2018). Available at: <http://gco.iarc.fr/today>. (Accessed: 28th November 2018)
 55. Mathis, K. M. *et al.* Bone resorption and bone metastasis risk. *Med. Hypotheses* **118**, 36–41 (2018).
 56. de Groot, A. F., Appelman-Dijkstra, N. M., van der Burg, S. H. & Kroep, J. R. The anti-tumor effect of RANKL inhibition in malignant solid tumors – A systematic review. *Cancer Treat. Rev.* **62**, 18–28 (2018).
 57. Falk, S. & Dickenson, A. H. Pain and nociception: mechanisms of cancer-induced bone pain. *J. Clin. Oncol.* **32**, 1647–1654 (2014).
 58. Lozano-Ondoua, A. N., Symons-Liguori, A. M. & Vanderah, T. W. Cancer-induced bone pain: Mechanisms and models. *Neurosci. Lett.* **557 Pt A**, 52–59 (2013).
 59. Aghazadeh Tabrizi, M. *et al.* Medicinal Chemistry, Pharmacology, and Clinical Implications of TRPV1 Receptor Antagonists. *Med. Res. Rev.* **37**, 936–983 (2017).
 60. Nicholson, B. Differential diagnosis: nociceptive and neuropathic pain. *Am. J. Manag. Care* **12**, S256–262 (2006).
 61. Zhu, Y. F. *et al.* Rat model of cancer-induced bone pain. *PAIN Reports* **2**, e603 (2017). doi: 10.1097/PR9.0000000000000603
 62. Caraceni, A. & Portenoy, R. K. An international survey of cancer pain characteristics and

- syndromes. IASP Task Force on Cancer Pain. International Association for the Study of Pain. *Pain* **82**, 263–274 (1999).
63. Grond, S. *et al.* High-dose tramadol in comparison to low-dose morphine for cancer pain relief. *J. Pain Symptom Manage.* **18**, 174–179 (1999).
 64. Liberti, M. V & Locasale, J. W. The Warburg Effect: How Does it Benefit Cancer Cells? *Trends Biochem. Sci.* **41**, 211–218 (2016).
 65. Hiasa, M. *et al.* Bone Pain Induced by Multiple Myeloma Is Reduced by Targeting V-ATPase and ASIC3. *Cancer Res.* **77**, 1283–1295 (2017).
 66. Stephan, G. *et al.* The ASIC3/P2X3 cognate receptor is a pain-relevant and ligand-gated cationic channel. *Nat. Commun.* **9**, 1354 (2018). doi: 10.1038/s41467-018-03728-5
 67. Ghilardi, J. R. *et al.* Selective blockade of the capsaicin receptor TRPV1 attenuates bone cancer pain. *J. Neurosci.* **25**, 3126–3131 (2005).
 68. Niiyama, Y., Kawamata, T., Yamamoto, J., Omote, K. & Namiki, A. Bone cancer increases transient receptor potential vanilloid subfamily 1 expression within distinct subpopulations of dorsal root ganglion neurons. *Neuroscience* **148**, 560–572 (2007).
 69. Qiu, F., Wei, X., Zhang, S., Weixiu, Y. & Mi, W. Increased expression of acid-sensing ion channel 3 within dorsal root ganglia in a rat model of bone cancer pain. *Neuroreport* **25**, 887–893 (2014).
 70. Khairatkar-Joshi, N. & Szallasi, A. TRPV1 antagonists: the challenges for therapeutic targeting. *Trends Mol. Med.* **15**, 14–22 (2009).
 71. Manitpisitkul, P. *et al.* TRPV1 antagonist JNJ-39439335 (mavatriptan) demonstrates proof of pharmacology in healthy men: a first-in-human, double-blind, placebo-controlled, randomized, sequential group study. *Pain reports* **1**, e576 (2016). doi: 10.1097/PR9.0000000000000576
 72. Schwarz, M. G., Namer, B., Reeh, P. W. & Fischer, M. J. M. TRPA1 and TRPV1 Antagonists Do Not Inhibit Human Acidosis-Induced Pain. *J. Pain* **18**, 526–534 (2017).
 73. Ortega-Ramírez, A., Vega, R. & Soto, E. Acid-Sensing Ion Channels as Potential Therapeutic Targets in Neurodegeneration and Neuroinflammation. *Mediators Inflamm.* **2017**, 1–18 (2017).
 74. UniProt: a worldwide hub of protein knowledge. *Nucleic Acids Res.* **47**, D506–D515 (2019).
 75. Jimenez-Andrade, J. M. *et al.* Pathological sprouting of adult nociceptors in chronic prostate cancer-induced bone pain. *J. Neurosci.* **30**, 14649–14656 (2010).
 76. Neto, E. *et al.* Osteoclasts control sensory neurons axonal growth through epidermal growth factor receptor signaling. *bioRxiv* 259218 (2018). doi:10.1101/259218
 77. Black, J. A., Nikolajsen, L., Kroner, K., Jensen, T. S. & Waxman, S. G. Multiple sodium channel isoforms and mitogen-activated protein kinases are present in painful human neuromas. *Ann. Neurol.* **64**, 644–653 (2008).
 78. Devor, M. Neuropathic pain: what do we do with all these theories? *Acta Anaesthesiol. Scand.* **45**, 1121–1127 (2001).
 79. Lindqvist, A., Rivero-Melian, C., Turan, I. & Fried, K. Neuropeptide- and tyrosine hydroxylase-immunoreactive nerve fibers in painful Morton’s neuromas. *Muscle Nerve* **23**, 1214–1218 (2000).
 80. Bloom, A. P. *et al.* Breast cancer-induced bone remodeling, skeletal pain, and sprouting of sensory nerve fibers. *J. Pain* **12**, 698–711 (2011).
 81. Biskup, E., Cai, F. & Vetter, M. Bone targeted therapies in advanced breast cancer. *Swiss Med. Wkly.* 2017 1472526 **147**, 14440–14450 (2017).

82. Tonge, D. A. *et al.* Fibronectin supports neurite outgrowth and axonal regeneration of adult brain neurons in vitro. *Brain Res.* **1453**, 8–16 (2012).
83. Yoon, C. *et al.* Low-density lipoprotein receptor-related protein 1 (LRP1)-dependent cell signaling promotes axonal regeneration. *J. Biol. Chem.* **288**, 26557–26568 (2013).
84. Matsunaga, E. *et al.* Periostin, a neurite outgrowth-promoting factor, is expressed at high levels in the primate cerebral cortex. *Dev. Growth Differ.* **57**, 200–208 (2015).
85. Shih, C.-H., Lacagnina, M., Leuer-Bisciotti, K. & Pröschel, C. Astroglial-derived periostin promotes axonal regeneration after spinal cord injury. *J. Neurosci.* **34**, 2438–2443 (2014).
86. Walsh, D. A. *et al.* Angiogenesis and nerve growth factor at the osteochondral junction in rheumatoid arthritis and osteoarthritis. *Rheumatology* **49**, 1852–1861 (2010).
87. Jimenez-Andrade, J. M. & Mantyh, P. W. Sensory and sympathetic nerve fibers undergo sprouting and neuroma formation in the painful arthritic joint of geriatric mice. *Arthritis Res. Ther.* **14**, R101 (2012). doi: 10.1186/ar3826
88. Driscoll, C. *et al.* Nociceptive Sensitizers Are Regulated in Damaged Joint Tissues, Including Articular Cartilage, When Osteoarthritic Mice Display Pain Behavior. *Arthritis Rheumatol.* **68**, 857–867 (2016).
89. Zhu, S. *et al.* Subchondral bone osteoclasts induce sensory innervation and osteoarthritis pain. *J. Clin. Invest.* **129**, 1076–1093 (2019).
90. Hensel, J. *et al.* Osteolytic cancer cells induce vascular/axon guidance processes in the bone/bone marrow stroma. *Oncotarget* **9**, 28877–28896 (2018).
91. Giger, R. J., Hollis, E. R., Tuszynski, M. H. & Tuszynski, M. H. Guidance molecules in axon regeneration. *Cold Spring Harb. Perspect. Biol.* **2**, a001867 (2010). doi: 10.1101/cshperspect.a001867
92. Negishi-Koga, T. *et al.* Suppression of bone formation by osteoclastic expression of semaphorin 4D. *Nat. Med.* **17**, 1473–1480 (2011).
93. Yang, Y.-H. *et al.* Semaphorin 4D Promotes Skeletal Metastasis in Breast Cancer. *PLoS One* **11**, e0150151 (2016). doi: 10.1371/journal.pone.0150151
94. Deb Roy, A. *et al.* Optogenetic activation of Plexin-B1 reveals contact repulsion between osteoclasts and osteoblasts. *Nat. Commun.* **8**, 15831 (2017). doi: 10.1038/ncomms15831
95. Lontos, K. *et al.* The Role of Semaphorin 4D in Bone Remodeling and Cancer Metastasis. *Front. Endocrinol. (Lausanne)*. **9**, 322 (2018). doi: 10.3389/fendo.2018.00322
96. Wang, Y. *et al.* Ephrin B2/EphB4 mediates the actions of IGF-I signaling in regulating endochondral bone formation. *J. Bone Miner. Res.* **29**, 1900–1913 (2014).
97. Labianca, R. *et al.* Adverse Effects Associated with Non-opioid and Opioid Treatment in Patients with Chronic Pain. *Clin. Drug Investig.* **32**, 53–63 (2012).
98. Clézardin, P., Benzaïd, I. & Croucher, P. I. Bisphosphonates in preclinical bone oncology. *Bone* **49**, 66–70 (2011).
99. Handforth, C., D'Oronzo, S., Coleman, R. & Brown, J. Cancer Treatment and Bone Health. *Calcif. Tissue Int.* **102**, 251–264 (2018).
100. Lüftner, D., Niepel, D. & Steger, G. G. Therapeutic approaches for protecting bone health in patients with breast cancer. *The Breast* **37**, 28–35 (2018).
101. Chapurlat, R. D. *et al.* Pathophysiology and medical treatment of pain in fibrous dysplasia of bone. *Orphanet J. Rare Dis.* **7 Suppl 1**, 1–9 (2012).
102. Zekri, J., Mansour, M. & Karim, S. M. The anti-tumour effects of zoledronic acid. *J. Bone Oncol.* **3**, 25–35 (2014).
103. EBCTCG. Adjuvant bisphosphonate treatment in early breast cancer: meta-analyses of individual patient data from randomised trials. *Lancet* **386**, 1353–1361 (2015).

104. Gruys, E., Toussaint, M. J. M., Niewold, T. A. & Koopmans, S. J. Acute phase reaction and acute phase proteins. *J. Zhejiang Univ. Sci. B* **6**, 1045–1056 (2005).
105. Sun, W., Shi, Z., Gao, F., Wang, B. & Li, Z. The pathogenesis of multifocal osteonecrosis. *Sci. Rep.* **6**, 29576 (2016). doi: 10.1038/srep29576
106. Chen, F. & Pu, F. Safety of Denosumab Versus Zoledronic Acid in Patients with Bone Metastases: A Meta-Analysis of Randomized Controlled Trials. *Oncol. Res. Treat.* **39**, 453–459 (2016).
107. Paice, J. A. *et al.* Management of Chronic Pain in Survivors of Adult Cancers: American Society of Clinical Oncology Clinical Practice Guideline. *J. Clin. Oncol.* **34**, 3325–3345 (2016).
108. Middlemiss, T., Laird, B. J. A. & Fallon, M. T. Mechanisms of Cancer-induced Bone Pain. *Clin. Oncol.* **23**, 387–392 (2011).
109. Patel, M. K., Kaye, A. D. & Urman, R. D. Tanezumab: Therapy targeting nerve growth factor in pain pathogenesis. *J. Anaesthesiol. Clin. Pharmacol.* **34**, 111–116 (2018).
110. Webb, M. P., Helander, E. M., Menard, B. L., Urman, R. D. & Kaye, A. D. Tanezumab: a selective humanized mAb for chronic lower back pain. *Ther. Clin. Risk Manag.* **14**, 361–367 (2018).
111. Sopata, M. *et al.* Efficacy and safety of tanezumab in the treatment of pain from bone metastases. *Pain* **156**, 1703–1713 (2015).
112. Alves, C. J. *et al.* Fracture pain—Traveling unknown pathways. *Bone* **85**, 107–114 (2016).
113. Nair, A. S. Tanezumab: Finally a Monoclonal Antibody for Pain Relief. *Indian J. Palliat. Care* **24**, 384–385 (2018).
114. Cancer Research UK. Worldwide cancer incidence statistics. (2018). Available at: <https://www.cancerresearchuk.org/health-professional/cancer-statistics/worldwide-cancer/incidence#heading-One>. (Accessed: 25th November 2018)
115. International Agency for Cancer Research. Cancer World Fact Sheets. (2018). Available at: <http://gco.iarc.fr/today/home>. (Accessed: 16th February 2019)
116. Neto, E. *et al.* Sensory neurons and osteoblasts: close partners in a microfluidic platform. *Integr. Biol. (Camb)*. **6**, 586–595 (2014).
117. Lelekakis, M. *et al.* A novel orthotopic model of breast cancer metastasis to bone. *Clin. Exp. Metastasis* **17**, 163–170 (1999).
118. Bartell, S. M. *et al.* FoxO proteins restrain osteoclastogenesis and bone resorption by attenuating H₂O₂ accumulation. *Nat. Commun.* **2014** **5**, 3773 (2014). doi: 10.1038/ncomms4773
119. Sousa, D. M. *et al.* Ablation of Y1 receptor impairs osteoclast bone-resorbing activity. *Sci. Rep.* **6**, 33470 (2016). doi: 10.1038/srep33470
120. Park, J. W., Vahidi, B., Taylor, A. M., Rhee, S. W. & Jeon, N. L. Microfluidic culture platform for neuroscience research. *Nat. Protoc.* **1**, 2128–2136 (2006).
121. Ye, J. *et al.* Primer-BLAST: a tool to design target-specific primers for polymerase chain reaction. *BMC Bioinformatics* **13**, 134 (2012). doi: 10.1186/1471-2105-13-134
122. Kozlow, W. & Guise, T. A. Breast Cancer Metastasis to Bone: Mechanisms of Osteolysis and Implications for Therapy. *J. Mammary Gland Biol. Neoplasia* **10**, 169–180 (2005).
123. Mukherjee, P. & Mani, S. Methodologies to decipher the cell secretome. *Biochim. Biophys. Acta - Proteins Proteomics* **1834**, 2226–2232 (2013).
124. Hathout, Y. Approaches to the study of the cell secretome. *Expert Rev. Proteomics* **4**, 239–248 (2007).
125. Maxie, M. G. Structure and function of bone tissue. in *Jubb, Kennedy & Palmer's*

- Pathology of Domestic Animals* 18–20 (Elsevier Health Sciences, 2015). doi:10.1016/B978-070202823-6.50004-X
126. Hall, B. K. Cells to Make and Cells to Break. in *Bones and Cartilage* 239–258 (Academic Press, 2015). doi:10.1016/B978-0-12-416678-3.00015-X
 127. Vesprey, A. & Yang, W. Pit Assay to Measure the Bone Resorptive Activity of Bone Marrow-derived Osteoclasts. *Bio-protocol* **6**, e1836 (2016). doi: 10.21769/BioProtoc.1836
 128. Zhou, Y. *et al.* SHP2 regulates osteoclastogenesis by promoting preosteoclast fusion. *FASEB J.* **29**, 1635 (2015). doi: 10.1096/FJ.14-260844
 129. Weinstein, R. S. *et al.* Promotion of osteoclast survival and antagonism of bisphosphonate-induced osteoclast apoptosis by glucocorticoids. *J. Clin. Invest.* **109**, 1041–1048 (2002).
 130. Sjøe, K. & Delaissé, J.-M. Time-lapse reveals that osteoclasts can move across the bone surface while resorbing. *J. Cell Sci.* **130**, 2026–2035 (2017).
 131. Ljusberg, J. *et al.* Proteolytic excision of a repressive loop domain in tartrate-resistant acid phosphatase by cathepsin K in osteoclasts. *J. Biol. Chem.* **280**, 28370–28381 (2005).
 132. Mancino, A. T., Klimberg, V. S., Yamamoto, M., Manolagas, S. C. & Abe, E. Breast cancer increases osteoclastogenesis by secreting M-CSF and upregulating RANKL in stromal cells. *J. Surg. Res.* **100**, 18–24 (2001).
 133. Xu, F. & Teitelbaum, S. L. Osteoclasts: New Insights. *Bone Res.* **1**, 11–26 (2013).
 134. Lamghari, M., Tavares, L., Camboa, N. & Barbosa, M. A. Leptin effect on RANKL and OPG expression in MC3T3-E1 osteoblasts. *J. Cell. Biochem.* **98**, 1123–1129 (2006).
 135. Hasegawa, Y. *et al.* Resolvin E1 Inhibits Osteoclastogenesis and Bone Resorption by Suppressing IL-17-induced RANKL Expression in Osteoblasts and RANKL-induced Osteoclast Differentiation. *Yonago Acta Med.* **61**, 8–18 (2018).
 136. Yoshimura, T., Yoshimura, Y., Deyama, Y., Suzuki, K. & Iida, J. Mechanical stress up-regulates RANKL expression via the VEGF autocrine pathway in osteoblastic MC3T3-E1 cells. *Mol. Med. Rep.* **2**, 229–234 (2009).
 137. Gollahon, L. S., Schuster, C., Mo, H., Shen, C.-L. & Gollahon, L. RANK/RANKL/OPG: The Axis of Breast Cancer Bone Metastasis Evil? *Annals of Breast Cancer Research* **2**, 1008-1017 (2017).
 138. Ney, J. T., Fehm, T., Juhasz-Boess, I. & Solomayer, E. F. RANK, RANKL and OPG Expression in Breast Cancer - Influence on Osseous Metastasis. *Geburtshilfe Frauenheilkd.* **72**, 385–391 (2012).
 139. Schubert, A., Schulz, H., Emons, G. & Gründker, C. Expression of osteoprotegerin and receptor activator of nuclear factor- κ B ligand (RANKL) in HCC70 breast cancer cells and effects of treatment with gonadotropin-releasing hormone on RANKL expression. *Gynecol. Endocrinol.* **24**, 331–338 (2008).
 140. Nicolin, V. & Narducci, P. Soluble TRAIL could enhance bone destruction acting on Rankl ligand in estrogen-independent human breast cancer cell line MDA-MB-231. *Acta Histochem.* **112**, 189–192 (2010).
 141. Nicolin, V. *et al.* Breast adenocarcinoma MCF-7 cell line induces spontaneous osteoclastogenesis via a RANK-ligand-dependent pathway. *Acta Histochem.* **110**, 388–396 (2008).
 142. Ell, B. *et al.* Tumor-induced osteoclast miRNA changes as regulators and biomarkers of osteolytic bone metastasis. *Cancer Cell* **24**, 542–556 (2013).
 143. Kim, B., Kim, H.-H. & Lee, Z. H. α -Tocopheryl Succinate Inhibits Osteolytic Bone Metastasis of Breast Cancer by Suppressing Migration of Cancer Cells and Receptor Activator of

- Nuclear Factor- κ B Ligand Expression of Osteoblasts. *J. bone Metab.* **25**, 23–33 (2018).
144. Sackmann, E. K., Fulton, A. L. & Beebe, D. J. The present and future role of microfluidics in biomedical research. *Nature* **507**, 181–189 (2014).
 145. Halldorsson, S., Lucumi, E., Gómez-Sjöberg, R. & Fleming, R. M. T. Advantages and challenges of microfluidic cell culture in polydimethylsiloxane devices. *Biosens. Bioelectron.* **63**, 218–231 (2015).
 146. Neto, E. *et al.* Compartmentalized Microfluidic Platforms: The Unrivaled Breakthrough of *In Vitro* Tools for Neurobiological Research. *J. Neurosci.* **36**, 11573–11584 (2016).
 147. Willerth, S. Natural biomaterials for engineering neural tissue from stem cells. in *Engineering Neural Tissue from Stem Cells* (Academic Press, 2017).
 148. Letourneau, P. Axonal Pathfinding: Extracellular Matrix Role. in *Encyclopedia of Neuroscience* **1**, 1139–1145 (Academic Press, 2009).
 149. Sleigh, J. N., Weir, G. A. & Schiavo, G. A simple, step-by-step dissection protocol for the rapid isolation of mouse dorsal root ganglia. *BMC Res. Notes* **9**, 82 (2016). doi: 10.1186/s13104-016-1915-8
 150. Melli, G. & Höke, A. Dorsal Root Ganglia Sensory Neuronal Cultures: a tool for drug discovery for peripheral neuropathies. *Expert Opin. Drug Discov.* **4**, 1035–1045 (2009).
 151. Fornaro, M., Sharthiya, H. & Tiwari, V. Adult Mouse DRG Explant and Dissociated Cell Models to Investigate Neuroplasticity and Responses to Environmental Insults Including Viral Infection. *J. Vis. Exp.* e56757 (2018). doi:10.3791/56757
 152. Neto, E. *et al.* Axonal outgrowth, neuropeptides expression and receptors tyrosine kinase phosphorylation in 3D organotypic cultures of adult dorsal root ganglia. *PLoS One* **12**, e0181612 (2017). doi: 10.1371/journal.pone.0181612
 153. Bernhardt, A., Schamel, M., Gbureck, U. & Gelinsky, M. Osteoclastic differentiation and resorption is modulated by bioactive metal ions Co²⁺, Cu²⁺ and Cr³⁺ incorporated into calcium phosphate bone cements. *PLoS One* **12**, e0182109 (2017). doi: 10.1371/journal.pone.0182109
 154. Rosenberg, S. S. & Spitzer, N. C. Calcium signaling in neuronal development. *Cold Spring Harb. Perspect. Biol.* **3**, a004259 (2011). doi: 10.1101/cshperspect.a004259
 155. Diez-Roux, G. *et al.* A High-Resolution Anatomical Atlas of the Transcriptome in the Mouse Embryo. *PLoS Biol.* **9**, e1000582 (2011). doi: 10.1371/journal.pbio.1000582
 156. Xi, F. *et al.* Calcium/calmodulin-dependent protein kinase II regulates mammalian axon growth by affecting F-actin length in growth cone. *bioRxiv* 518076 (2019). doi:10.1101/518076
 157. Vizard, T. N. *et al.* Regulation of axonal and dendritic growth by the extracellular calcium-sensing receptor. *Nat. Neurosci.* **11**, 285–291 (2008).
 158. Liu, M. *et al.* Effect of nano-hydroxyapatite on the axonal guidance growth of rat cortical neurons. *Nanoscale* **4**, 3201–3207 (2012).
 159. Li, S., Gu, X. & Yi, S. The Regulatory Effects of Transforming Growth Factor- β on Nerve Regeneration. *Cell Transplant.* **26**, 381–394 (2017).
 160. Knöferle, J. *et al.* TGF- β 1 enhances neurite outgrowth via regulation of proteasome function and EFABP. *Neurobiol. Dis.* **38**, 395–404 (2010).
 161. Walshe, T. E., Leach, L. L. & D'Amore, P. A. TGF- β signaling is required for maintenance of retinal ganglion cell differentiation and survival. *Neuroscience* **189**, 123–31 (2011).
 162. Li, Y., Zhao, E. & Chen, D. Emerging roles for insulin-like growth factor binding protein like protein 1. *Neural Regen. Res.* **14**, 258 (2019). doi: 10.4103/1673-5374.244787
 163. Guo, C. *et al.* IGF1 Regulates Axon Growth through IGF-1-mediated Signaling

- Cascades. *Sci. Rep.* **8**, 2054 (2018). doi: 10.1038/s41598-018-20463-5
164. Sun, K. L. W., Correia, J. P. & Kennedy, T. E. Netrins: versatile extracellular cues with diverse functions. *Development* **138**, 2153–2169 (2011).
 165. Boyer, N. P. & Gupton, S. L. Revisiting Netrin-1: One Who Guides (Axons). *Front. Cell. Neurosci.* **12**, 221 (2018). doi: 10.3389/fncel.2018.00221
 166. Kefeli, U. *et al.* Netrin-1 in cancer: Potential biomarker and therapeutic target? *Tumor Biol.* **39**, 4 (2017). doi: 10.1177/1010428317698388.
 167. Mediero, A., Ramkhalawon, B., Perez-Aso, M., Moore, K. J. & Cronstein, B. N. Netrin-1 is a critical autocrine/paracrine factor for osteoclast differentiation. *J. Bone Miner. Res.* **30**, 837–854 (2015).
 168. Owen, R. & Reilly, G. C. In vitro Models of Bone Remodelling and Associated Disorders. *Front. Bioeng. Biotechnol.* **6**, 134 (2018). doi: 10.3389/fbioe.2018.00134
 169. Hsiao, Y.-C., Chu, L. J., Chen, J.-T., Yeh, T.-S. & Yu, J.-S. Proteomic profiling of the cancer cell secretome: informing clinical research. *Expert Rev. Proteomics* **14**, 737–756 (2017).
 170. Salamanna, F., Contartese, D., Maglio, M. & Fini, M. A systematic review on in vitro 3D bone metastases models: A new horizon to recapitulate the native clinical scenario? *Oncotarget* **7**, 44803–44820 (2016).

APPENDIX

Table A. 1 - RNA integrity data returned by the Experion software. RQI assessment implies comparing the RNA sample with a set of degraded RNA standards. The principle behind the method is that RNA degradation results in smaller RNA fragments, with a lower molecular-weight, therefore fast-moving, which accumulate towards the bottom of the electropherogram. RQI numeric classification is associated with a color-coded labelling system that enables a quick evaluation of samples' quality: $1 \leq RQI \leq 4$ is shown in red and corresponds to degraded samples that should not be used; $4 \leq RQI \leq 7$ is displayed in yellow, meaning samples underwent some degradation; $7 \leq RQI \leq 10$ are presented in green, meaning RNA has a good integrity and can be used with complete confidence.

Well ID	Sample Name	RNA Area	RNA Concentration (ng/ul)	Ratio [28S:18S]	RQI	RQI Classification	RQI Alert
L	Ladder	527.80	160.00				
1	1 Patricia	149.36	45.28	0.68	7.2	■	
2	2	677.62	205.42	1.09	9.5	■	
3	3	19.37	5.87	1.41	N/A		RNA conc. too low
4	4	264.43	80.16	1.12	9.2	■	
5	5	102.30	31.01	1.40	9.3	■	
6	6	55.49	16.82	1.43	9.7	■	
7	7	131.49	39.86	1.35	8.0	■	
8	8	69.50	21.07	1.44	9.7	■	
9	9	100.43	30.44	1.53	9.8	■	
10	10	1,612.30	488.76	1.34	9.7	■	
11	11	1,722.30	522.10	0.66	3.1	■	
12	12	1,958.43	593.68	0.92	8.4	■	

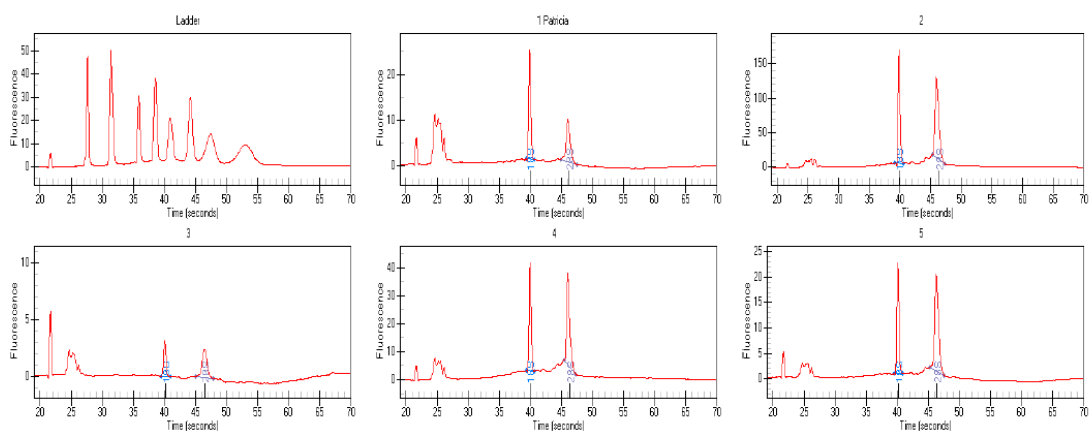


Figure A. 1 – Example of electropherograms obtained. The first graph corresponds to the ladder with different molecular weights, while the remaining graphs display samples electropherograms.

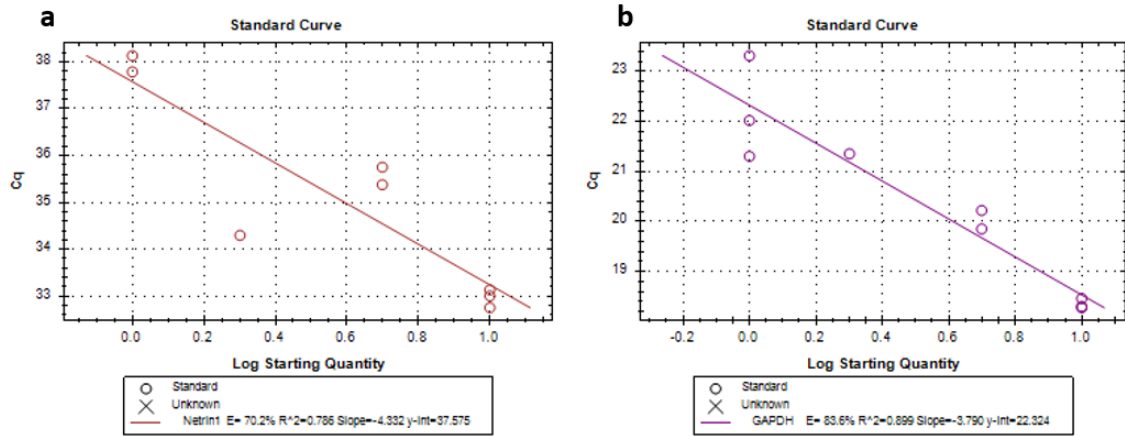


Figure A. 2 - Efficiency curves obtained for a. Netrin-1 and b. GAPDH primers. Netrin-1 (target gene) was amplified with a 70.2% efficiency, while amplification efficiency for GAPDH (reference gene) reached 83,6% (in the OCS cDNA). Ideally, this parameter should be between 90 to 110%. Withal, the efficiencies obtained are still within the acceptable. A set of 4 dilutions (1x, 2x, 5x and 10x) of a chosen cDNA sample was used to obtain the standard curve for each gene.